Measurement and Time Domain Modeling of Superconductor-Insulator-Superconductor (SIS) Mixing Junctions for Radioastronomy

by

Douglas W. Henke
B.Eng., University of Victoria, 2001

A Thesis Submitted in Partial Fulfillment of the
Requirements for the Degree of

MASTER OF APPLIED SCIENCE

in the Department of Electrical and Computer Engineering

Supervisors: Dr. Wolfgang J. R. Hoefer and Dr. Stéphane M. X. Claude

Abstract

This thesis describes the methods utilized to characterize the superconductor-insulator-superconductor (SIS) mixer used in millimeter-wave low noise radioastronomy receivers. An overview of the theory and measurement techniques is given to determine the noise contribution of double-sideband (DSB) and sideband-separating (2SB) receiver assemblies. Experimental results are shown for DSB and 2SB receivers operating in the frequency range of 84-116 GHz.

The detailed theory of the quasiparticle tunnel junction is reviewed; first, for the standard frequency domain presentation, and then, special emphasis is given to the time domain formulation. A new time-stepping algorithm, based on the voltage update method, is demonstrated in the large signal case using MATLAB. It can be used to determine the large signal voltage developed across the junction while accounting for the source impedance. Using this technique, the quantum mixer theory is embedded into MEFiSTo-3D Pro, a time domain electromagnetic field solver, and demonstrated for simple source impedances.

Supervisors:

Dr. W. J. R. Hoefer, (Department of Electrical and Computer Engineering)

Dr. S. M. X. Claude, (Herzberg Institute of Astrophysics, Victoria, BC, Canada)

Contents

List of Figures

Acknowledgements

I would like to express my deep gratitude to my supervisors, Dr. Wolfgang Hoefer and Dr. Stéphane Claude, for giving me the chance to participate in such interesting research.

During my involvement at the Herzberg Institute of Astrophysics, Dr. Claude has exemplified true leadership and created a dynamic and satisfying research experience. It has been a great pleasure to work and study under his mentorship. Special acknowledgements are given to members of the Band 3 team that I worked with: André Anthony, Dennis Derdall, Dr. Philip Dindo, David Dousset, Dave Duncan, Darren Erickson, Dominic Garcia, Dr. Frank Jiang, Brian Leckie, Ajaz Mirza, Pat Niranjanan, Mike Pfleger, Greg Rodrigues, Kei Szeto, Paul Welle and Keith Yeung. Extra thanks goes to Dennis and Greg, who taught me the ways of a mad scientist, and Keith, Philip and Frank who provided many helpful and encouraging discussions. Thanks to Pat for making the VNA measurements of the LO inline absorbers. I am grateful to the Institute for providing the research contributions through the D. C. Morton Fellowship.

I would like to thank Dr. Alessandro Navarrini for supplying a Mathcad script demonstrating the frequency domain quantum mixer theory.

I consider myself highly privileged to have studied under the supervision of Dr. Hoefer. He has demonstrated an expert level of skill and understanding in electromagnetic theory and modeling, and I have appreciated learning from such a respected and recognized professor. I am grateful for the freedom he gave me in my research, for his creative explanations and for his contributions through the research assistance funding. I am very thankful for the programming expertise of Dr. Poman So, as well as his great ideas, encouragements and the long hours spent helping with the research presented herein. Special thanks goes to Dr. Rambabu Karumudi and Huilian Du for their helpful advice and interesting conversation.

I would like to express my thankfulness to my parents for encouraging me through this rewarding step. I give thanks to God for the blessing of this opportunity and for the gift of my lovely wife, Amanda, who is my companion and has given me her unending support (and a good excuse to leave my research and go hiking with her!).

1 Introduction

Through the observation of the millimeter and submillimeter-wave electromagnetic spectrum, astronomers have the opportunity to explore unique phenomena not visible with optical telescopes. In fact, one of the most compelling motivations for millimeter-wave receivers is to further enhance the science describing the origin of stars and galaxies [1]. In the star forming regions, visible light is absorbed by the surrounding dust clouds. For very distant objects, the absorbed energy is re-emitted in the millimeter and submillimeter bands. Cold gases that surround star forming regions may be characterized by the molecular transitions that result in distinct spectral lines and may be studied to provide information on the structure and chemical composition of newly formed stars.

Since the (sub)millimeter band is strongly attenuated in the presence of water vapor, a major limitation is caused by the earth's atmosphere. As such, certain observing locations are selected around the world that exhibit the qualities of high altitude and dry conditions. Even in these remote sites, the atmosphere still gives rise to transmission bands, or atmospheric windows, which dictate certain bands of frequencies that can be received (see [1] for an example).

There are several types of millimeter-wave detectors in use today and excellent reviews are given in [3] and [21]. This thesis may be categorized into the class of heterodyne receivers based on the ultra-low noise *superconductor-insulator-superconductor (SIS)* junction. Heterodyning refers to the process whereby a high frequency signal is downconverted to an intermediate frequency (IF) by means of combining the signal with a local oscillator (LO) and passing it through a nonlinear mixing device.

Through a joint partnership between Europe and North America, with the possible inclusion of Japan, the *Atacama Large Millimeter Array (ALMA)* [2] project combines the elements listed above. When completed, ALMA will consist of an array of 64, 12 meter antennas located in the Atacama desert of northern Chile. Comprising Canada's role in the ALMA project, the millimeter-wave instrumentation group of the Herzberg Institute of Astrophysics (HIA) has undertaken the goal of supplying the front end cartridge of the receiver for the third millimeter-wave band of 84-116 GHz (Band 3).

The theory of SIS receivers originates from the discovery of superconductivity [4]-[9], where it was found that if two superconductors were separated by a very thin section of insulator, electron tunneling would occur [12]-[18]. In particular, it was discovered that the quasiparticle tunneling exhibited a quantum mechanical characteristic in the presence of incident radiation upon the junction. This phenomenon, called *photon-assisted tunneling*, provided the framework for SIS junctions to be used as detectors. A complete quantum theory describing mixing features of the SIS junction was developed; the papers by J. R. Tucker [19],[20], along with the joint authorship of M. J. Feldman [21], are considered the standard. Another excellent paper, presented from a photodiode perspective, is [25]. Most of the theory was formulated within the frequency domain, but the time domain theory and applications were also considered [19]-[21],[26]-[30].

The exciting result of Tucker's theory pointed to a quantum limited sensitivity of SIS detectors, i.e., that the receiver noise temperature could reach as low as hf/k (C.F. Sec. 3.3). Several modeling predictions and measurements at various frequencies have shown receiver sensitivity approaching this limit [34]-[48]. Of particular relevance to this thesis are measurements falling in the band of 84-116 GHz. Measured results, all using the same mixer chip design, are given in [45]-[47] and indicate a receiver noise temperature of 3-4 times the quantum limit, which are consistent with the measurements found in this thesis. Another example using a different chip design was measured to achieve a similar performance [44]. For this band, these measurements remain amongst the lowest measured in the world today for a millimeter-wave detector.

Tucker's theory may be implemented using a high level programming language and requires a two part solution. First, the large signal waveform (i.e., local oscillator) applied across the SIS junction must be determined [53]-[55], and secondly, the small signal mixing and noise analysis is performed. Most designers use custom programs and tools to complete this step, although a C++ open source code using frequency domain algorithms is available [59].

1.1 Aim of Thesis

The main objective of this thesis is to provide the reader with the necessary tools to characterize the SIS mixer receiver. The theory and practical measurement techniques of

both *double-sideband (DSB)* and *sideband-separating (2SB)* receiver assemblies are presented. Top-level modeling methods are given and validated through measured results. With this information presented first, motivation is given to explore modeling of the junction at a closer detail.

Complementing the measured results, an approach to modeling the mixing component at the junction level is developed. The standard frequency domain theory is provided, but the emphasis is on the time domain theory. Some examples of modeling different components of the mixer chip are given. Finally, the groundwork for implementing the quantum mixer theory into a time domain field solver is presented. This algorithm offers future designers the ability to embed the junction theory into a full wave field solver.

1.2 Contribution

The work presented within this thesis has taken place in two stages. Using the world class millimeter-wave facilities of the Herzberg Institute of Astrophysics (HIA), which is part of the National Research Council of Canada (NRC), the laboratory component was completed. The experimentation contributed towards the demonstration phase of the Band 3 cartridges to be used within the ALMA receivers. The main impact was the completion of the assembly and test of the 2SB receiver, using newly designed components (e.g., the HIA cryogenic low noise amplifier and the sideband-separating assembly). Component designs and cryostat expertise were provided by the electrical and mechanical design teams at HIA.

The second stage of research was accomplished with the cooperation and facilities of the Computational Electromagnetics Research Laboratory (CERL) at the University of Victoria. Because of the expertise in time domain modeling, the time domain formulation of Tucker's theory was explored in practical detail. The contribution of this thesis is a time-stepping algorithm, fully consistent with the full quantum mixer theory and demonstrated using MATLAB [60]. The embedding of the algorithm into a full wave field solver, MEFiSTo-3D Pro [62], was completed with the programming abilities and resources of CERL. A large signal analysis was used as a demonstration to validate the method. To the author's knowledge, the quantum mixer theory has not yet been embedded into any field solver.

1.3 Future Work

Using the time domain algorithm presented herein, more complex designs involving bias and tuning networks need to be implemented and tested. A convenient way of handling the noise needs to be embedded alongside of the time domain theory. While a true time domain modeling of the noise is probably not feasible, the results of the simulation (i.e., the large signal waveform) can be used directly to implement a separate noise module. Finally, a quantitative comparison of the small signal results should be completed against some other valid technique.

2 Noise Measurements of SIS Mixers

2.1 Noise Definitions

2.1.1 Black Body Radiation

To measure the noise of a receiver system, the *Y-Factor* method is used. In this technique, the system is presented with two different radiative loads at different temperatures. To provide some background to the noise measurement, it is useful at this point to explore some introductory concepts.

One method of thermal energy transfer is through radiation [10], [11]. According to Stefan's law, the net power radiated by an object is given by

$$P_{net} = e\sigma A\left(T^4 - T_0^4\right) \tag{1}$$

where P_{net} is the power radiated, e is the emissivity of the object, σ is *Stefan's constant*, A is the area, T_0 is the temperature of the surroundings and T is the temperature of the object. If $T < T_0$, then P_{net} is the power absorbed. If an object absorbs all the radiation that is incident on it, it is called a *black-body*. Since all incident power is absorbed, the only power that is radiated from the object is precisely at the temperature of the object itself, and so a black-body is also an ideal radiator.

When considering the radiated energy of a black-body, experimental data show that the energy varies with both temperature and wavelength. The classical approximation to this is given by the *Rayleigh-Jeans Law*, but this expression suffers when high frequencies or low temperatures are used (and also leads to the so-called *ultraviolet catastrophe*). With the introduction of quantum mechanics, Max Planck accounted for these inadequacies by using

$$P^{Planck}(f,T) = kTB\left(\frac{hf/kT}{e^{hf/kT}-1}\right) \tag{2}$$

where f is the frequency, B is the bandwidth around the frequency ($B << f$), h is Planck's constant and k is Boltzmann's constant. However, in [31] it has been demonstrated that Planck's equation is not consistent with the noise limitations given by Tucker's quantum mixer theory [19], [20], [21]. Through Callen and Welton's work

[33], a correction factor has been added to account for the *zero-point fluctuations* (quantum noise), so that the power radiated is

$$P^{C\&W}(f,T) = kTB\left(\frac{hf/kT}{e^{hf/kT}-1}\right)+\frac{hfB}{2}. \tag{3}$$

Note that this correction is half the energy of a photon scaled by the bandwidth and that, in the limit of T $\rightarrow$ 0, the expression no longer tends to zero, but rather approaches the half photon energy. Therefore, the Callen and Welton formulation shows that even though a blackbody may be at a physical temperature of 0 K, it will still radiate some energy due to the zero-point fluctuations.

Another observation may be made when considering low frequencies and high temperatures, so that $hf/kT << 1$. In this condition, $P^{C\&W}$ reduces to the Rayleigh-Jeans approximation of

$$P^{RJ}(f,T) = kTB \tag{4}$$

where T in the above three equations refers to the physical temperature of the blackbody.

2.1.2 Noise Power and Equivalent Noise Temperature

It is convenient to write a generalized power expression in the same format as (4), such that

$$P^{n}(f,T) = kT^{n}B. \tag{5}$$

Note that T^{n} is not the physical temperature of the body, but rather the noise temperature as given by the Rayleigh-Jeans, Planck or Callen and Welton expressions. By re-writing, the noise temperature is

$$T^{n} = \frac{P^{n}(f,T)}{kB}. \tag{6}$$

It should be emphasized that T^{n} is simply the *noise power density* (i.e., per *Hz*) scaled by k^{-1}, and to be consistent with the uncertainty principle, the Callen and Welton expression for power must be used [31], [32]. Depending on the frequency and temperature of measurement, however, it may be sufficient to use the Rayleigh-Jeans approximation.

Fig. 1 shows how the Callen and Welton formulation clearly converges towards the Rayleigh-Jeans approximation. In fact, for a frequency of 100 GHz, the Callen and Welton noise temperature differs by less than ¼ K from the physical temperature of 9 K. However, Planck's equation shows a fixed error of approximately 2.2 K – this error would be more pronounced at higher frequencies [31].

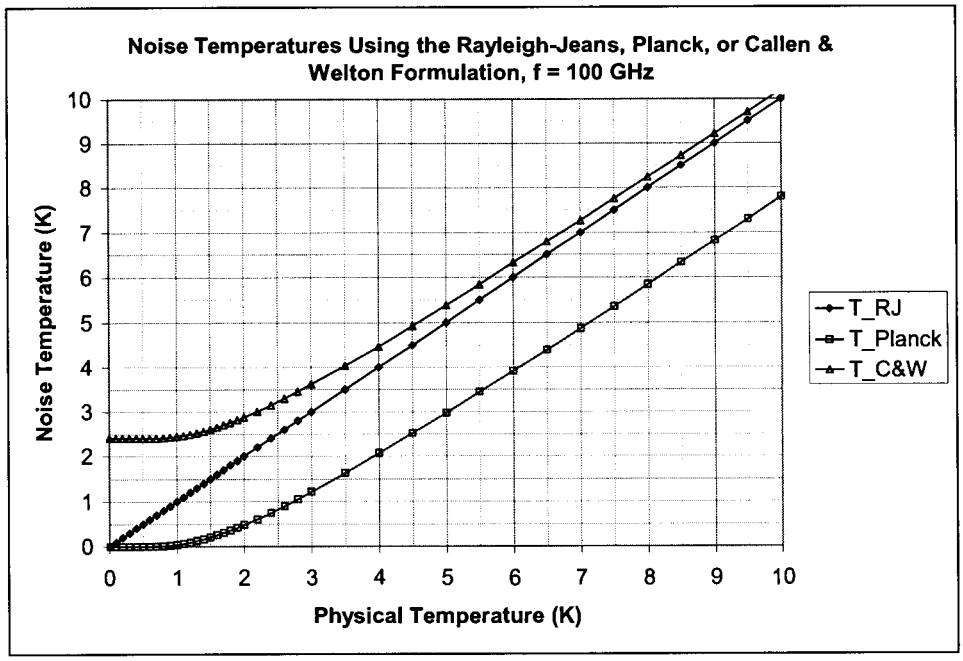

Fig. 1. Comparison of noise temperatures using the Rayleigh-Jeans, Planck and Callen and Welton expressions.

2.1.3 Y-Factor and Measuring Receiver Noise

In the classical view, the *receiver noise temperature* is derived assuming a noiseless input, as shown in Fig. 2. The subtle problem with this understanding is that as a consequence of the zero-point fluctuations, the input termination can no longer be considered noiseless. While there is some debate over whether the zero-point noise should be associated with the input termination or the receiver, the confusion is avoided by defining the receiver noise temperature using the *Y-factor method* in the manner described below [31], [32].

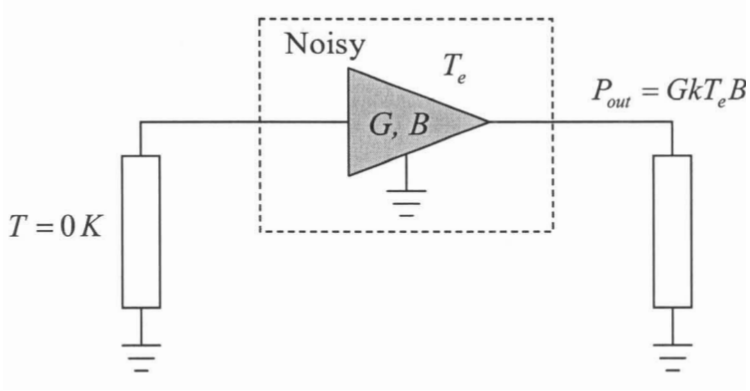

Fig. 2. Classical definition of equivalent noise temperature.

Using (5), the most consistent way to calculate the output power is to use the Callen and Welton expression. The output power can then be referred to the input of the receiver by dividing by the gain and bandwidth; this is the *input noise power density*. Any additional input signal, P^s, will combine with the equivalent input noise power of the receiver, P^r, in the following manner:

$$P_{out} = G\left(P^r + P^s\right)B\,. \tag{7}$$

Using this concept, the noise of the receiver may be determined through the measurement of two separate input signals of different noise temperatures so that

$$P_{out}^{Hot} = G\left(P^r + P_{in}^{Hot}\right)B \tag{8}$$

and

$$P_{out}^{Cold} = G\left(P^r + P_{in}^{Cold}\right)B\,. \tag{9}$$

The ratio of the two output powers is called the *Y-Factor* and is given by

$$Y = \frac{P_{out}^{Hot}}{P_{out}^{Cold}} = \frac{P^r + P_{in}^{Hot}}{P^r + P_{in}^{Cold}}\,. \tag{10}$$

Re-writing this equation, the noise power of the receiver system, referred to the input, is

$$P^r = \frac{P_{in}^{Hot} - Y P_{in}^{Cold}}{Y - 1}\,. \tag{11}$$

Using (6), the receiver noise temperature is found simply by

$$T^r = \frac{P^r}{kB}. \tag{12}$$

Notice that, in this definition, there is no dependence on a noiseless source and, since power definitions are used, it accounts for the zero-point fluctuations if the Callen and Welton expression is used. One may also re-write the Y-factor equation to solve for the receiver noise temperature directly. In this writing, the temperatures, T^{Hot} and T^{Cold}, are the noise temperatures and not the physical temperatures. The receiver noise temperature is then

$$T^r = \frac{T^{Hot} - YT^{Cold}}{Y-1}. \tag{13}$$

In practice, the calibration input signals, P_{in}^{Hot} and P_{in}^{Cold}, are established by using some type of microwave absorber at room temperature (290 K) and another absorber that is soaked in liquid Nitrogen (77 K). From (1) it can be seen that it is important to find a material that has very low reflection properties at the frequency of interest. The better absorption properties of the material, the closer the radiation signal will approach the black-body radiation ideal, so that the above equations can be used with confidence.

Consider the effect of several components arranged in a cascaded configuration, each with an equivalent noise temperature, $T_1, T_2, T_3, \ldots$, corresponding to the first, second, and subsequent stages. If an input source with noise temperature T_0 is applied, the output system noise power is

$$\begin{aligned} N^{Output} &= G_1 k(T_0 + T_1)B + G_2 kT_2 B + G_3 kT_3 B + \ldots \\ &= G_{cas} k(T_0 + T_{cas})B \end{aligned} \tag{14}$$

where

$$\begin{aligned} G_{cas} &= G_1 \cdot G_2 \cdot G_3 \cdot \ldots \\ T_{cas} &= T_1 + \frac{T_2}{G_1} + \frac{T_3}{G_1 G_2} + \ldots \end{aligned} \tag{15}$$

2.1.4 DSB, SSB and 2SB Noise

There are generally three operational modes of heterodyne receivers: double-sideband (DSB), single-sideband (SSB) and sideband-separating (2SB). In the DSB mode, both sidebands, the upper and lower, are converted to the intermediate frequency (IF), i.e., both sidebands are overlaid on top of one another in the IF band. The DSB receiver is the simplest configuration and is used for continuum measurements (DSB operation) or for observing a narrow band signal that is present in only one of the bands (SSB operation). A single-sideband receiver filters off one of the bands in the front end (e.g., through an image rejection filter). The sideband-separating operation is the most complex receiver and allows the user to discriminate between the two sidebands. One can see the potential problems in comparing receiver noise performance between different types of receivers. The following is a summary from [31] that allows for a consistent definition.

When the Y-factor method is used to measure a DSB receiver, the receiver is operating in a continuum or DSB configuration. This means that (13) gives the DSB receiver noise temperature of a DSB receiver. However, if the Y-factor method is used for a SSB receiver, equation (13) will then indicate the SSB receiver noise temperature of a SSB receiver. When comparing a DSB receiver with a SSB receiver, it is useful to refer all of the noise to one sideband, so that for a DSB receiver

$$T_{SSB}^{r} = T_{DSB}^{r}\left(1+\frac{G_i}{G_s}\right) = T_{DSB}^{r}\left(1+\frac{1}{R}\right) \tag{16}$$

where R is the *sideband ratio* and G_s and G_i are the conversion gains of the *signal* and *image* signal. Only in this way, can a DSB receiver be compared with a SSB receiver. If the conversion gains of the image and signal bands are equal, then

$$T_{SSB}^{r} = 2 \cdot T_{DSB}^{r}. \tag{17}$$

If a DSB receiver is operating in a narrow band, or SSB mode, then the receiver noise can no longer be easily obtained using the Y-factor method. Only a *system* noise temperature can be derived, which now includes the input temperatures of the signal and image, T_s and T_i, and is given as

$$T_{SSB}^{sys} = \frac{P_{out}}{kBG_s} = T_s + T_i\left(\frac{G_i}{G_s}\right) + T_{SSB}^{r}. \tag{18}$$

In this case, the noise temperature of the receiver system cannot be directly compared with the other two configurations mentioned above.

The sideband-separating receiver has a configuration so that the sideband separation is caused by an in-phase addition and an out-of-phase subtraction. If this re-combination and simultaneous subtraction (or rejection) is ideal, then the receiver noise can be predicted as in the case of a SSB receiver using the Y-factor method. In reality, however, there is some leakage of the unwanted sideband into the IF. The sideband rejection ratio, as shown in (16), is used to determine the quality of the sideband re-combination and rejection. Considering the leakage of the unwanted sideband, the Y-factor measurement of a 2SB receiver is really a DSB measurement, and to correct for this the following expression

$$T_{SSB}^{r} = T_{DSB}^{r}\left(1 + \frac{1}{R_n}\right) \tag{19}$$

is used where R_n is the image rejection corresponding to each IF output (i.e., $n = 1,2$) [42].

2.2 Double-Sideband (DSB) Measurements

The double-sideband receiver is the building block of the sideband-separating receiver, and so it is constructive to explore the DSB setup and measurement procedure first.

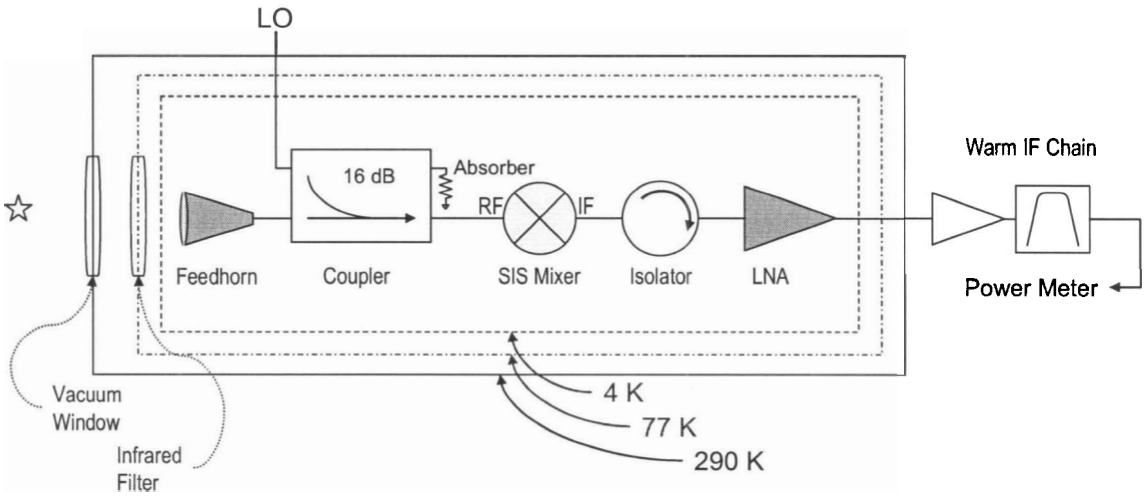

Fig. 3. Block diagram of the double-sideband receiver

Fig. 3 shows the configuration when the receiver is set up for double-sideband reception. The diagram represents four main areas: the front end optics, front end RF, cold IF and warm IF chain. In order for the receiver to have the lowest noise possible, and thereby the best sensitivity, all critical components are mechanically affixed to the cold plate. The cold plate is housed within a two-stage wet cryostat and is maintained at a temperature of 4.2 K. Liquid nitrogen and liquid helium are used, whose boiling points are 77 K and 4.2 K, respectively. Special care is given to reduce the amount of heat transfer from room temperature to inside the cryostat. All wiring and waveguide feed-throughs that extend from outside are manufactured from metals with low thermal conductivity, such as stainless steel and beryllium copper, to reduce conductive heat transfer. Radiative heat transfer is reduced by ensuring that the cold plate and inner radiation shield are constructed from shiny materials with low emissivity. Finally, to eliminate heat loading caused by convection, the inside of the cryostat is held under high vacuum (approximately 10^{-5} Torr or less).

For the experiment contained within this thesis, the front end optics are very simple. As a consequence of the vacuum, the incoming electromagnetic waves are forced through a vacuum window (usually created with Mylar or Melinex film). Next in line is the infrared filter constructed from a Gortex disk. It is important to ensure that the losses and reflections due to the window and IR filter are kept to a minimum. In fact, as can be seen

from (15), any losses that come before the LNA will have a strong impact on the noise temperature of the receiver.

Following the optics, the front end RF section of the receiver consists of a feedhorn, directional coupler and the mixer. The local oscillator signal is established by using a Gunn or YIG oscillator and is then combined with the incoming RF through a 16 dB branch-guide waveguide coupler. Note that the value of the LO coupling was chosen as a trade-off between LO signal power, amount of cold attenuation and machining constraints of the waveguide slots (C.F. Sec. 2.2.1). The *thru* part of the coupler is terminated with a wedge type microwave absorber (with input reflection loss of 24 dB or better). The mixer chip is contained within a split block that has a waveguide input and an IF output. A stripline probe extending into the waveguide allows for the coupling of the incoming signal onto the mixer chip. Since the mixer is sensitive to the output impedance match, a cryogenic isolator is used. Finally, a cryogenic low noise amplifier (LNA) is used providing some gain before the signal exits the cryostat. Completing the receiver is the warm IF chain [51], which gives further amplification and filtering (broadband or narrowband).

2.2.1 DSB Noise Analysis

It is desirable to examine the contributions of the noise temperature from each component within the receiver. Please note that in the calculations that follow, the Rayleigh-Jeans approximation has been used. Since the highest frequency is 116 GHz, and the coldest physical temperature used within the Y-Factor measurement is 77 K (for liquid nitrogen), the difference between the Callen and Welton noise temperature and the physical temperature is negligible. This can also be deduced from Fig. 1.

Using the cascaded formulation given in (15), one can calculate the noise contribution of each component in the receiver chain. Note that for passive components, the noise temperature is given by

$$T_e = (L-1)T. \tag{20}$$

Fig. 4 shows the noise budget estimate for the DSB receiver, but does not show the contribution of noise due to the local oscillator noise. One can see that the mixer and LNA have the most dominance. Since the noise temperature of a cascaded component is

divided by the cascaded gain of the previous elements, the noise temperature contribution of any element following the LNA is greatly reduced. Likewise, components in between the mixer and the LNA have their noise contributions increased because of the cascaded loss (mostly due to the conversion loss of the mixer). This can be seen by comparing the T_e column with the *Contribution* column.

Component	Phys. Temp. (K)	Gain (dB)	Te (K)	Gcas (dB)	Tcas (K)	Contribution (K)
Vacuum window	290	-0.02	1.338579181	-0.02	1.3386	1.3386
IR Filter (77K)	77	-0.03	0.533738502	-0.05	1.8748	0.5362
FH (4.2 K)	4.2	-0.03	0.029113009	-0.08	1.9042	0.0295
Coupler	-	-0.15	0.03	-0.23	1.9348	0.0306
Mixer	-	-1	5	-1.23	7.2067	5.2719
IF Cable 1	4.2	-0.1	0.097830568	-1.33	7.3366	0.1299
Isolator	4.2	-0.5	0.512477508	-1.83	8.0327	0.6961
IF cable 2	4.2	-0.1	0.097830568	-1.93	8.1818	0.1491
LNA	-	35	4	33.07	14.4200	6.2382
IF Cable 3	290	-2.5	225.7010289	30.57	14.5313	0.1113
Warm IF	-	60	627.0605214	90.57	15.0812	0.5499

Fig. 4. Expected losses of DSB receiver without LO coupling noise.

The equivalent noise temperatures, T_e, have been calculated using (20), except where **specified (highlighted).** Notice that the coupler has been specified with a noise temperature due to the conductive losses of the waveguide and not due to the coupling loss. The cryogenic low noise amplifier has been developed within HIA (based on a NRAO design [48]) and has a noise temperature of 4 K across the IF band of 4-8 GHz. The row entitled *Warm IF* signifies the warm IF chain described above and has been characterized with a 5 dB noise figure and 60 dB gain, where the noise figure has been converted into a noise temperature. Note that to convert between noise figure, F, and noise temperature the following expression is used:

$$T_e = (F-1)290. \qquad (21)$$

It has been found experimentally that the SIS mixers used within the Band 3 project have noise temperatures ranging from 5 to 10 K and 0.8 to 3.0 dB conversion loss [48]. Taking the best and worst cases, the overall cascaded noise, without including the LO, is predicted over the range of 14.7 K to 25.0 K.

To account for the noise increase due to the local oscillator signal coupled into the RF path, the simple cascaded formula can not be used by itself. A different approach, using

the Y-factor technique is used [50]. The noise power from the LO is added at the input to the mixer during each of the hot and cold measurements, so that the power input to the mixer for each scenario is

$$P_{MixerInput}^{Hot} = G_{FE}kB(T_{Hot} + T_{FE}) + G_{LO}kBT_{LO} \tag{22}$$

and

$$P_{MixerInput}^{Cold} = G_{FE}kB(T_{Cold} + T_{FE}) + G_{LO}kBT_{LO} \tag{23}$$

where *FE* refers to the components before the mixer, *LO* refers to the components along the local oscillator chain (including the coupling), and *Hot* and *Cold* refer to the calibration loads used for the Y-factor measurement. The rest of the receiver chain, which includes the mixer and the IF chain, is denoted as *MxIF* so that the total received power is

$$P_{out}^{Hot} = G_{MxIF}P_{MixerInput}^{Hot} + G_{MxIF}kBT_{MxIF} \tag{24}$$

and

$$P_{out}^{Cold} = G_{MxIF}P_{MixerInput}^{Cold} + G_{MxIF}kBT_{MxIF}\,. \tag{25}$$

Now, equations (10) and (13) can be used to find the receiver *system* noise temperature. An important result of this analysis is that the noise contribution to the system noise temperature due to the LO can be reduced by the value of LO coupling. The problem is that for lower coupling, the slots in the branch-guide coupler need to become narrower, which becomes infeasible for CNC milling machines (Electrical Discharge Machining (EDM) may be used). However, by adding a cold attenuator, as shown in the worksheet of Fig. 5, this same kind of effect can be observed (although it would be the best to accomplish this using the coupler alone).

The LO chain is composed of a signal source (a Gunn or YIG oscillator), room temperature copper waveguide, stainless steel waveguide (providing the feed-through into the cryostat), copper waveguide and coupler. Stainless steel guides are used because of their poor thermal conduction so that a temperature gradient is established across them. The calculations below simplify the gradient to a step approximation. Again, the noise

temperature for the coupler has been specified according to the conductor loss due to the waveguide, and not as if it was a 16 dB absorber.

Since the LO coupler is strapped to the 4 K cold plate, there is already some inherent cold attenuation due to the conductive losses. The cold attenuator may take the form of an absorber wedge placed inside the LO waveguide (see Appendix B for possible designs); the waveguide and attenuator are also at 4 K. Fig. 5 describes a typical worksheet that may be used to calculate the cascaded noise temperature with a cold attenuator value of 10 dB. Considering the plot of Fig. 6, choosing the value of the cold attenuator between 6 and 10 dB appears to give the best tradeoff between power and noise reduction, and so this was implemented in the experiment below.

In total, when the value of the cold attenuator is set at 8 dB for a 16 dB LO coupler, the receiver noise (if the mixer is calculated with 0.8 to 3.0 dB conversion loss and 5 to 10 K noise temperature) varies from 15.8 K to 26.0 K. Note that Fig. 6 was calculated with the mixer at 1.0 dB conversion loss and 5 K equivalent noise temperature.

LO Input Power					
Component	***Phys. Temp. (K)***	***Gain (dB)***	***Te (K)***	***Gcas (dB)***	***Tcas (K)***
Copper WG from Gunn	290	-0.1	6.755	-0.1	6.755
SS WG1 (290K)	290	-2	169.619	-2.1	180.325
SS WG2 (77K)	77	-1.5	31.765	-3.6	231.842
SS WG3 (4.2K)	4.2	-0.03	0.029	-3.63	231.909
Copper WG (4.2K)	4.2	-0.03	0.029	-3.66	231.976
Cold Atten	4.2	-10	37.800	-13.66	319.776
Coupler	4.2	-16	0.030	-29.66	320.472

T_LO_source	290		G_FE	-0.23
T_Hot_in	290		T_FE	1.9348
T_Cold_in	77		G_MxIF	90.8
BW	4.00E+09		T_MxIF	12.4683
P_Hot_MxInput	1.53E-11			
P_Cold_MxInput	4.17E-12			
P_Hot_out	1.93E-02		Y-Factor	3.296
P_Cold_out	5.84E-03		Tsys	15.777

Fig. 5. Example of worksheet to calculate LO contribution

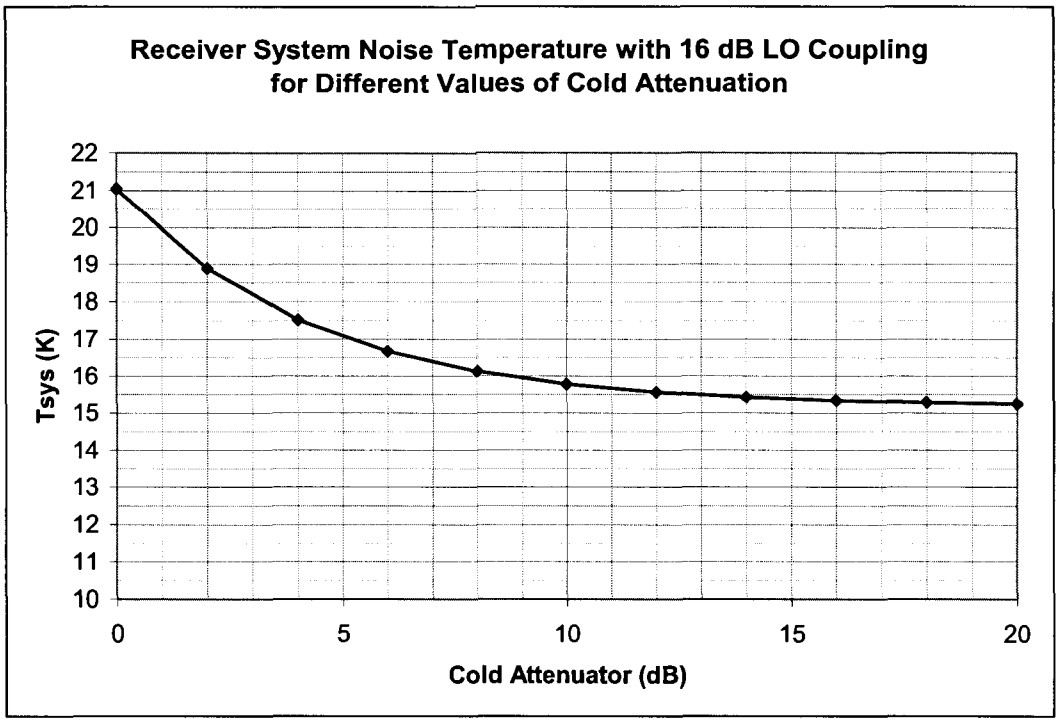

Fig. 6. System noise temperature for a 16 dB LO coupler combined with varying cold attenuation values.

2.2.2 DSB Measurement Setup and Results

The DSB experiment was performed using the J1 SIS mixer chip from the prototype SIS mixer wafer (N11-01-L1267B-0302). This mixer had been characterized previously and was known to exhibit very low noise temperature. The experiment given below was performed to verify the new HIA cryogenic LNA and a new biasing configuration (6-wire biasing of the mixer).

The biasing of the mixer was accomplished using a bias-tee network within the amplifier. The DC bias is applied through the IF cable, passing through the IF port of the mixer and then terminated to ground after the junction. Fig. 7 shows the inside of the cryostat assembled for the DSB measurement. Critical items are labeled and described below:

1. **WR-10 Feedhorn** – shown facing the infrared filter.
2. **LO Coupler Block** - it is hard to see, but the LO waveguide, feedhorn and mixer all attach to this branch-guide coupler (it is underneath the rectangular bracket).

3. **SIS mixer** – the mixer chip sits inside the mixer block that has been thermally strapped to the cold plate.
4. **Cryogenic Isolator** – manufactured by Pamtech (S/N 162R). The mixer DC bias traveling along the semi-rigid cable is able to pass through the isolator.
5. **Cryogenic LNA** – serial number HIA0012.
6. **LO Waveguide (Gold)** – comprised of three different waveguide sections, this guide is strapped to the cold plate. Since the entire guide is gold-plated copper, there is no temperature gradient across it (or a very small gradient) and its temperature is that of the cold plate.
7. **LO Waveguide Feed-through (Stainless Steel)** – extends from outside to inside of the cryostat. The guide is thermally strapped to the radiation shield at its midpoint so a temperature gradient from 290 to 77 K and 77 to 4.2 K will be established across it.
8. **IF Cabling** – these cables have TIG-welded connectors for cryogenic durability and the inner and outer conductors are copper. Again, no gradient is across these cables.
9. **IF Cabling** – same as 8.
10. **IF Cabling Feed-through** – this IF cable extends through the cryostat. As thermal isolation from room temperature is necessary, this cable has stainless steel inner and outer conductors. As a result, attenuation is higher, but since this cable follows the amplifier, it has a negligible effect on increasing the system noise temperature. Just like the LO waveguide, there are thermal straps to the radiation shield (77 K) and the cold plate (4.2 K).
11. **Cryogenic Wiring** – made of beryllium copper, the wire has a low thermal conductivity and is used for the LNA, mixer and temperature sensors.
12. **Temperature Sensor** – the sensor shown is attached directly to the cold plate and can accurately read temperatures of liquid nitrogen and helium. There is another sensor on top of the LO coupler (not shown) to get an indication of how well the components are cooling.

Each component is mounted onto the cold plate using copper brackets that have high thermal conductivity. Heat straps are made with tinned copper braiding and can be

soldered directly to the cables and brackets to aid in cooling. It is important to tie down any lose wires because the cryostat is flipped upside-down before filling it with the liquids. Dangling wires may cause thermal shorts between the radiation shield and the cold plate or other components. Wherever possible, brass screws were used in order to get a closer match of the coefficient of thermal expansion (CTE) between the different metals to maintain strong thermal contact over cooling. If stainless steel screws were used, compression washers, e.g., Belleville washers, were used to maintain a strong thermal connection over temperature.

Fig. 7. ostat assembly of the DSB receiver.

Since the Y-factor measurement technique was used, hot and cold calibration loads were created out of Eccosorb AN-72 absorber and shaped into a cone. During measurement, the cold load was soaked in liquid nitrogen and then quickly placed around the RF window.

Fig. 8 shows the results of the broadband, double-sideband measurement for the mixer J1, with a measurement bandwidth of 4 GHz. To cover the entire RF frequency range of 84-116 GHz, the LO frequency had to extend from 92-108 GHz with an IF frequency range of 4-8 GHz. Two different Gunn oscillators were necessary to cover the entire spectrum. One can see excellent agreement between the noise measurements as each result of the two different Gunn oscillators at 100 GHz are overlaid on top of each other. A ferrite wedge absorber was used in the LO chain, pointing towards the LO source, to ensure low reflections and provide better LO stability. The most likely reason for the roll-off in noise temperature is due to the variation of conversion loss for the mixer (higher loss at lower frequencies).

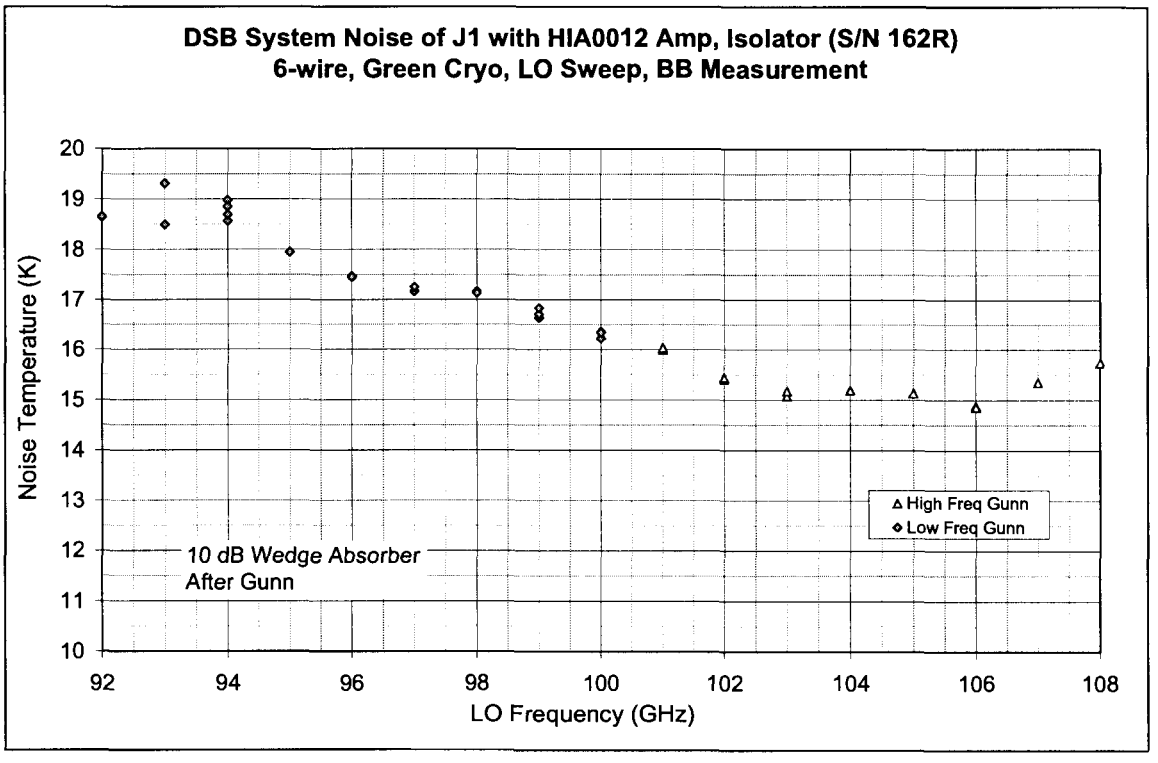

Fig. 8. Broadband DSB noise temperature using Mixer J1.

2.3 Sideband-Separating (2SB) Measurements

To expand the usefulness of the receiver, a sideband-separating (2SB) architecture can be used to separate the upper and lower sidebands for individual observation. The design is the phase cancellation type using waveguide hybrids, as described in [41], [48] and shown in Fig. 9.

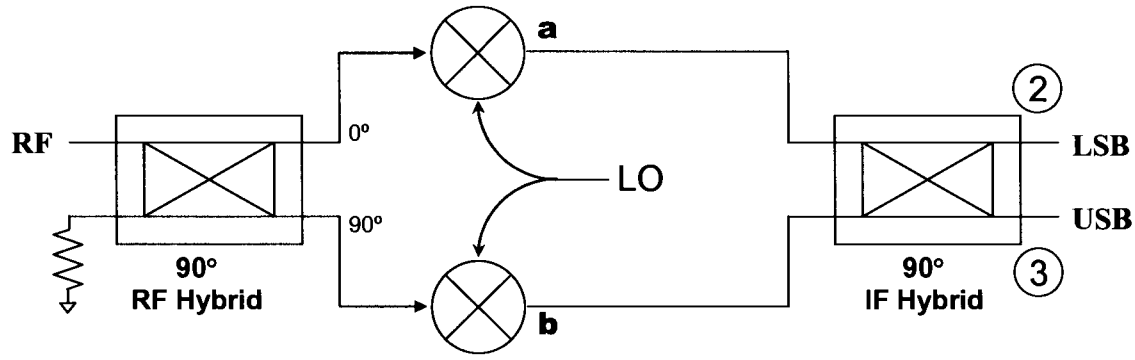

Fig. 9. Phase-cancellation 2SB architecture.

In this approach, the incoming RF is divided in half using a branch-guide 3 dB coupler so that the outputs have a 90° phase difference. Since the hybrid is strapped to the cold plate of the cryostat, the absorber used to terminate the isolated port adds little noise. The LO source is split in-phase using an E-plane power divider. The downconverted signals, *a* and *b*, are then routed through a 90° IF hybrid. It is important that the path lengths of the upper and lower paths are matched. Each sideband is followed by identical IF chains consisting of an isolator, LNA, and warm IF section, as seen in Fig. 3.

To demonstrate the sideband separation, consider the following. Let the input RF signal be represented as $\cos\omega_{RF}t$ and the LO source as $\cos\omega_{LO}t$. The signals input to the mixer chip are

$$a_{RF} = \frac{1}{\sqrt{2}}\cos\omega_{RF}t + \cos\omega_{LO}t \tag{26}$$

and

$$b_{RF} = \frac{1}{\sqrt{2}}\cos(\omega_{RF}t + 90) + \cos\omega_{LO}t\,. \tag{27}$$

Ignoring the DC and higher-order terms, the down-converted IF products are

$$a = C\left[\cos(\omega_{RF} + \omega_{LO})t + \cos(\omega_{RF} - \omega_{LO})t\right] \tag{28}$$

and

$$b = C\left[\cos(\omega_{RF}t + 90 + \omega_{LO}t) + \cos(\omega_{RF}t + 90 - \omega_{LO}t)\right] \tag{29}$$

where C represents a scaling factor and includes the conversion loss of the mixer. Consider the case of the upper sideband signal (USB), $\omega_{RF} = \omega_{LO} + \omega_{IF}$, then the output signals of the IF hybrid at ports 2 and 3 are

$$\begin{aligned} S_2^{USB} &= \left(\frac{a}{\sqrt{2}}\right)_{+90^\circ} + \left(\frac{b}{\sqrt{2}}\right)_{+180^\circ} \\ &= \frac{C}{\sqrt{2}}\left[\cos(2\omega_{LO} + \omega_{IF} + 90)t + \cos(\omega_{IF} + 90)t\right] + \frac{C}{\sqrt{2}}\begin{bmatrix}\cos(2\omega_{LO}t + 270 + \omega_{IF}t) \\ +\cos(\omega_{IF}t + 270)\end{bmatrix} \\ &= 0 \end{aligned}$$

and

$$\begin{aligned} S_3^{USB} &= \left(\frac{a}{\sqrt{2}}\right)_{+180^\circ} + \left(\frac{b}{\sqrt{2}}\right)_{+90^\circ} \\ &= \frac{C}{\sqrt{2}}\left[\cos(2\omega_{LO} + \omega_{IF} + 180)t + \cos(\omega_{IF} + 180)t\right] + \frac{C}{\sqrt{2}}\begin{bmatrix}\cos(2\omega_{LO}t + 180 + \omega_{IF}t) \\ +\cos(\omega_{IF}t + 180)\end{bmatrix} \\ &= \sqrt{2}C\left[\cos(2\omega_{LO} + \omega_{IF} + 180)t + \cos(\omega_{IF} + 180)t\right]. \end{aligned}$$

Therefore, the USB signal cancels because of out-of-phase addition at port 2, but combines at port 3. Similarly, for the lower sideband (LSB), $\omega_{RF} = \omega_{LO} - \omega_{IF}$, port 3 shows cancellation, but port 2 recombines. In this way the two sidebands are separated from one another.

2.3.1 2SB Noise Analysis

The 2SB setup adds some complexity to the noise analysis and may be analyzed in detail by combining the cascaded noise theory and using the Y-factor equations as shown above for the DSB LO coupling analysis. However, assuming that the noise temperature of each individual sideband path is very similar to the DSB receiver performance, a reasonable prediction using (19) can be made. The image rejection ratios are defined as

$$R_1 = \frac{G_1^{USB}}{G_1^{LSB}} \quad \text{and} \quad R_2 = \frac{G_2^{LSB}}{G_2^{USB}} \tag{30}$$

where it is assumed that IF port 1 is supposed to receive the upper-sideband, as depicted in Fig. 10. In [42], an effective method to measure the sideband ratios has been presented using a sideband interferer source (where the precise power level of the interferer does not need to be known). This technique has been used in the measurements provided below.

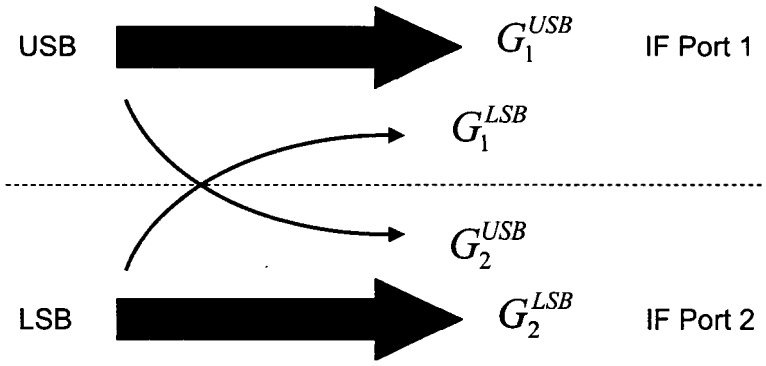

Fig. 10. Conversion gains for the 2SB receiver.

Referring back to Fig. 9, the quality of the image rejection for each sideband relies on equal amplitude division and identical phase paths. Special care is given in the mechanical assembly of the 2SB receiver to ensure that IF cables are phase matched and that the power dividers are symmetric (after the IF hybrid this is no longer a concern). Fig. 11 shows the expected image rejection ratios for given phase and amplitudes imbalances.

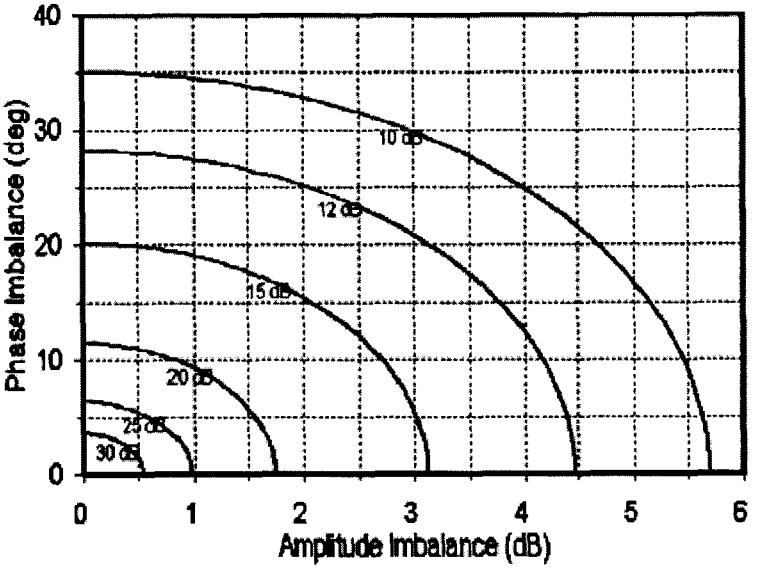

Fig. 11. Dependence of image rejection on phase and amplitude imbalances. Figure taken from [41].

2.3.2 2SB Measurement Setup and Results

All of the same techniques for assembly and cooling, as previously shown for the DSB receiver, apply for the 2SB assembly. A close-up of the sideband-separating assembly is shown in Fig. 12 – two mixers are attached to the RF hybrid block whose IF outputs are routed to the IF hybrid using phase-matched cables. The RF hybrid block consists of an input 3 dB branch guide splitter, an E-plane splitter for the LO signal and two 16 dB couplers to combine the LO and RF together. Fig. 13 shows the complete setup of the 2SB components within the cryostat where, after the IF hybrid, the two IF paths (each containing one sideband) are identical. Labeling of the components is as follows: 1) feedhorn, 2) sideband-separating assembly, 3) cryogenic IF isolator, 4) cryogenic low-noise amplifier, 5) LO waveguide and 6) output IF cabling.

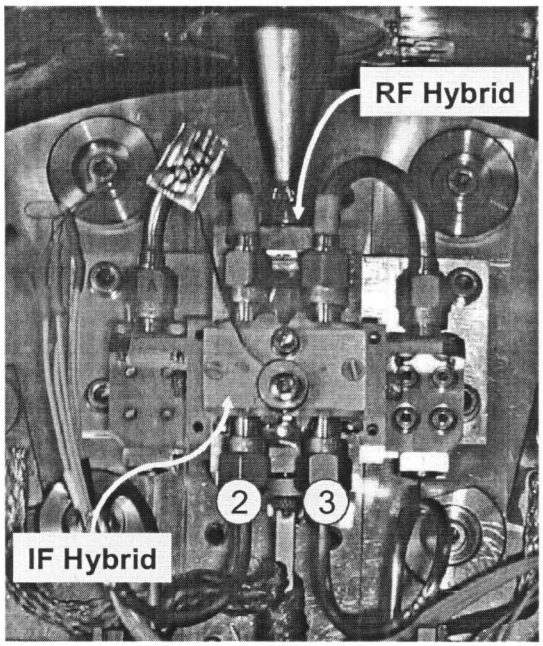

(a)

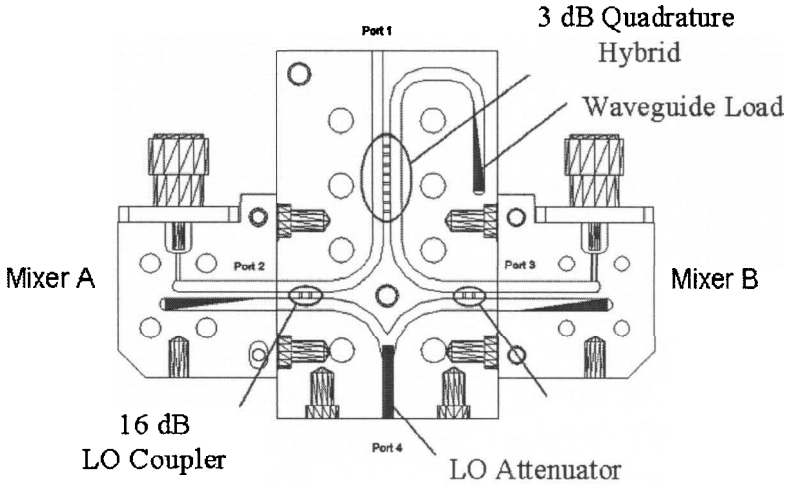

(b)

Fig. 12. (a) View of the sideband-separating assembly within the cryostat. The IF hybrid is mounted on top of the RF hybrid, and the SMA cables are phase matched. (b) Split block view of the mixer and RF hybrid.

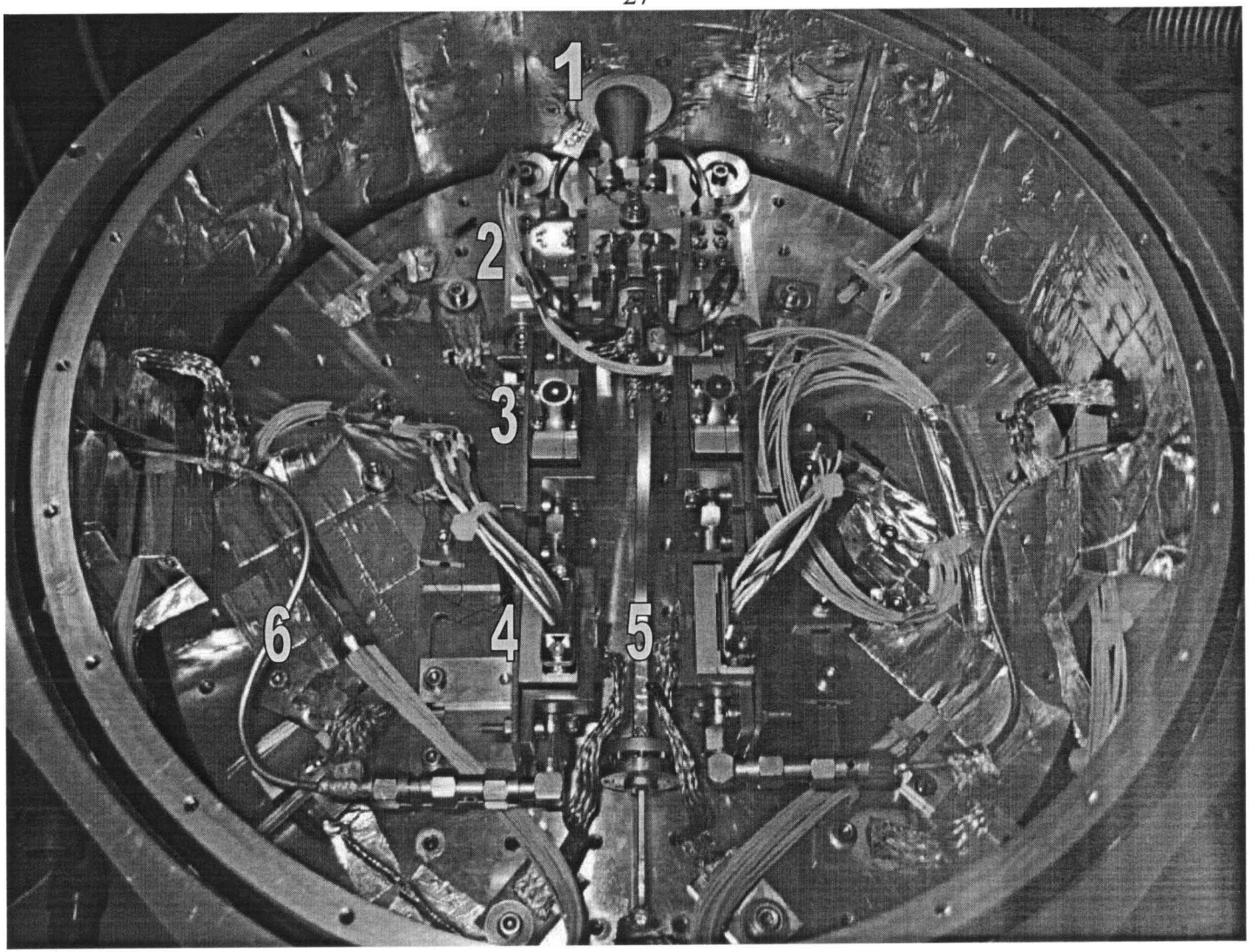

Fig. 13. ostat assembly of the 2SB receiver.

The 2SB receiver was tested, for each channel, in the fashion already described. Fig. 14 shows the broadband noise temperature for each sideband output. Channel 1 contains the USB and channel 2 contains the LSB.

In the measurements, the low and high frequency Gunn oscillators were used over the range of 92-95 GHz and 96-108 GHz respectively. The mixers used for this 2SB measurement have been measured separately and the DSB results are presented in Appendix A. From the theory already discussed, it is expected that the 2SB results should be approximately twice that of the DSB measurements, which is what is indicated in the plot below. Fig. 15 is similar except that only a narrow bandwidth of 40 MHz, centered in the middle of the IF band, has been sampled. Fig. 16 and Fig. 17 show how the narrowband noise temperature varies across the IF band for three different LO frequencies: 92, 100 and 108 GHz.

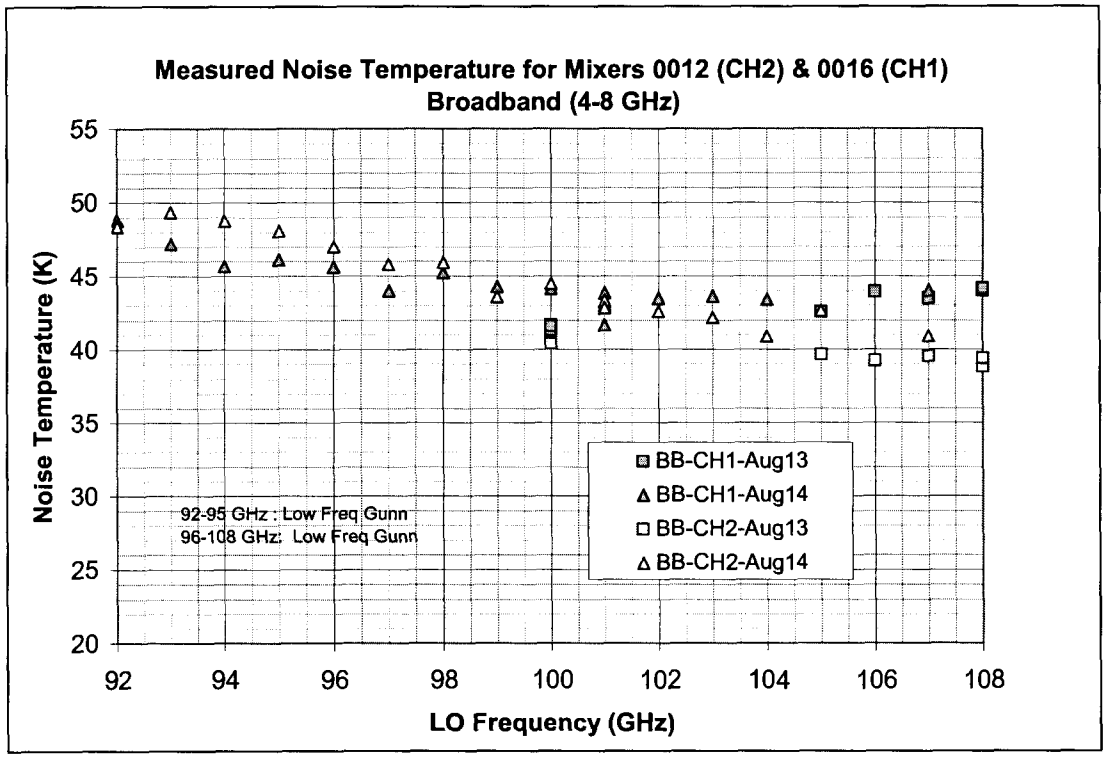

Fig. 14. Broadband noise temperature of the 2SB receiver for different LO frequencies.

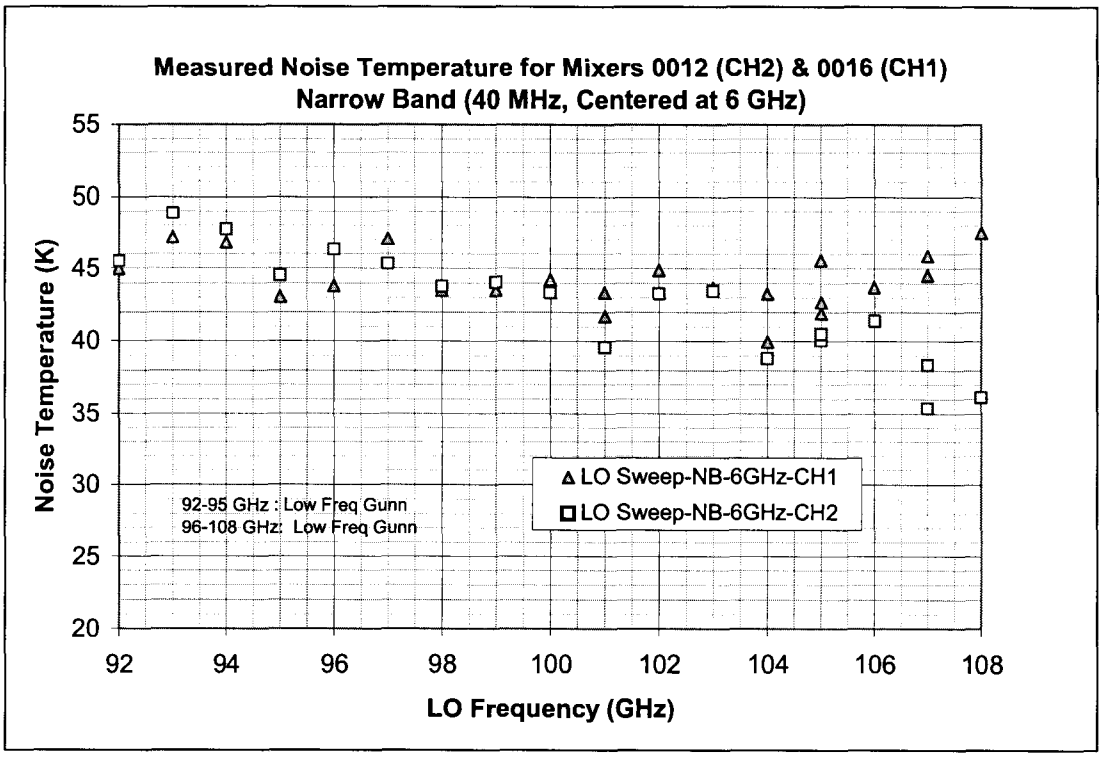

Fig. 15. Narrow band (40 MHz, Fc=6 GHz) noise of 2SB receiver vs. LO frequency.

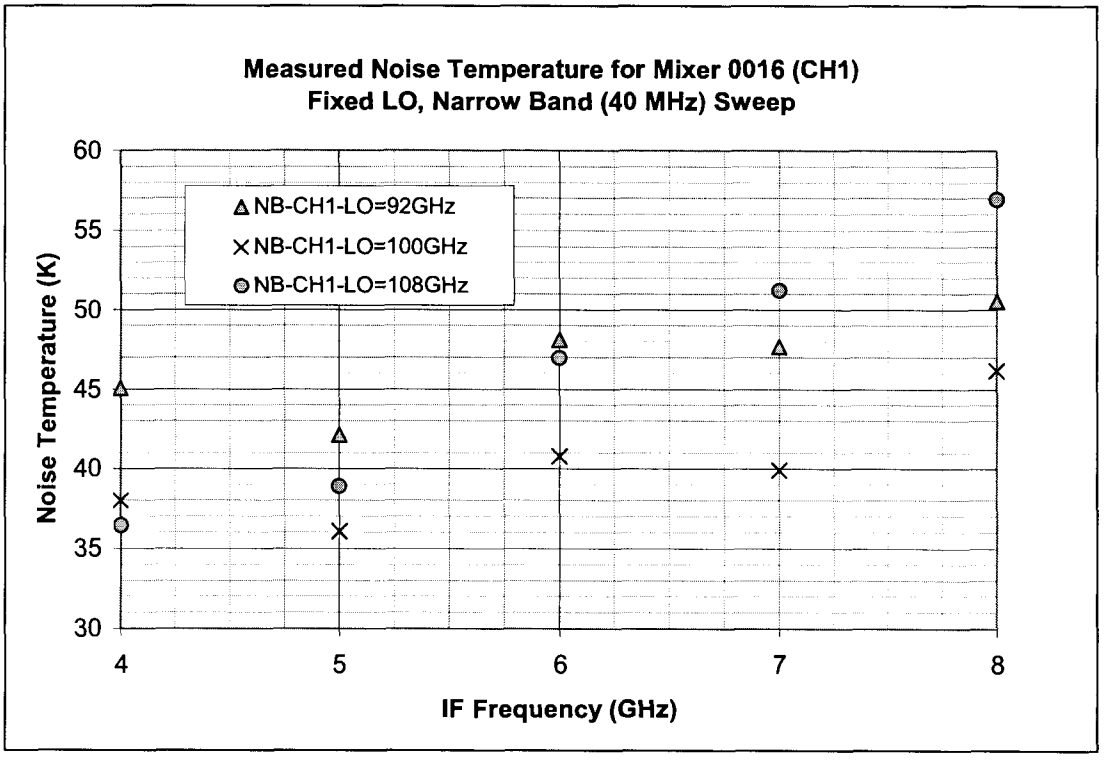

Fig. 16. Narrow band sweep for fixed LO frequencies - Channel 1.

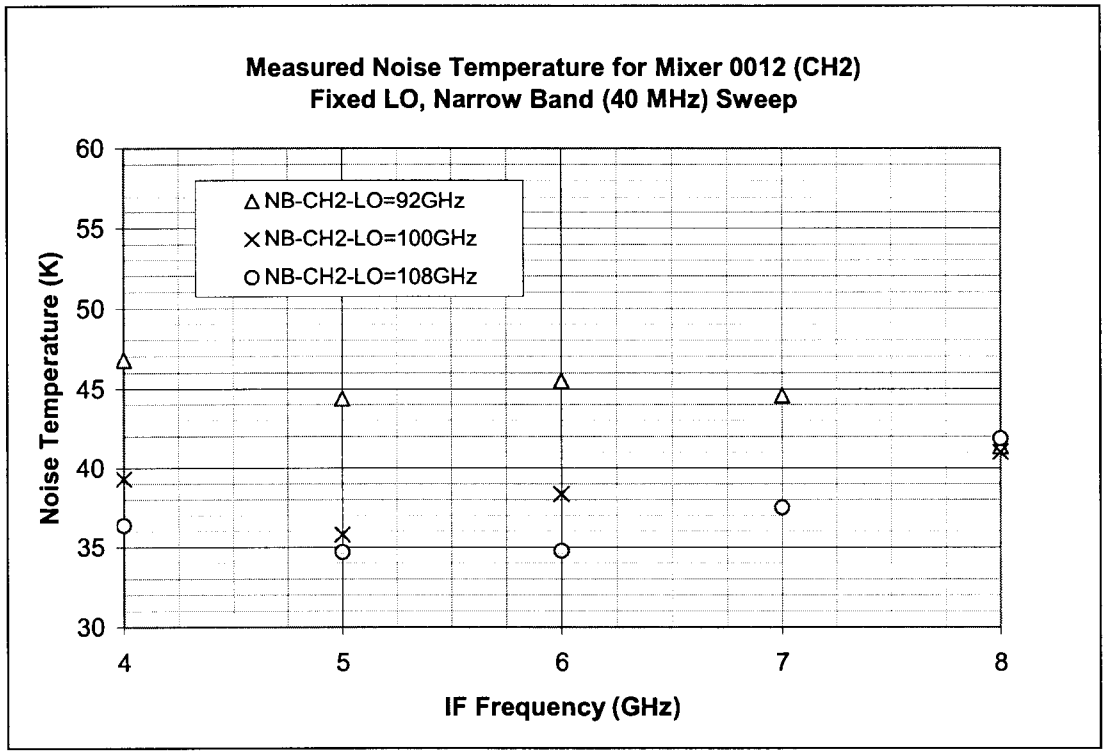

Fig. 17. Narrow band sweep for fixed LO frequencies - Channel 2.

Note that the above graphs have **not** been corrected using the image rejection ratios as described in equations (19) and (30). These ratios were measured and are given in Fig. 18. If the sideband rejection is 10 dB, the noise temperatures would be increased by 10%; for a rejection of 15 dB, the correction is only 3%. The lowest measured ratio is approx 13.4 dB, which would take a 45 K measurement and correct it to 47 K.

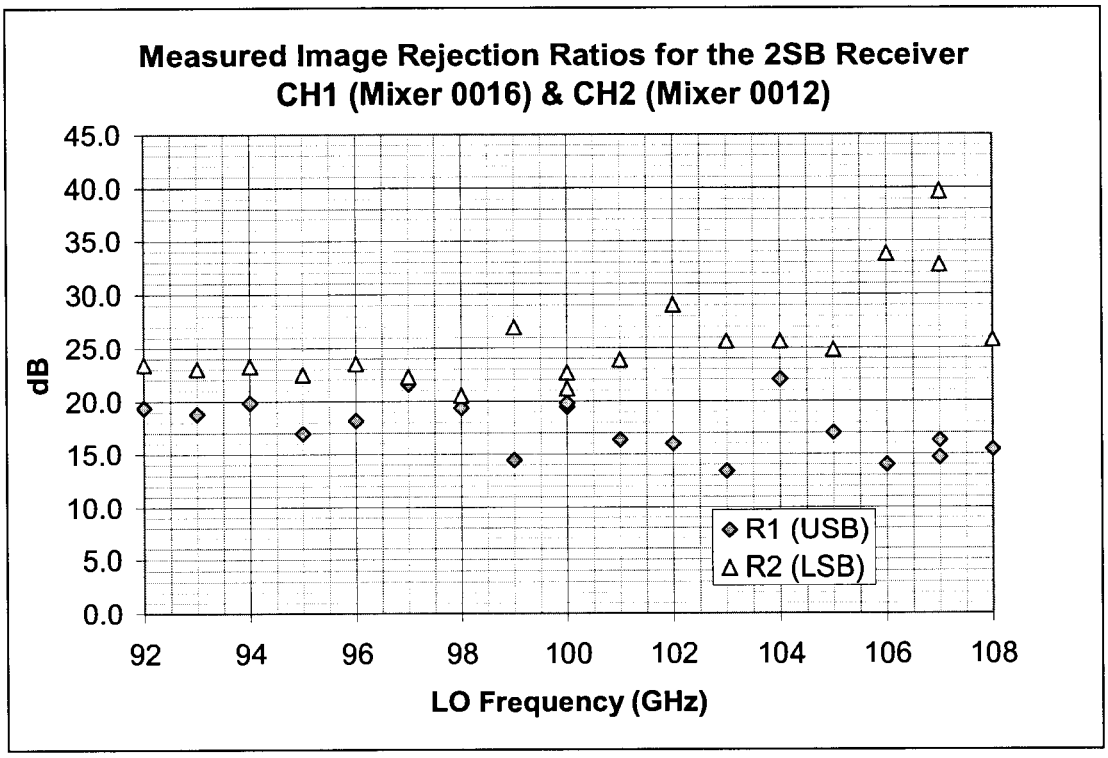

Fig. 18. Measured sideband rejection ratios for the 2SB receiver.

2.4 Conclusion

Although a great effort was made to reduce as many measurement inaccuracies as possible, there are many possible factors that may contribute to measurement error. In terms of the calibration loads, slight heating of the cold load, reflections of the vacuum window and non-ideal black-body characteristics of the absorber will create variation in the results. It is possible that signal leakage (RF or IF) into the receiver path or some internal spurious signal will cause some problems. Furthermore, the phase noise of the LO or poor Gunn oscillator tuning, may degrade the measurement. By matching the Gunn source with a waveguide attenuator, better stability of the source was observed.

3 SIS Mixing Junctions

In the previous section, the SIS receiver was analyzed at a component block level so that the performance of the SIS junction was treated as part of the *mixer block*. The block consists of an input waveguide section, chip substrate and output IF section. The junction itself comprises only a very small part of the chip, which is mostly a network of strip transmission lines to properly match, bias, and filter the output of the superconducting junction. Therefore, to understand and predict the performance of the mixer block, it is necessary to consider the detailed theory of the junction itself.

3.1 Superconducting Principles

Shortly after Kamerlingh Onnes was able to first liquefy helium in 1908, he observed a sudden drop in the resistivity of mercury when it was super-cooled. This discovery broke open the vast realm of low temperature physics. A prominent area of this research is that of *superconductivity* whereby certain elements and compounds exhibit a zero DC resistance below a certain temperature, called the *critical temperature*, T_c [6], [7], [8]. Fig. 19 shows a comparison of different critical temperatures for some pure elements and compounds. It is important to notice the great variation of temperatures between each listed. Since the most common cryogenic liquids are liquid helium and liquid nitrogen (normal boiling points of 4.2 and 77 K respectively), to have practical laboratory application, the element or compound must have a transition temperature that is greater than the boiling point of liquid helium (e.g., Nb).

Another unique and important phenomenon is that in the superconducting state, the magnetic flux is completely expelled from the superconductor. This is known as the *Meissner Effect* and leads to the definition of a *critical field*, H_c, which defines the point whereby any external magnetic field exceeding this value will destroy the superconducting state. There is a dependence of H_c on temperature (see Fig. 20) given by the expression

$$H_c(T) \approx H_c(0)\left[1-\left(\frac{T}{T_c}\right)^2\right] \tag{31}$$

where $H_c(0)$ is the critical field at absolute zero, given in Fig. 19.

Element	T_c (K)	H_c (Gauss)
Al	1.196	99
Cd	0.56	30
Ga	1.091	51
α-Hg	4.15	411
β-Hg	3.95	339
Nb	9.26	1980
Pb	7.19	803
Rh	< 0.001	-
Sn	3.72	305
Zn	0.875	53
Zr	0.65	47

Compound	T_c (K)
Nb_3Sn	18.05
Nb_3Ge	22.3
NbN	16
NbO	1.2
$YBa_2Cu_3O_7$	90

Fig. 19. Values of the critical temperature, T_c, and critical magnetic field, H_c, for selected elements and compounds. The values are specified at absolute zero.

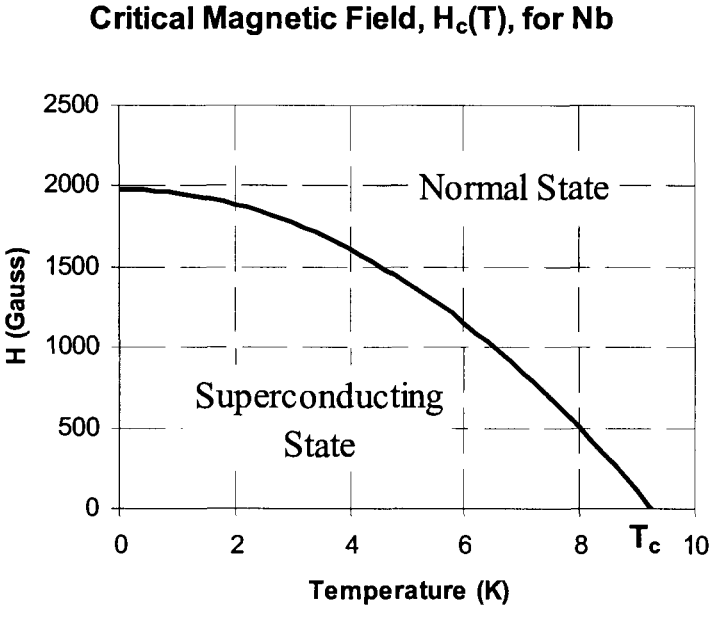

Fig. 20. Example of temperature dependence on the critical field, shown for niobium.

A further distinction on the type of superconductor is made on the basis of the sharpness of transition between the superconducting and normal state in the presence of a magnetic field. That is, if a magnetic field exceeding H_c is applied to a superconductor (cooled below T_c), and then is slowly reduced so that the external field falls below H_c, a

type I superconductor will show a sharp transition into the superconducting state as all penetrating magnetic flux is suddenly removed. Type II superconductors do not make such an immediate transition and the magnetic flux is only partially excluded as the superconductor transitions between its normal and superconducting states. This intermediate region is called the *vortex state*.

In 1957, Bardeen, Cooper and Schrieffer put forth a microscopic theory explaining the behavior of superconductivity in what is known as the *BCS theory* [5]. Within the superconductor, the Fermi sea (or collection of electrons occupying lowest available energy level) can become unstable. Though the electrons repel each other by their Coulombic force, they may become attracted via the crystal lattice at very low temperatures and form electron pairs. In other words, the electron interacts with the lattice causing the positive ions of the lattice to be displaced and, in effect, surround the electron by a cloud of positive charge. When the aggregate positive charge is of greater magnitude than the surrounded electron, another electron may attract. Note that at higher temperatures, thermal motion keeps the lattice from being polarized in this manner and pairs are not formed [8]. Another way of thinking about this interaction is by using a quantum description. An electron excites the energy state of the crystal lattice so that when it returns to its ground state a sound quanta of energy is released in the form of a phonon. It is this virtual exchange (emission and absorption) of a phonon between two electrons that binds the pair together creating what is also referred to as a *Cooper pair*. The BCS theory assumes that the coupling attraction between the paired electrons is weak (the Ginzburg-Landau theory treats the generalized case of strong coupling).

Recall the theory of semiconductors, which depicts an *energy gap* to describe a restricted energy region between the valence and conduction band. In a conductor, the conduction band is completely empty at 0 K, but as the temperature rises electrons are excited into the conduction band leaving behind an empty state, or hole, in the valence band. The motion of the electrons and holes account for the movement of charge. For an intrinsic semiconductor, the *Fermi energy level*, E_f, corresponds to the energy level midpoint of the energy gap. Probabilities of finding an electron at a given energy level are described by the *Fermi-Dirac distribution function*, $f(E)$. One may predict the

concentrations of electrons (and holes) over a range of energies using the distribution function and the *density of states*, $N(E)$ [9].

Similarly, for superconductors, the energy required to overcome the ground state of the Cooper pair (thereby breaking up the pair), describes the energy gap of the superconductor. The excited single electrons are called *quasiparticles* and the energy levels that they may fill are

$$E_k = \sqrt{\xi^2 + \Delta^2} \tag{32}$$

where ξ is the quasiparticle energy as measured from the Fermi energy and Δ is the energy gap parameter [7]. For a single particle, the minimum excitation energy is Δ, so that in order to break the pair, twice the amount is needed. The density of states is given as

$$N_S(E) = N_N(0)\frac{E}{\sqrt{E^2 - \Delta^2}} \tag{33}$$

where $N_N(0)$ is the normal metal density of states at the Fermi level. The superconductor density of states is shown for the example of tunneling in Fig. 23a.

The gap voltage is found from the measured I-V curve by looking at the point of maximum slope and is related to the energy gap as

$$V_g = \frac{E_g}{e} = \frac{2\Delta}{e} \tag{34}$$

where e is the electron charge. Depending on the temperature of the junction, the gap voltage will vary, illustrating that Δ is therefore dependent on temperature. As described by the BCS theory, this relation is approximately

$$\frac{\Delta(T)}{\Delta(0)} \approx \sqrt{\cos\left[\frac{\pi}{2}\left(\frac{T}{T_c}\right)^2\right]} \tag{35}$$

where $\Delta(0) = 1.76 k_B T_c$ and is plotted in Fig. 21 [43]. As the junction is cooled, the energy gap will increase, shifting the gap voltage higher (and thereby shifting the entire I-V curve), until the maximum of $\Delta(0)$ is reached. Recalling the critical temperature of

Nb, the plot of Fig. 21 justifies why Nb is so prevalent for use as a superconducting metal. At standard pressure, liquid helium will cool Nb to approximately 0.45 T_c resulting in little reduction of the energy gap. Using (34), the corresponding gap voltage for Nb at 4.2 K is found to be 2.66 mV.

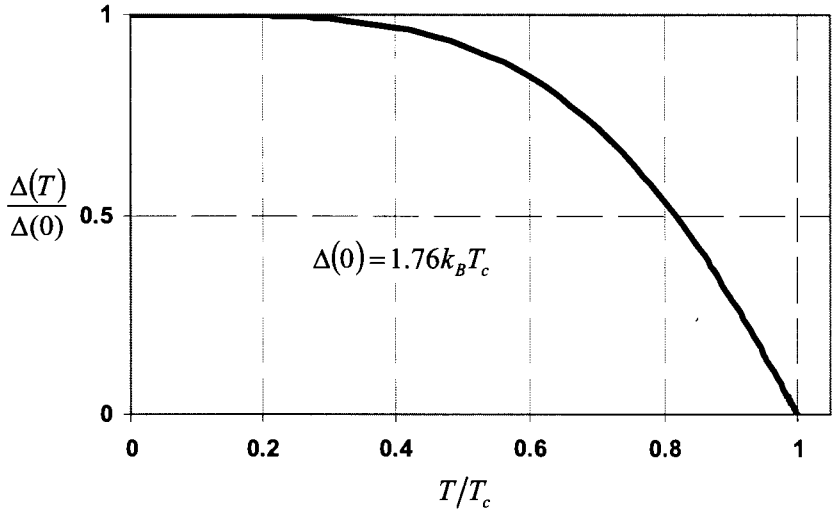

Fig. 21. Temperature dependence of the gap energy. As the temperature increases, the gap becomes smaller until reaching T_c, at which point the superconducting state is nullified.

3.2 Tunneling

When two sections of a superconductor are separated by a thin barrier of insulator (1-3 nm), the quantum effect of electron tunneling occurs [12]-[17]. SIS junctions, or more generally, *Josephson junctions*, have two tunneling currents: (1) the Cooper pair or the tunneling current that results when excited electrons tunnel in pairs, and (2) the quasiparticle or the single electron tunneling current. Cooper pair tunneling is also called *Josephson current* [4], [15]. When a DC current is applied across the junction, it will flow up to a maximum *critical current*, I_c, with no rise in voltage; this is called the *Josephson supercurrent.* Once the critical current is exceeded, the junction rapidly switches to the gap voltage. Above the gap voltage, the electron pair tunneling results in the *AC Josephson current* at a frequency of $\omega = 2eV_{DC}/\hbar$, or 484 GHz/mV. For SIS detectors, this AC current will interfere with mixing. If the receiving frequency is low enough (as in this thesis), the junction capacitance will shunt out the AC Josephson

current, otherwise a magnetic field can be used to suppress it. As a result, the term *SIS detector* implies that the AC Josephson current is not present [21].

Thus, of most importance to SIS mixers, is the quasiparticle current which accounts for the highly non-linear I-V curve characteristic. In order for the single electrons to tunnel, they must be excited with enough energy to overcome the energy gap. This may be accomplished by simply applying a DC voltage to the junction such that $eV_{DC} > \Delta_1 + \Delta_2$. Fig. 22 shows this effect for an ideal junction and also illustrates the hysteresis due to the supercurrent. Realistically, the non-linear part of the I-V curve is smeared out over a finite voltage and there is some offset leakage current (as shown for the solid line of Fig. 23b). Above the gap voltage, the I-V curve becomes linear with a slope of R_N^{-1}, where R_N is the *normal state resistance.*

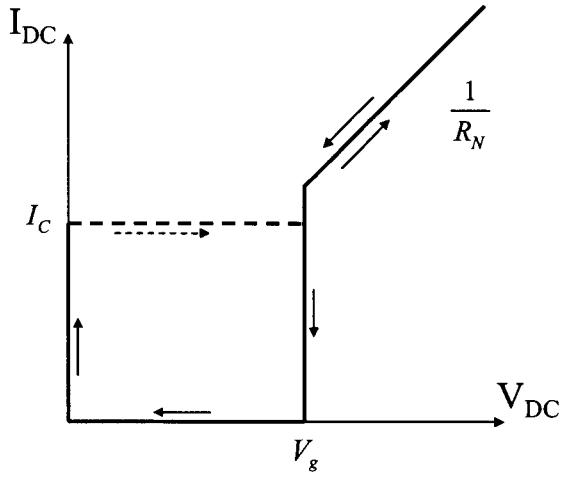

Fig. 22. Hysteresis of an I-V curve for an ideal SIS junction. Starting from the origin, the electron pair supercurrent increases up to the limit of the critical current, at which point the junction switches to the gap voltage and single particle current flows. Once the current has surpassed I_c, reducing it will only give rise to quasiparticle current, and the junction will remain at the gap voltage until the current becomes zero, at which point the voltage will drop back to zero (for a real junction this is called the *drop back voltage* and is less than the gap voltage). It is assumed that the AC Josephson current is suppressed.

A unique distinction between a SIS mixer and a classical mixer is the quantum effect of *photon-assisted tunneling* [13], [17]. In a heterodyne receiver, a large signal local oscillator (LO) is combined with the desired small signal to be downconverted. Since the corresponding incident photons have an energy of hf, single particle tunneling may be

induced if the junction absorbs a photon with enough energy to overcome the energy gap. Fig. 23a shows the semiconductor picture of this action and illustrates that the relation

$$eV_{DC} + nhf > \Delta_1 + \Delta_2 \qquad (36)$$

must hold for tunneling to occur, where n is the number of quanta absorbed. If the frequency of the incident radiation is such that the photon voltage is greater than the voltage width of the nonlinear part of the I-V curve [21], current steps will appear as shown for the dotted line in Fig. 23b. For example, the first step below the gap voltage indicates DC voltage bias point for which one additional photon induces tunneling. The threshold voltage is $V_{gap} - hf/e$. Fig. 23b represents two measurement scenarios: the *pumped* and *unpumped* I-V curves corresponding to the dotted and solid line respectively.

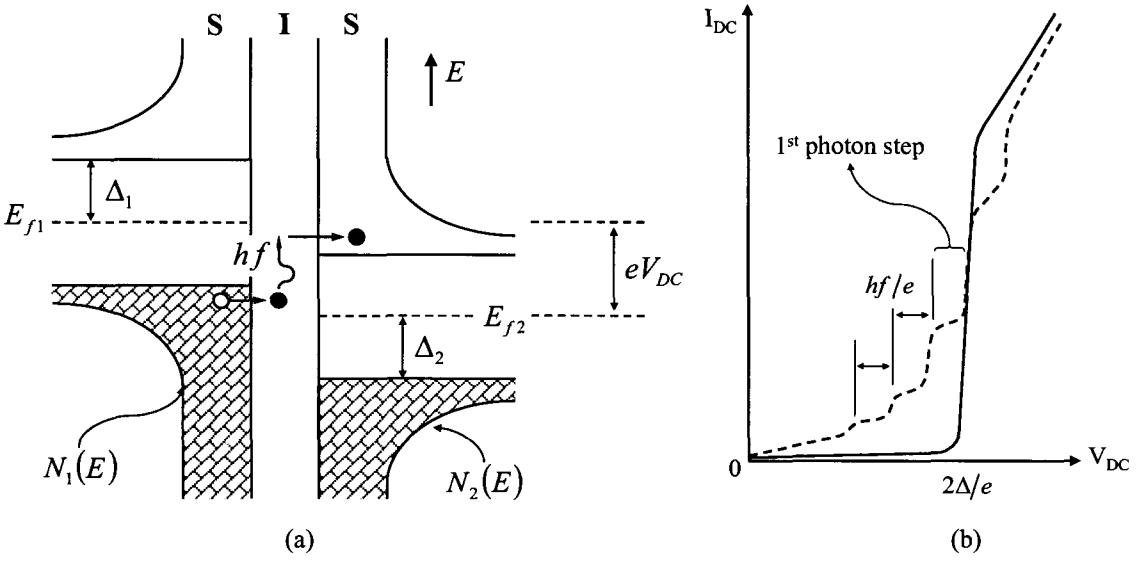

Fig. 23. (a) Semiconductor picture of photon-assisted tunneling of a SIS junction. The junction has been biased with eV_{DC} which is still less than the gap energy. An incident photon provides an additional hf of energy, enough to excite the quasiparticle over the gap and tunnel through the barrier. (b) The dotted line shows the pumped I-V curve of a SIS junction and illustrates the current steps due to photon-assisted tunneling. Single electron tunneling will occur without incident radiation (the unpumped I-V curve) when the bias is great enough to overcome the gap energy as shown by the solid line [21].

3.3 Quantum Mixer Theory – Frequency Domain

It was J. R. Tucker who provided a complete quantum mechanics treatment of mixer theory; first applying it to Schottky diodes, and then to SIS mixers with the adjoining effort of M. J. Feldman [19]-[22]. Surprising phenomena such as quantum-limited

sensitivity, photon-assisted tunneling, and the possibility of gain (negative IF conductance) have been described. What follows is a summary of this theory given in the frequency domain, which is the most prevalent application in use today. A time domain formulation of the theory has also been discussed and will be presented in the following section.

The quantum mixer theory follows a *Hamiltonian* approach based on [14]. For a classical system, the Hamiltonian of a system represents the energy of the system expressed in its coordinates and momentum. Once the Hamiltonian is given, the equations of motion can be determined and be used to predict what will happen to a particle from one time instant to the next. In quantum mechanics, however, it is not possible to know both the momentum and position with absolute precision – this is the *uncertainty principle* and implies that the exact path of a particle is no longer valid. However, within a localized and bounded space, the position and momentum can be measured to within an error specified by the uncertainty principle. Probabilities are then used to predict the motion of the particle.

Within quantum mechanics, the Hamiltonian formulation is used to solve for the *wave function*, $\Psi(q)$, where q represents the coordinates of the system. Once the wave function is known, the state of a system has been completely determined and the probability distribution of the particle is given by $|\Psi(q)|^2$. Solving for the wave function is non-trivial and requires the solution of the *wave equation* given by

$$i\hbar\frac{\partial\Psi}{\partial t} = H\Psi \tag{37}$$

where H is the Hamiltonian of the system, $i = \sqrt{-1}$ and $\hbar = h/2\pi$ [23].

To describe the SIS junction, the total Hamiltonian is

$$H = H_R^0 + H_L^0 + eV(t)N_L + H_T \tag{38}$$

where H_L^0 and H_R^0 describe the left and right side electrodes of the junction (assuming no tunneling), H_T characterizes the coupling between the two sides (called the *transfer Hamiltonian*), and $eV(t)N_L$ represents the modulation of the junction that occurs when a

time-varying voltage potential is applied across it (where N_L is called the *left-side number operator* and $V(t)$ is the potential). Using the last two terms of (38), and assuming adiabatic modulation (meaning that the excitation of the potential across the junction is slow enough such that the junction remains in thermal equilibrium), a time-dependent perturbation theory is used to solve for the quasiparticle tunneling current. The expected current is

$$\langle I(t)\rangle = \mathrm{Im}\int_{-\infty}^{\infty} W(\omega')W^*(\omega'')e^{-i(\omega'-\omega'')t}\, j(V_{DC}+\hbar\omega'/e)d\omega' d\omega'' \qquad (39)$$

and has been written in the frequency domain in the form of [18]. This complex expression can be understood in two parts. First, because of the time-dependence of the applied voltage, an extra term will arise that multiplies this time-dependence onto the wave function. This is called the *phase factor* and is written as

$$U(t) = e^{-i\frac{e}{\hbar}\int_0^t V(t')dt'}. \qquad (40)$$

The significance of the phase factor will be explored more fully in the next section. To obtain the expression of (39), the phase factor is Fourier transformed so that

$$e^{-i\frac{e}{\hbar}\int_0^t [V(t')-V_{DC}]dt'} = \int_{-\infty}^{\infty} W(\omega')e^{-i\omega t}\, d\omega' \qquad (41)$$

where the right side expression represents only the AC part of the phase factor. That is, since the voltage can be written as $V(t)=V_{AC}(t)+V_{DC}$, equation (41) shows the DC part removed from the expression. There are two integration factors in (39) to account for tunneling currents in both directions through the junction.

A complex *response function*, $j(V)$, is contained in the second part of (39) and it characterizes the quantum features of the junction. When the applied voltage is DC, the expected current reduces to

$$\mathrm{Im}\, j(V_{DC}) = I_{DC}(V_{DC}). \qquad (42)$$

There is great significance in this finding because $I_{DC}(V_{DC})$ is the unpumped I-V curve of the junction and may be measured. Now to solve for the current with a time-dependent voltage, the entire complex function $j(V)$ must be known, yet only the imaginary part can be determined through measurement. Fortunately, the real part of the response function can be found through the *Kramers-Kronig transform*, given as

$$I_{KK}(V) = P\int_{-\infty}^{\infty} \frac{[I_{DC}(V') - V'/R_N]}{V' - V}\frac{dV'}{\pi} = \mathrm{Re}\, j(V) \tag{43}$$

where P is the *Cauchy principle value* and $I_{DC}(V)$ is the function describing the measured I-V curve. Note that by subtracting the Ohmic region from within the integrand, the limits of integration are reduced (C.F. Sec. 3.4.1). To restate the implications of (43), a simple DC measurement of the I-V curve contains sufficient information to predict the complete current response (including the RF response) when the voltage across the junction is known.

3.3.1 Large Signal Response

Following standard mixer theory, the waveform of the large signal (or local oscillator) applied to the junction must be determined. In general, the resulting voltage established across the junction is a function of the LO generator and its impedance. The generator impedance is frequency dispersive and combines the input waveguide and strip transmission lines to the junction along with the capacitance of the junction itself. As harmonics of the generator will be present, determining the voltage response across the junction is challenging. Established techniques to solve this problem are the *multiple reflection method* [53] and the *voltage update method* [54], [55]. These methods take advantage of the time domain expressions by treating the mixer response in the time domain and then interfacing it to the embedding network through a frequency conversion.

Assume, then, a simplified case where the waveform that develops across the mixer contains only a pure sinusoidal local oscillator and some DC bias. The voltage may be expressed as

$$V(t) = V_{DC} + V_{LO}\cos(\omega_{LO}t) \tag{44}$$

where the LO has a magnitude of V_{LO} and frequency ω_{LO}. It is more common to express the amplitude of the LO in terms of

$$\alpha = eV_{LO}/\hbar\omega_{LO} \tag{45}$$

where α is the *pumping factor*. The expression of (39) will then result in

$$I_{LO}(t) = a_0 + \sum_{m=1}^{\infty} (2a_m \cos m\omega_{LO}t + 2b_m \sin m\omega_{LO}t) \tag{46}$$

where

$$2a_m = \sum_{n=-\infty}^{\infty} J_n(\alpha)[J_{n+m}(\alpha) + J_{n-m}(\alpha)]\, I_{DC}(V_{DC} + n\hbar\omega/e)$$

$$2b_m = \sum_{n=-\infty}^{\infty} J_n(\alpha)[J_{n+m}(\alpha) - J_{n-m}(\alpha)]\, I_{KK}(V_{DC} + n\hbar\omega/e)$$

$$a_0 = \sum_{n=-\infty}^{\infty} J_n^2(\alpha)\, I_{DC}(V_{DC} + n\hbar\omega/e)$$

and m indicates the corresponding harmonic content of the current. Note that J_n are the n-th order *Bessel functions of the first kind*, and they arise from evaluation of the phase factor. For example, looking at only the AC part of the phase factor it can be written as

$$e^{-i\left[\frac{eV_{LO}}{\hbar}\int_0^t \cos\omega_{LO}t'\,dt'\right]} = e^{-i\frac{eV_{LO}}{\hbar\omega_{LO}}\sin\omega_{LO}t} = \sum_{n=-\infty}^{\infty} J_n\left(\frac{eV_{LO}}{\hbar\omega_{LO}}\right) e^{-in\omega_{LO}t} \tag{47}$$

through the Bessel-Fourier expansion.

While the expression of (46) is quite complicated, it is seen that part of the current depends on the I-V curve function, and the other on reactive terms from the Kramers-Kronig transform. These quantum reactances do not appear in classical mixer theory and imply that the current is no longer instantaneously related to the applied voltage. The current response at DC, or a_0, corresponds to the pumped I-V curve as in Fig. 23b.

3.3.2 Small Signal Response

Once the large signal response for the nonlinear network has been determined, the mixing properties of the small signal may be analyzed. Fig. 24 shows a diagram

representing a heterodyne receiver where each mixer product, $\omega_m = m\omega_{LO} + \omega_{IF}$, is assigned a separate port. Each port voltage is related linearly to the other currents by

$$i_m = \sum_{m'} Y_{mm'} v_{m'} \tag{48}$$

where $Y_{mm'}$ is the admittance matrix that characterizes the large signal solution with the nonlinear element, and i_m and v_m are phasors at frequency ω_m. Since port 1 is assumed to be the desired RF signal sideband, it is represented by an additional current generator with a specified admittance. All other sidebands are assumed not incident to the receiver and are only represented with an admittance at that frequency. Port 0 also has special meaning because this is the downconverted output IF signal (where $Y_0 = Y_L$ is the IF load admittance seen by the mixer). Note that $V_{LO}(t)$ represents the solution of the large signal, time-varying waveform impressed across the nonlinear device; here assumed to be the local oscillator waveform as specified by the AC part of (44).

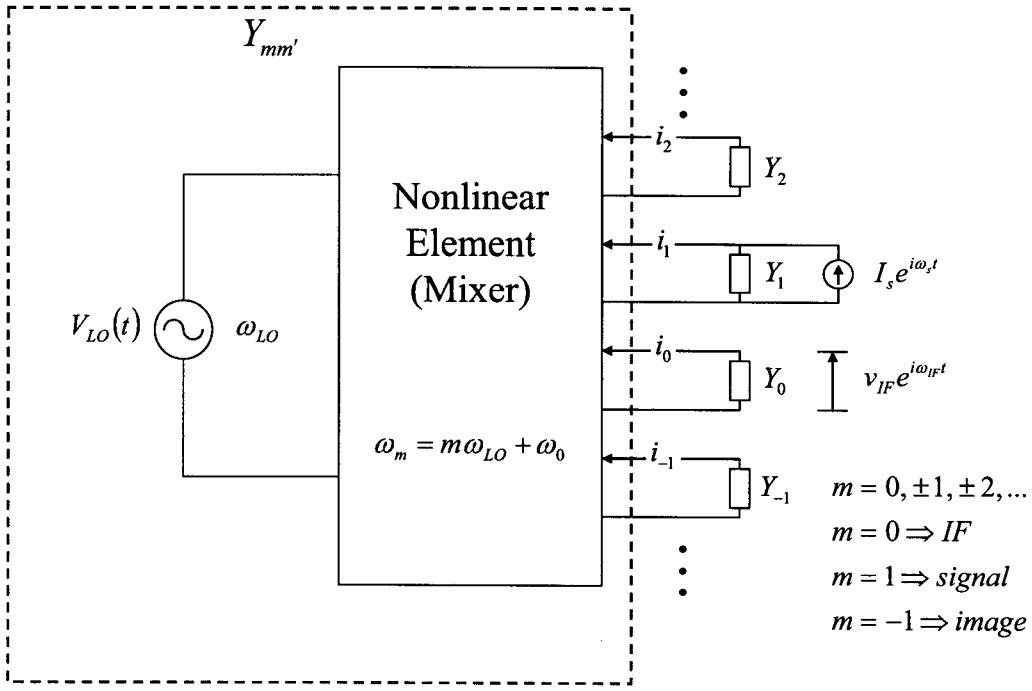

Fig. 24. Diagram illustrating a heterodyne receiver. Each sideband (denoted by m) is assigned a separate port such that it is related to other ports in a linear fashion through an admittance matrix, $Y_{mm'}$. The characteristics of the admittance matrix represent the nonlinearities of the mixer element as determined by the large signal (local oscillator) waveform applied across the diode.

Determining the admittance matrix requires changing the phase factor to include the small signal so that the voltage potential becomes

$$V(t) = V_{DC} + V_{LO}(t) + v_{sig}(t) \tag{49}$$

where $v_{sig}(t)$ contains the combined signal voltages at every sideband. Keeping only terms that are first order and linear, the admittance matrix is found to be

$$Y_{mm'} = G_{mm'} + iB_{mm'} \tag{50}$$

where

$$\begin{aligned} G_{mm'} &= \frac{e}{2\hbar\omega_{m'}} \sum_{n,n'=-\infty}^{\infty} J_n(\alpha) J_{n'}(\alpha) \delta_{m-m',n'-n} (A_G + B_G) \\ A_G &= I_{DC}(V_{DC} + n'\hbar\omega_{LO}/e + \hbar\omega_{m'}/e) - I_{DC}(V_{DC} + n'\hbar\omega_{LO}/e) \\ B_G &= I_{DC}(V_{DC} + n\hbar\omega_{LO}/e) - I_{DC}(V_{DC} + n\hbar\omega_{LO}/e - \hbar\omega_{m'}/e) \end{aligned} \tag{51}$$

and

$$\begin{aligned} B_{mm'} &= \frac{e}{2\hbar\omega_{m'}} \sum_{n,n'=-\infty}^{\infty} J_n(\alpha) J_{n'}(\alpha) \delta_{m-m',n'-n} (C_B - D_B) \\ C_B &= I_{KK}(V_{DC} + n'\hbar\omega_{LO}/e + \hbar\omega_{m'}/e) - I_{KK}(V_{DC} + n'\hbar\omega_{LO}/e). \\ D_B &= I_{KK}(V_{DC} + n\hbar\omega_{LO}/e) - I_{KK}(V_{DC} + n\hbar\omega_{LO}/e - \hbar\omega_{m'}/e) \end{aligned} \tag{52}$$

Recall from Fig. 24 that a current generator has been added to represent incoming signal radiation to the receiver. This can be generalized for any number of incident signals so that

$$\begin{aligned} I_m &= i_m + Y_m v_m \\ &= \sum_{m'} (Y_{mm'} + Y_m \delta_{m,m'}) v_{m'} . \end{aligned} \tag{53}$$

Now (53) can be inverted to solve for the signal voltages at each sideband so that

$$v_m = \sum_{m'} Z_{mm'} I_{m'} \tag{54}$$

where

$$\left\| Z_{mm'} \right\| = \left\| Y_{mm'} + Y_m \delta_{m,m'} \right\|^{-1} \tag{55}$$

such that the matrix includes the sideband admittances (equation given in matrix notation). Therefore, the conversion gain of a SSB signal (as in Fig. 24) is found to be

$$G_{mixer} = \frac{P_{out}}{P_{in}} = \frac{0.5G_L|Z_{01}|^2|I_s|^2}{|I_s|^2/8G_s} = 4G_S G_L|Z_{01}|^2 \tag{56}$$

where G_S and G_L are the real parts of the respective port admittances [21].

Along with the conversion gain, the other important parameter, to be determined by Tucker's theory, is the noise of the mixer. Continuing from [21], a *current correlation matrix* is used to describe the downconverted shot noise and is defined as

$$H_{mm'} = e\sum_{n,n'=-\infty}^{\infty} J_n(\alpha)J_{n'}(\alpha)\delta_{m-m',n'-n}(E+F)$$
$$E = \coth[\beta(eV_{DC} + n'\hbar\omega_{LO} + \hbar\omega_{m'})/2]\, I_{DC}(V_{DC} + n'\hbar\omega_{LO}/e + \hbar\omega_{m'}/e). \tag{57}$$
$$F = \coth[\beta(eV_{DC} + n\hbar\omega_{LO} - \hbar\omega_{m'})/2]\, I_{DC}(V_{DC} + n\hbar\omega_{LO}/e - \hbar\omega_{m'}/e)$$

The SSB mixer noise temperature is then

$$T_{mixer} = \frac{1}{4kG_S|\lambda_{01}|^2\sum_{m,m'}\lambda_{0m}\lambda^*_{0m'}H_{mm'}} \tag{58}$$

where $\lambda_{0m} = Z_{0m}/Z_{00}$. Recall that Fig. 1 illustrated the noise level would never drop below a contribution due to the zero-point fluctuations. However, (58) does not indicate any lower limit and may even approach zero [21]. This apparent contradiction is resolved when the input signal and image terminations are taken into account. For example, in a DSB mixer, both sidebands emit a noise power according to the Callen and Welton expression of (3). Even if these terminations were at 0 K, they would each still contribute a noise temperature of $hf/2k$ so that the minimum *system* mixer noise is hf/k. A detailed explanation with further examples is given in [31] and [32]. Therefore, depending on how the cascaded receiver performance is being calculated (e.g., as in Sec. 2), the value of T_{mixer} may need to be modified. That is, when the Callen and Welton expressions for noise are used in the cascaded analysis, the zero point fluctuations are already accounted for. It is common, however, to use Planck's equations during a cascaded analysis when the frequency and temperature allow (an approximation used in

this thesis), and so the value of (58) needs an additional $hf/2k$ for each sideband (sidebands that are shorted out do not contribute) [43]. Regardless of the approach, the minimum theoretical system mixer noise is always hf/k (at 0 K with the mixer perfectly optimized). DSB receiver designs have come to within 3-4 times this amount, as demonstrated in this thesis and also in [44]-[47].

In order to simplify the above results for use with a computer program, a three-port approximation is used so that $m = 0, \pm 1$ and only the signal, image and IF bands are considered. All other bands are assumed to be shorted out by the junction capacitance. This assumption, combined with the earlier assumption that LO harmonics are also shunted, produces reasonable accuracy but underestimates the noise. In [56] a comparison between a three-port, quasi five-port, and full five-port approximation is given. The five-port approximations include the IF and first and second harmonics of the sidebands so that $m = 0, \pm 1, \pm 2$. In the three-port and quasi five-port, only the fundamental LO is considered in the large signal analysis; the full five-port includes the second LO harmonic. The quasi five-frequency approximation can be used with reasonable confidence for gain, bandwidth and impedance matching, but the noise is over estimated. An example is given in [45] where a quasi five-frequency approximation is used and an extra noise term due to the *multiple Andreev reflections* is included [57], which is in addition to the zero-point quantum noise discussed above.

3.4 Quantum Mixer Theory – Time Domain Analysis

The time domain formulation of the quantum mixer theory has also been presented in [19]-[21]. Earlier work, [26]-[30], concentrated on the time response of Josephson junctions developed mainly for transient applications like switching and computing. Time-domain theory has already been used for certain aspects of simulation, e.g., determining the LO voltage waveform using the *multiple reflection method* [53] or the *voltage update method* [54], [55]. However, a full embedding of the mixer theory into a time domain 3D electromagnetic field solver has not yet been done. While the current and voltage waveforms can be modeled in the time-domain, it is not feasible to predict the noise, and so this would need to be treated separately.

The main advantages of performing simulations within the time domain are the ability to process arbitrary time signals applied to the nonlinear junction and to generate complete information on the mixing products over a wide frequency range. For example, assumptions on the harmonic content of the LO need not be made. A trade-off, however, is that more computational time is required when simulating in the time domain. Yet, this approach still seems feasible because the speed of computers has increased dramatically.

The following summarizes the time domain theory presented in [19]-[21]. To provide further insight, a MATLAB [60] implementation is used to demonstrate junction currents and photon-assisted tunneling. Note that the results do not include the effects of the junction capacitance or source impedance, but this can be implemented and is discussed later.

3.4.1 Time Domain Theory

Recall that the unique result of Tucker's theory is that the unpumped curve provides sufficient information to predict the RF performance of the mixer. This concept is shown through a response function, which is denoted in the frequency domain as $j(V)$ and is a complex function that characterizes the quantum features of the junction. Combined with the Kramers-Kronig transform, the response function is completely determined from the measured, unpumped I-V curve. Fig. 25a shows a measured I-V curve for a typical mixer used in the receiver measurements given above. These mixers each contain four junctions arranged in a series array. For simplicity, the I-V curve characteristic used in this section to demonstrate the time domain theory is shown in Fig. 25b and represents data that might be measured for a single Nb junction [43].

In the time domain, the response function is defined in the following manner:

$$\overline{\chi}(t)=\frac{2}{\pi}\int_0^{\infty}\left(I_{DC}(\hbar\omega/e)-\frac{\hbar\omega}{eR_n}\right)\sin\omega t\,d\omega. \qquad (59)$$

The function, $I_{DC}(V)$, is the equation that describes the measured unpumped I-V curve and is assumed to be an odd function that tends toward the normal state conductance at large bias voltages. The integration factor, ω, should not be confused with the frequency

of an applied voltage signal, but is only present as a consequence of the inverse Fourier transform. Since $I_{DC}(V)$ is a function of voltage, it is evaluated at the corresponding photon voltages for the integration factor ω. Like before, all of the quantum aspects of a particular SIS junction are embodied in the response function. It is based entirely on the I-V curve and is independent of any applied voltage. The response function only needs to be calculated once and, noting the bracketed expression of (59), computation is seen to converge when $I_{DC}(V) \rightarrow V/R$.

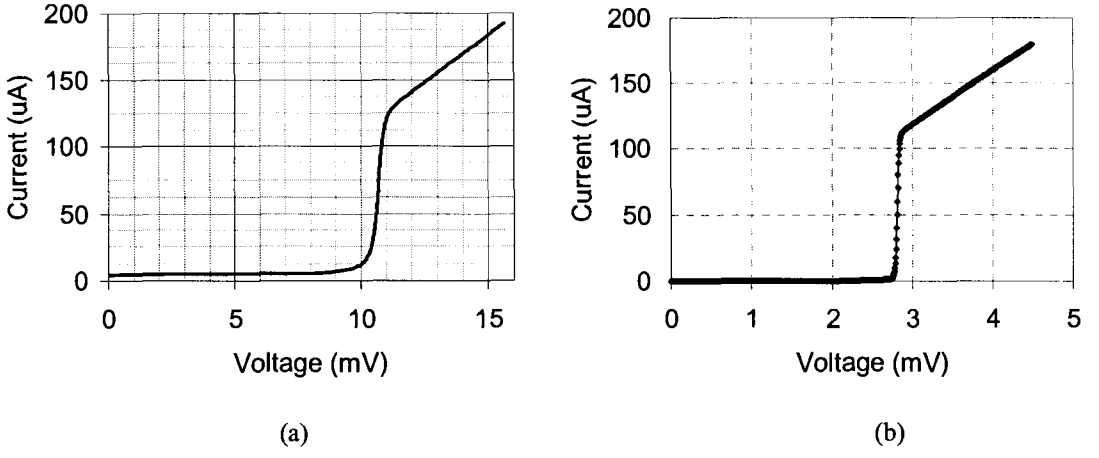

Fig. 25. Unpumped I-V curves that may be used for analysis. (a) Measured I-V curve for a series array of four Nb junctions. This is the typical response of the mixers used within the Band 3 receivers. (b) I-V curve characteristic mimicking a measured response for a single Nb junction [43]. All MATLAB results contained herein are based on this manufactured curve.

Fig. 26 depicts the initial time segment of the response function that was calculated for the I-V curve data of Fig. 25b. The response function will oscillate at a frequency proportional to the *gap energy*, 2Δ, so that for the junction under consideration, the period of oscillation is given as

$$T_{gap} = h/2\Delta \approx 1.47 p\,\text{sec} \tag{60}$$

where

$$2\Delta = V_g \cdot e \tag{61}$$

and e is the electron charge and V_g is the gap voltage. The plotted response is only for a single junction; a series array of junctions will have a proportionally larger gap voltage and so the resonating frequency will increase. Furthermore, depending on the quality of

the junction, i.e., the sharper the nonlinearity of the I-V curve, the longer it will take for the response function to decay [27].

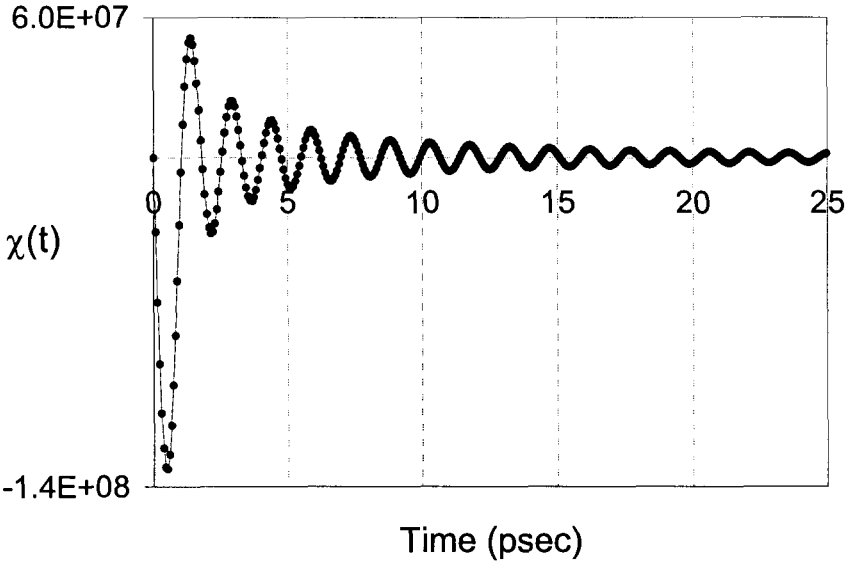

Fig. 26. The response function, $\chi(t)$, derived from the I-V curve data shown in Fig. 25b. The response function completely characterizes the nonlinearities and quantum effects of the SIS junction in the time domain.

It is appropriate to now consider the full time domain expression for the current across the junction for a given applied voltage, *V(t)*. One may compare this expression with the frequency domain form found in (39). The expected quasiparticle tunneling current is given as

$$\langle I(t)\rangle = \frac{V(t)}{R_n} + \mathrm{Im}\left(U^*(t) \int_{-\infty}^{t} \overline{\chi}(t-t')U(t')dt' \right). \tag{62}$$

where $U(t)$ is the phase factor. Recall that the phase factor arises from a derivation that is rooted in quantum mechanics and can be considered an extra term that multiplies the wave function describing the electron states. It will change depending on the voltage potential that is presented to the junction and is given as

$$U(t) = e^{-i\phi(t)} \tag{63}$$

where

$$\phi(t) = \frac{e}{\hbar} \int_{-\infty}^{t} V(t')dt' . \qquad (64)$$

It is important to recognize that the phase factor will always have a unity magnitude with the phase varying in the complex plane with increasing time.

As pointed out in [27], the expected current of (62) shows an instantaneous response (the first term) and a delayed component due to the convolution. In this way, the current depends on the past history of the applied voltage. This manifests itself in the frequency domain in the form of a reactive part of the current due to a quantum susceptance [21].

There are some computational simplifications that must be made to the above theory. Since $V(t)$ is assumed to be zero for $t < 0$, the corresponding $U(t)$ at these times will be real with a magnitude of one. Since the response function is also real, the latter term of (62) will always be zero for negative time values, and so the lower integration limit of (62) and (64) need only go to zero. Also, it is not necessary to store the entire voltage history when computing the convolution. Only the latest time values, equal in length to the time required for the response function to reach a steady state, are needed.

3.4.2 Large Signal Response

Even though the time domain implementation can accept an arbitrary applied voltage, in order to provide continuity with the frequency domain approach, consider the voltage signal defined as

$$V(t) = V_{DC} + V_{LO}\cos(\omega_{LO}t). \qquad (65)$$

The waveform of (65) shows a DC bias voltage component combined with a local oscillator voltage signal with magnitude V_{LO}. It is assumed that $V(t)$ is the voltage that falls across the mixer and, therefore, no LO source impedance has been taken into account.

Consider the unpumped case ($\alpha = 0$) such that only a DC bias is present across the junction. Fig. 27 depicts the current response when the junction is biased above, below and exactly at the gap voltage. One can clearly see the transient nature of the quasiparticle current.

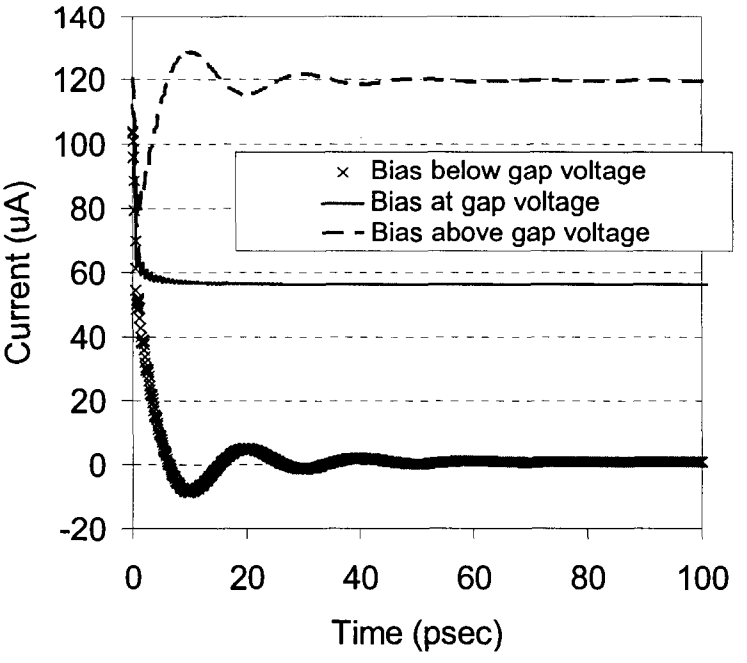

Fig. 27. Time responses of the current through the SIS junction due to three different DC bias voltages across an unpumped junction.

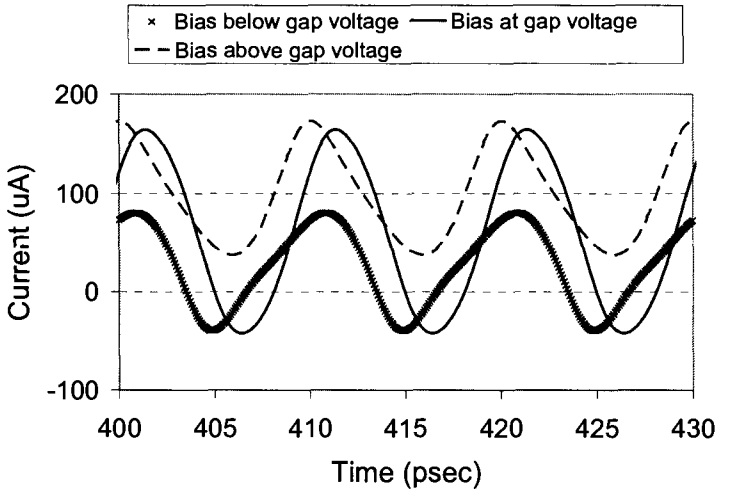

Fig. 28. Time response of current due to three different DC bias voltages across a pumped junction.

The junction is then pumped with the LO signal, at an amplitude corresponding to α = 1, and the current is evaluated using the same three bias voltages. Note that the DC biases correspond to V_g + ½ *LO photon voltage*, V_g, and V_g – ½ *LO photon voltage*, where hf/e is the photon voltage for a given frequency. Fig. 28 shows that the steady-

state waveform biased at V_g exhibits almost no distortion, while the other two signals contain harmonics of the local oscillator.

An interesting verification of the algorithm is to demonstrate the quantum effect of photon-assisted tunneling, as shown most clearly in the pumped I-V curve. The time-varying current was calculated at incremental DC bias voltages, from which the DC component of the current was then extracted through a Fourier transform. Fig. 29 shows the pumped curves that were computed for different pumping strengths; each step has an approximate width of 0.4 mV, which correctly corresponds to the photon voltage of the local oscillator (f_{LO} = 100 GHz).

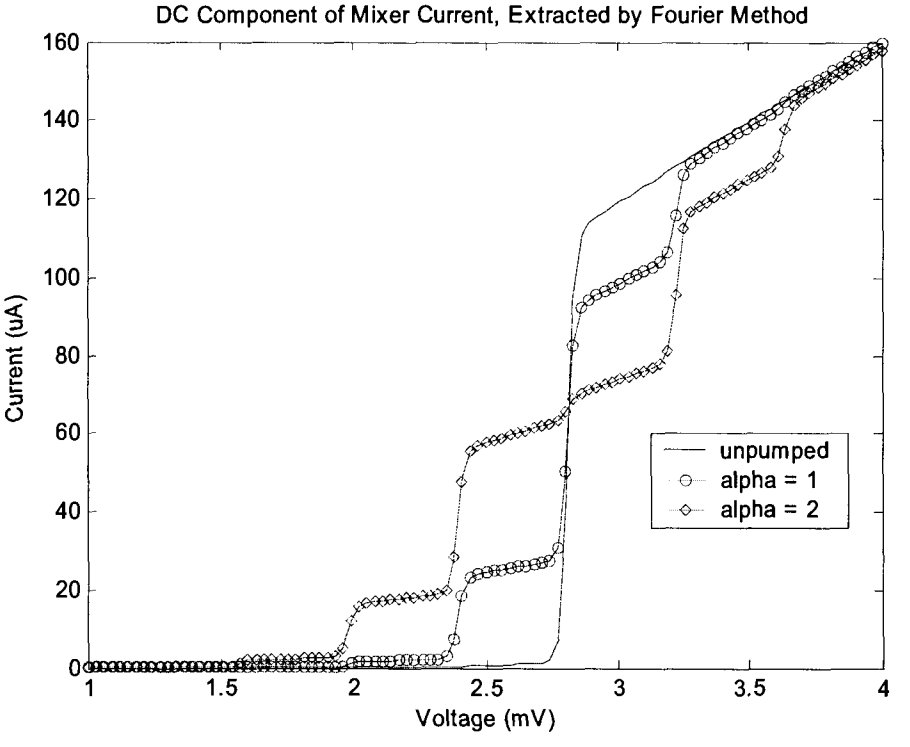

Fig. 29. Photon-assisted tunneling demonstrated with pumped I-V curves. Each curve was generated by extracting the DC component from the time domain response. A SIS mixer is typically biased near the midpoint of the photon step below the gap voltage.

Since, in practice, the junction is most often biased near the midpoint of the first photon step below the gap voltage, it serves well to look at the transient current for this condition. Fig. 30a shows the initial transient behavior and how, after several local oscillator periods, the signal has reached a steady state. The next figure shows a steady

state sample of this same waveform separated into the individual components of (62): the instantaneous current and the current arising from the convolution term.

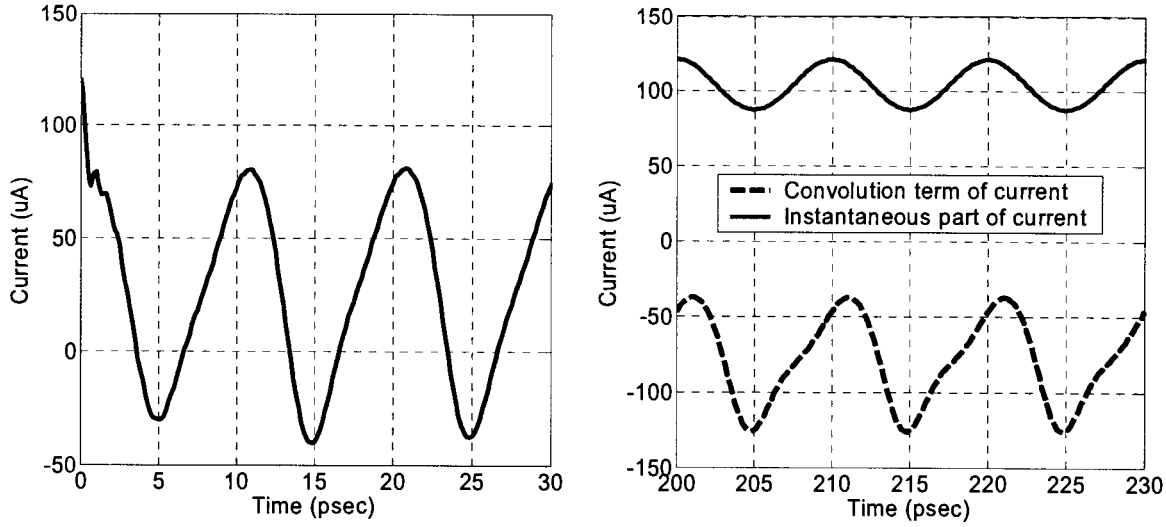

Fig. 30. (a) Transient response of the junction current when the DC bias voltage is centered on the first photon step and the LO is pumped at $\alpha = 1$. (b) Comparison of the two contributions of current once it has reached a steady state.

4 Modeling the Performance of SIS Mixers

When considering the quantum theory presented above, it is easy to lose sight of how and where the junction fits into the modeling scheme of the entire mixer. As one can guess, the entire process usually involves several modeling tools, each performing a task at a certain level of modeling depth as shown in Fig. 31.

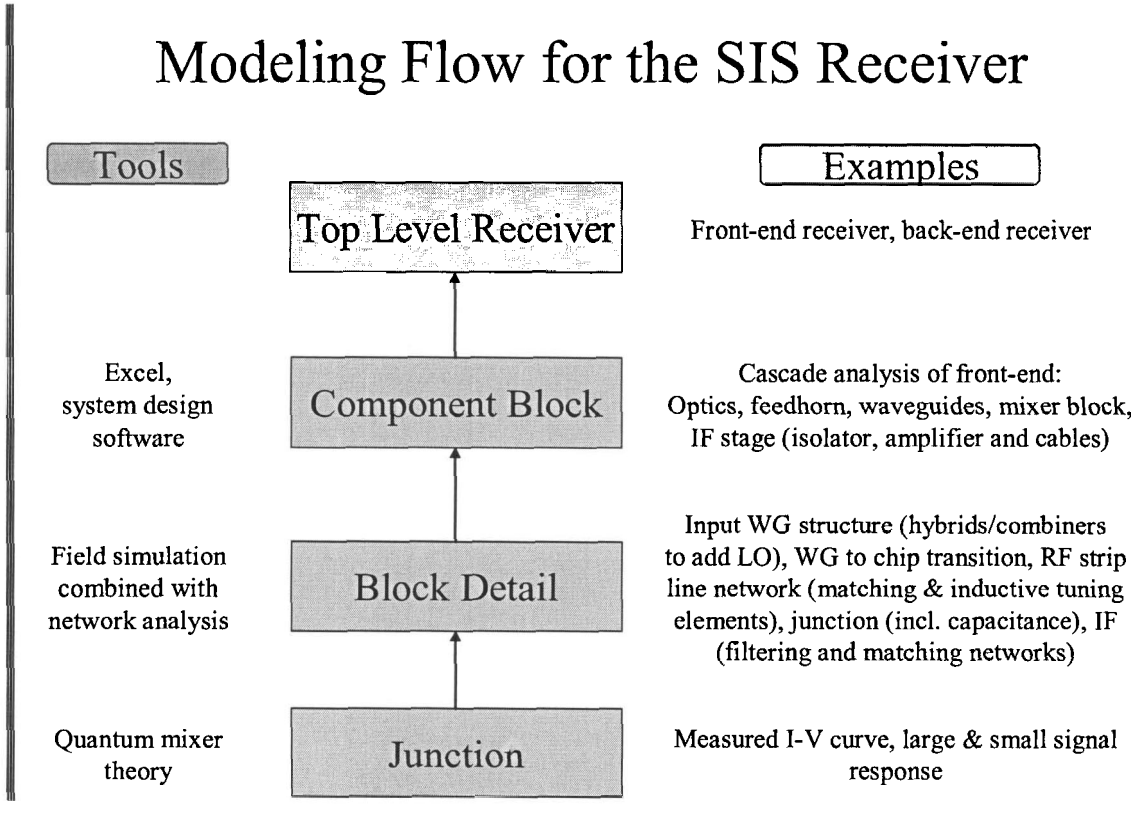

Fig. 31. Block diagram illustrating the different levels of modeling the SIS receiver. Each level typically requires the use of a separate analysis tool.

This thesis has already presented the component block level and the theory of the junction. The next step is the arduous task of modeling the mixer chip at the block detail level. Because of the limited scope of this thesis, only an overview of the standard frequency domain approach will be given. Following this, a summary of the chip design used for the Band 3 receivers is presented. The waveguide to mixer chip coupling is presented as an example of one stage within the block detail model. Following this section, an alternative approach (albeit simplified) is presented in the time domain as a first step to integrating Tucker's mixer theory into a full wave 3D field solver.

4.1 Standard Approach to Modeling the Mixer at the Block Detail Level

In order to model or design a mixer chip, it is necessary to interface the junction theory with the embedding environment. It is standard to work in the frequency domain so that impedance concepts are used throughout. The basic design and modeling approach are as follows:

1. Obtain measured junction characteristics which include the I-V curve, junction capacitance and normal state resistance.
2. Perform a quantum mixer theory analysis. During the design stage, the source and load impedances can be optimized for desired characteristics. Trade-offs must be made between input reflection, output reflection, gain/loss, bandwidth and noise temperature.
3. Each critical segment of the mixer block is characterized as a separate two-port network. Examples are: the waveguide to chip transition, biasing networks, RF and IF matching networks and inductive tuning elements. A combination of field solvers (to simulate complex segments) and network analysis software (to combine each two-port segment) is used. During the design stage, matching networks are used to present the mixer with the optimum values found in step 2.

It is assumed in Step 1 that the junction parameters have already been specified. Junction fabrication and characterizing the quality of the chip (through such factors as the critical current density, J_c, and the $\omega R_n C_J$ product) are outside of the scope of this thesis; however, design rules for chip parameters are given in [35], [36], [37]. The junction capacitance may be calculated using

$$C_J = \frac{\varepsilon_0 \varepsilon_r A}{t} \tag{66}$$

where t is the thickness of the oxide barrier and A is the surface area.

Step 2 requires a determination of the RF and IF source and load impedances. Note that in this context, the *source* refers to the LO generator source and assumes that the impedance does not vary greatly between the sidebands and LO frequency. When simulating an existing design, it is often difficult to ascertain the value of the source

impedance – especially at very high frequencies. If appropriate modeling tools are available, the source impedance can be found through simulation [39], as suggested in Fig. 31. Otherwise, a large scale model can be manufactured so that the embedding impedance can be measured using a network analyzer [34] (a more recent example is found in [38]). If the source and load impedances have not yet been designed, the quantum theory algorithm may be used to find optimized values depending on the design requirements.

Recall that the large signal response determines the correct pumped voltage falling across the junction; each time the source impedance changes, the large signal response must be re-calculated. Fig. 32 shows the admittance matching circuit for the RF section where $Y_{S,opt}$ is the optimum source admittance that includes the junction capacitance, inductive tuning elements, and all previous circuitry (e.g., waveguides, antenna, etc.).

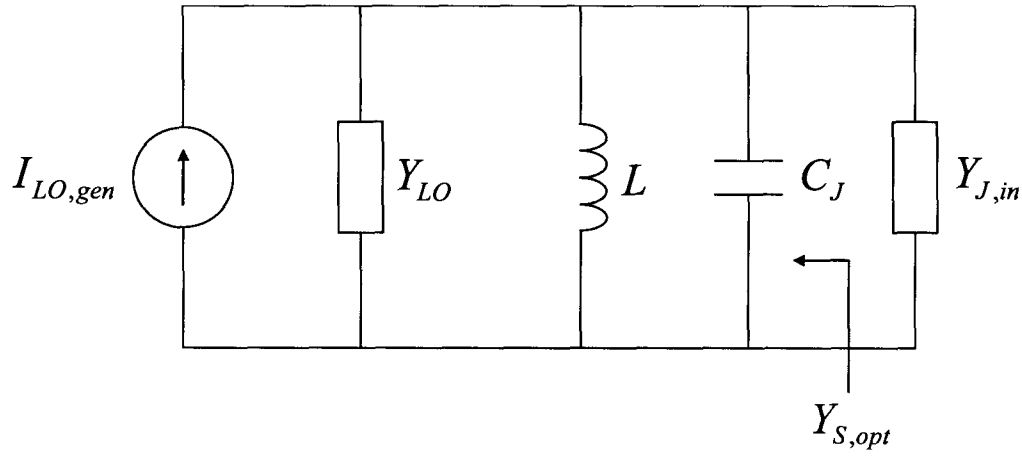

Fig. 32. Circuit description for RF impedance match of SIS junction. The optimum noise impedance match does not correspond to a maximum power transfer condition. For clarity, the junction capacitance and inductive tuning network (to tune out this capacitance over the frequency of the LO and sidebands) have been separated out.

The purpose of the inductive element is to tune out the junction capacitance at the LO and sideband frequencies, but not at harmonic frequencies, so that they remain shorted out. Mechanical tuners, such as tunable waveguide backshorts, or fixed-tuned designs employing strip transmission lines, may be used. Since the matching and tuning networks must accommodate the DC biasing of the mixer, bandwidth is a concern. Usually, the strip transmission line network of the chip is fabricated with the same superconducting metal used in the junction which creates further complications because

the superconducting lines result in surface impedance changes, and special corrections within the simulation are necessary [58].

To understand the input RF admittance of the junction, it is common to represent the junction with a parallel RC combination, since the susceptance of the junction is dominated by the junction capacitance. As an approximation, one may use the junction capacitance, C_J, and the normal state resistance, R_n, so that $Y_{J,in}$ in Fig. 32 is simply $(R_n)^{-1}$. However, since this approximation does not take into account the quantum susceptances mentioned above, a better way to define it is

$$Y_{J,in} = \frac{I_{LO}}{V_{LO}} \tag{67}$$

where I_{LO} is the pumped LO current from (46) and V_{LO} is the large signal voltage established across the junction as in Fig. 24 [39]. Note that the optimum source admittance, for lowest noise, does not correspond to a matching condition with the junction. Depending on the mixer requirements for reflection, gain, noise and bandwidth, a suitable trade-off will need to be found. Design rules of thumb are given in [35], [36], [37] so that the chip exhibits approximately 0 dB conversion loss and 10 dB input return loss. Assuming that all the capacitance is tuned out, it was found that

$$R_{S,opt} = \left(\frac{R_N}{2.4}\right)\left(\frac{f_{GHz}}{100}\right)^{0.72} \tag{68}$$

where f_{GHz} is the LO frequency specified in GHz and $R_{S,opt}$ is the optimum source resistance. The same value of $R_{S,opt}$ was also used for the IF loading condition, i.e., R_L.

In general, to calculate the IF output admittance of the mixer, $(Z_{00})^{-1}$ needs to be found using (55). The load presented to the mixer is most often real, so it is represented as G_L which includes the IF matching, filtering and bias networks. In the special case of a DSB mixer, the RF signal sideband admittances are the conjugate of each other resulting in zero IF output susceptance of the junction. The output conductance can then be measured by taking the slope of the I-V curve around the bias operating point [21]. Depending on the source impedance, this slope can be negative implying that SIS mixers

may operate with gain (although instability becomes an issue). In [21] the detailed expressions to calculate the DSB gain are given and the reader is referred to equations (4.74)-(4.77).

As a final step, each segment of the mixer block is pieced together using a network analysis software. Complicated stages may be simulated using field solvers, an example of which is given in section 4.2.1.

4.2 Overview of ALMA Band 3 Mixer Chip Design

The ALMA Band 3 receiver uses a SIS mixing chip designed at the National Radio Astronomy Observatory (NRAO) that has been fabricated at the University of Virginia (UVA). A complete description of the design is given in [45], [46]. Further insight on the design is found in [40], and other experimental results are presented in [47].

To appreciate the geometry of the chip, consider the following diagram. Fig. 33 depicts the layout of the chip and a closer view of the matching circuitry preceeding the junction. It is fascinating to see how the actual junction comprises only a very small part of the chip. The chip lies inside a split block and is suspended between two channels as shown by view X-X. Along either side of the chip, a ground connection is made between the block and the co-planar waveguide ground layer using a crushed gold wire technique. RF energy from the waveguide is coupled onto the chip through an interaction between the waveguide backshort and the stripline probe position (section 4.2.1).

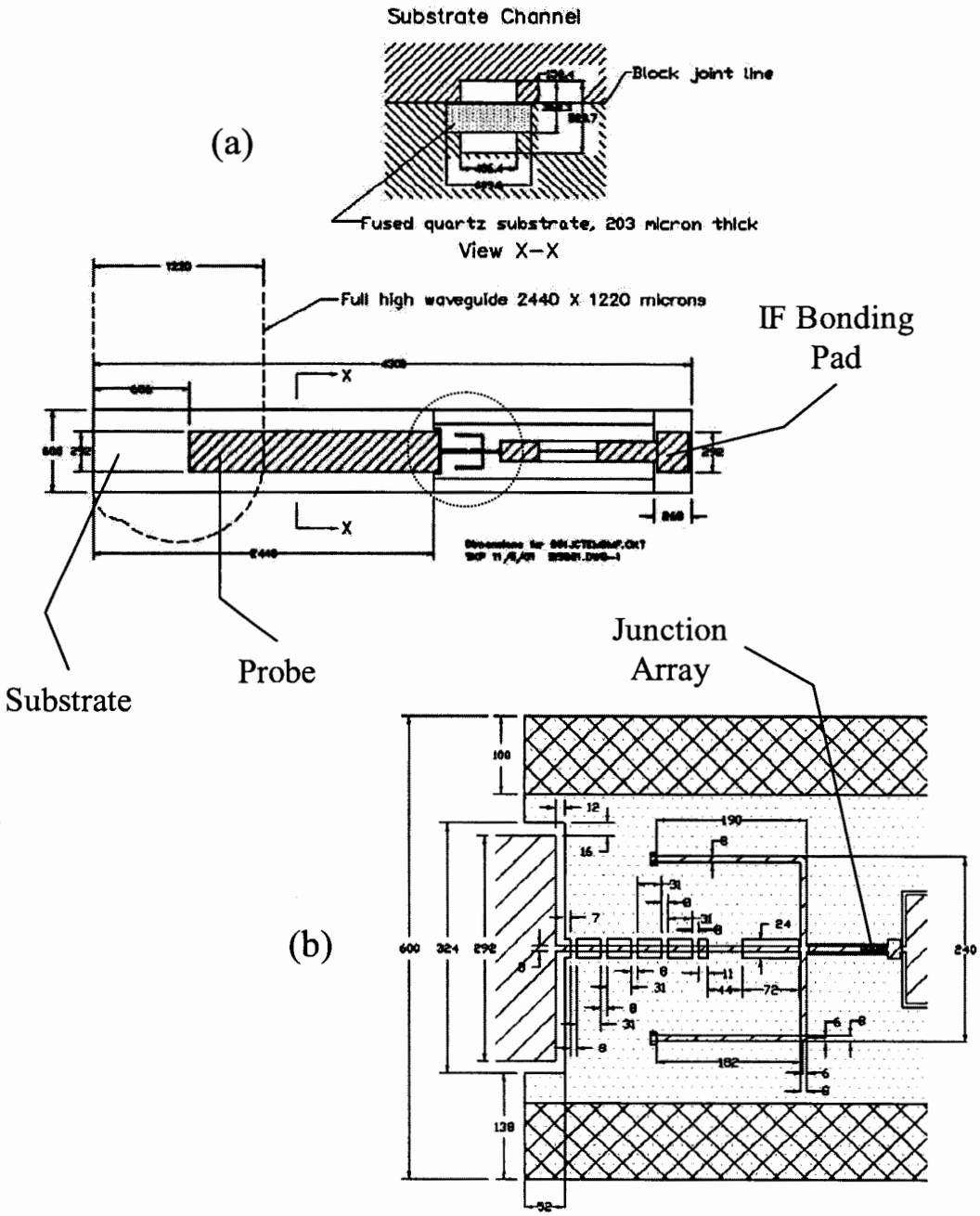

Fig. 33. Layout of the ALMA Band 3 mixer chip. Design is shown in [45]; these figures have been reproduced from this reference. (a) A top view of the entire chip substrate. The large strip on the left is the waveguide probe that allows coupling of the waveguide field onto the chip. The dashed line shows the position of the probe with respect to the input waveguide and backshort. View X-X above illustrates how the chip is suspended inside a split block. (b) Detailed view of the matching and tuning circuitry for the junction. The strip transmission line changes from suspended stripline to a co-planar waveguide network designed for matching and tuning so as to present the junction with the optimum source impedance. The DC bias termination is accomplished through the L-shaped microstrip short-circuited stubs; biasing is applied via the IF bonding pad.

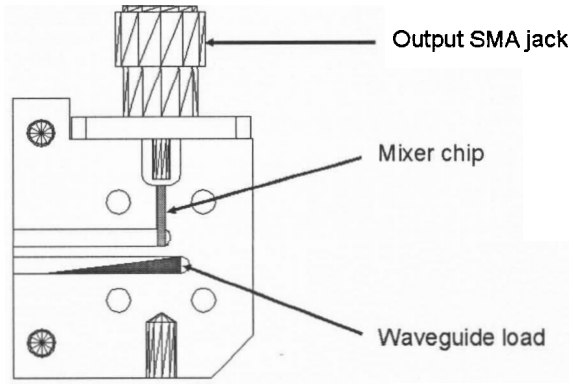

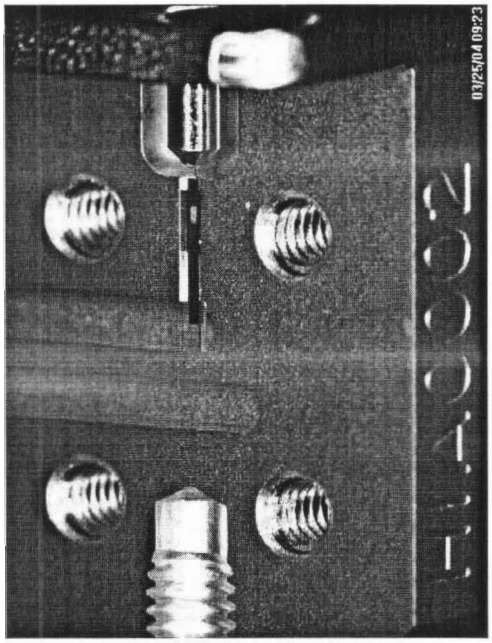

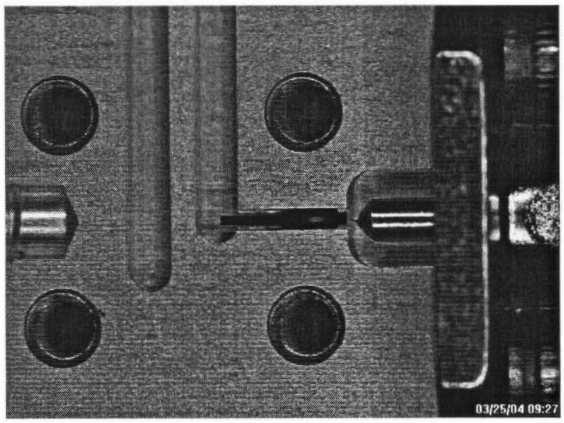

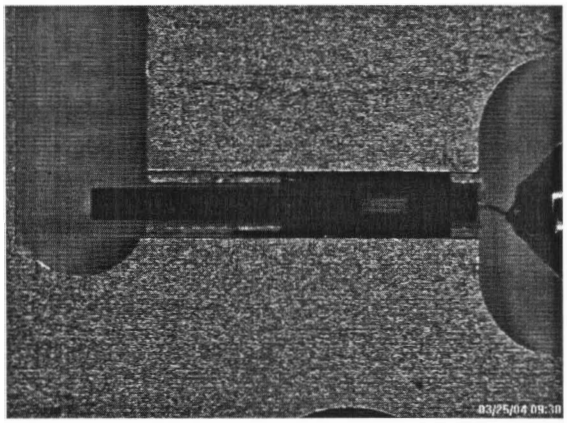

Fig. 34. Cross-sectional views of the ALMA Band 3 mixer block. The probe of the mixer chip intersects near the electric field maximum of the rectangular waveguide. The input waveguide is WR-9.6 (i.e., waveguide width is 0.096 inches) and only half of the E-plane split block is shown. Two waveguides are used because they interface to a waveguide hybrid where the lower guide is used to terminate one of the ports. A small bond wire runs between the chip and the center pin of a SMA connector. The chip is placed upside down and so the intricate junction matching network is masked by the ground plane.

The suspended stripline has a characteristic impedance of approximately 50 Ohms and then transitions into a capacitively loaded co-planar waveguide line, of similar impedance, to bring the line width on the scale of the junction geometry. A pair of microstrip short circuit stubs provide a DC bias ground and present a low impedance path for IF components. The advantage of this is that the IF is de-coupled from the input RF circuitry. Additional IF reactance due to the RF matching circuitry is then minimized,

thereby increasing the available IF bandwidth of the mixer. Next to the junction, a straight section of line acts inductively to compensate for the junction capacitance. Following the junction, a co-planar waveguide IF line chokes off high frequencies and matches the output IF impedance to 50 Ohms. The IF bonding pad provides a bonding surface for a wire that can be attached directly to the center pin of a 50 Ohm SMA connector. Fig. 34 shows the assembled mixer chip within the bottom half of the mixer block.

4.2.1 Simulation of Probe Coupling from Waveguide

As part of the integration process of the mixer chip into the ALMA Band 3 receivers, it was necessary to determine the effect that widening the slot of the mixer chip would have on the RF coupling performance. A model of the waveguide-antenna probe interaction was built using CST Microwave Studio [61], a time-domain 3D electromagnetic field solver. The modeling serves as a good example of one of the stages within the block detail level of Fig. 31.

Shown in Fig. 35, the model consists of an interaction between a WR-9.6 rectangular waveguide at port 1 with a suspended stripline transmission line at port 2. Note that a WR-9.6 is the same as a WR-10 waveguide except that the scaling is such that the width is 0.096" instead of 0.100". A slightly smaller dimension was used to increase the fundamental mode operating range to accommodate the frequencies of 84-116 GHz. Only the probe and suspended stripline section of the mixer chip were modeled; the input waveguide and output stripline were terminated with ideally matched ports. It is assumed in the model that the background material is a *perfect electrical conductor* (PEC).

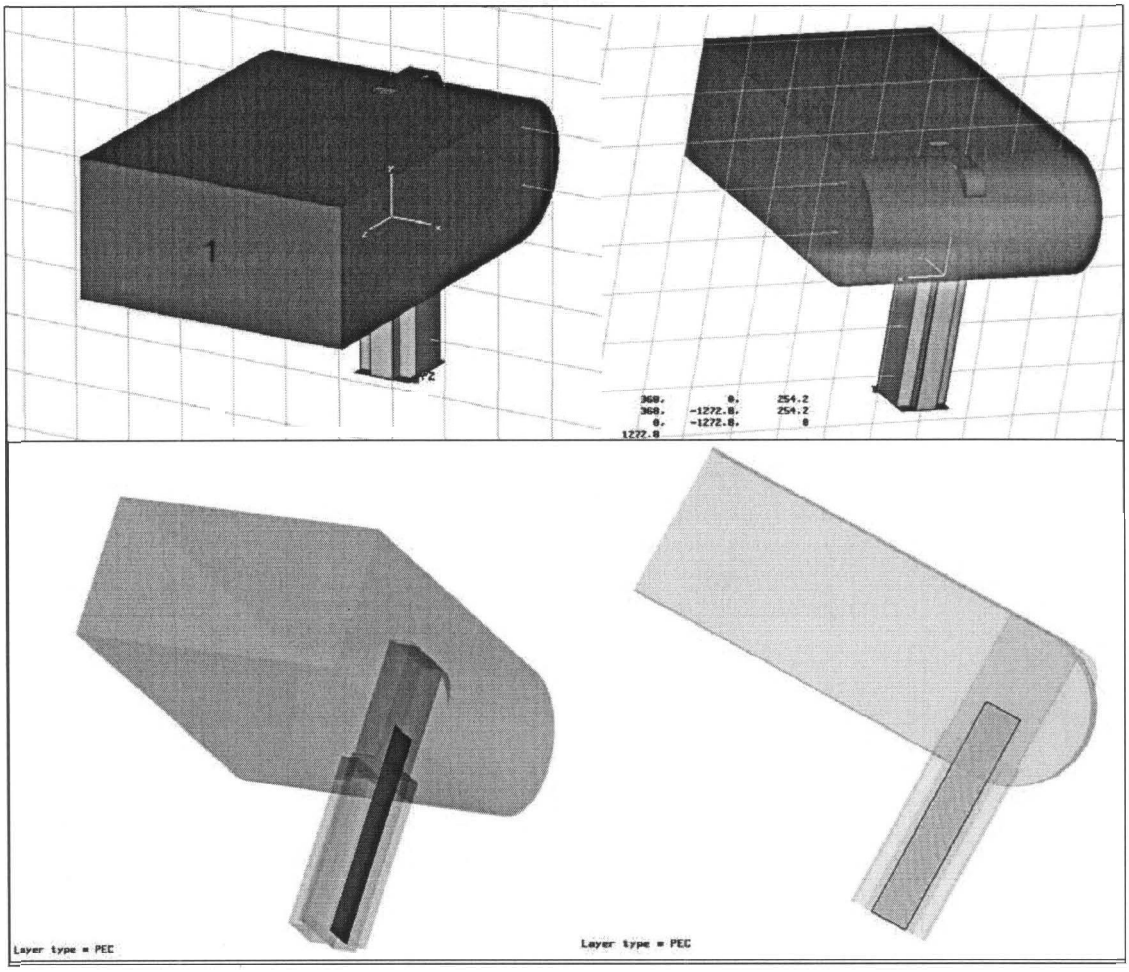

Fig. 35. Several views of the CST model showing the placement of the antenna probe within the waveguide. The quartz chip sits flush to the edge of the waveguide, but the strip probe extends only part of the way. The placement of the probe with respect to the rounded backshort (caused by the milling of the block) is critical to the coupling performance. It is assumed that the surrounding material is a perfect electrical conductor (PEC).

Recall that the block is machined in halves whereby the waveguide is split along the E-plane. The 3D model shows the complete, assembled form illustrating how the strip is aligned parallel to the electric field within the guide. The quartz substrate is placed into the slot so that the chip is flush to the side of the waveguide. The waveguide is terminated by a rounded backshort that is due to the milling tool used to machine the block. Notice how the probe extends only partly into the guide; it is the positioning of the stripline from the backshort that provides the optimal energy coupling.

A tolerance analysis was completed by varying the width of the mixer chip slot. S-parameters were used as the performance criteria for coupling and input impedance match. Since the slot gets wider and horizontal misalignment of the chip is more likely,

two simulation scenarios are necessary: (1) widening the slot with the chip remaining centered, and (2) widening the slot with the chip aligned to one edge (illustrated in Fig. 36).

To begin the analysis, the appropriate mesh density was determined so that a small change in slot width could be detected. The suspended stripline was analyzed by itself to observe the dependence of the line impedance with respect to this change. After this, the entire waveguide to stripline interface was analyzed and data was obtained for the range of $-10\mu m, +60\mu m$ variation of the slot width. Fig. 37 shows the results of the input impedance match when the slot width is varied. When the chip remained centered inside the slot, i.e., it did not change its position with respect to the back short, the input match did not degrade. However, small changes were observed when the chip was shifted towards or away from the backshort. It was determined that widening the slot by $20\mu m$ will cause, in the worst case, a 1 dB degradation in the input loss and negligible coupling loss.

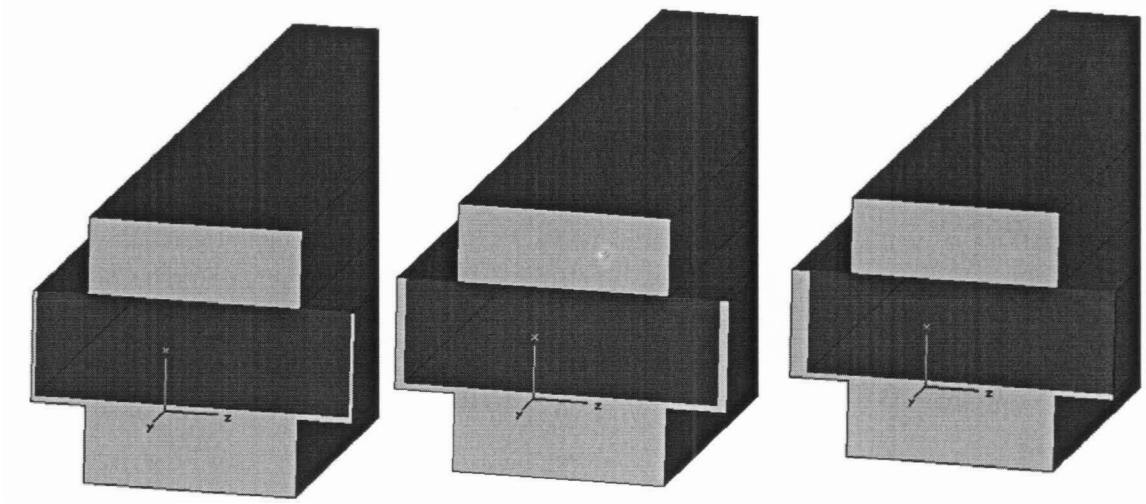

Fig. 36. Cross-sectional view of the suspended stripline part of the mixer chip. Only the dielectric of the chip (darker shading and centered) and the air of the grooves above and below the chip are shown. There is a slight gap between the bottom edges of the chip because a gold wire is placed along each shoulder of the slot. The chip is mounted with the strips facing downward so that as the chip is compressed into the wire, the crushed gold becomes the grounding contact between the chip and the block. Three positions are shown: (a) the nominal placement of the chip, centered in its slot, (b) the slot widened with the chip remaining centered, and (c) the slot widened with the chip off-centered and aligned to one edge.

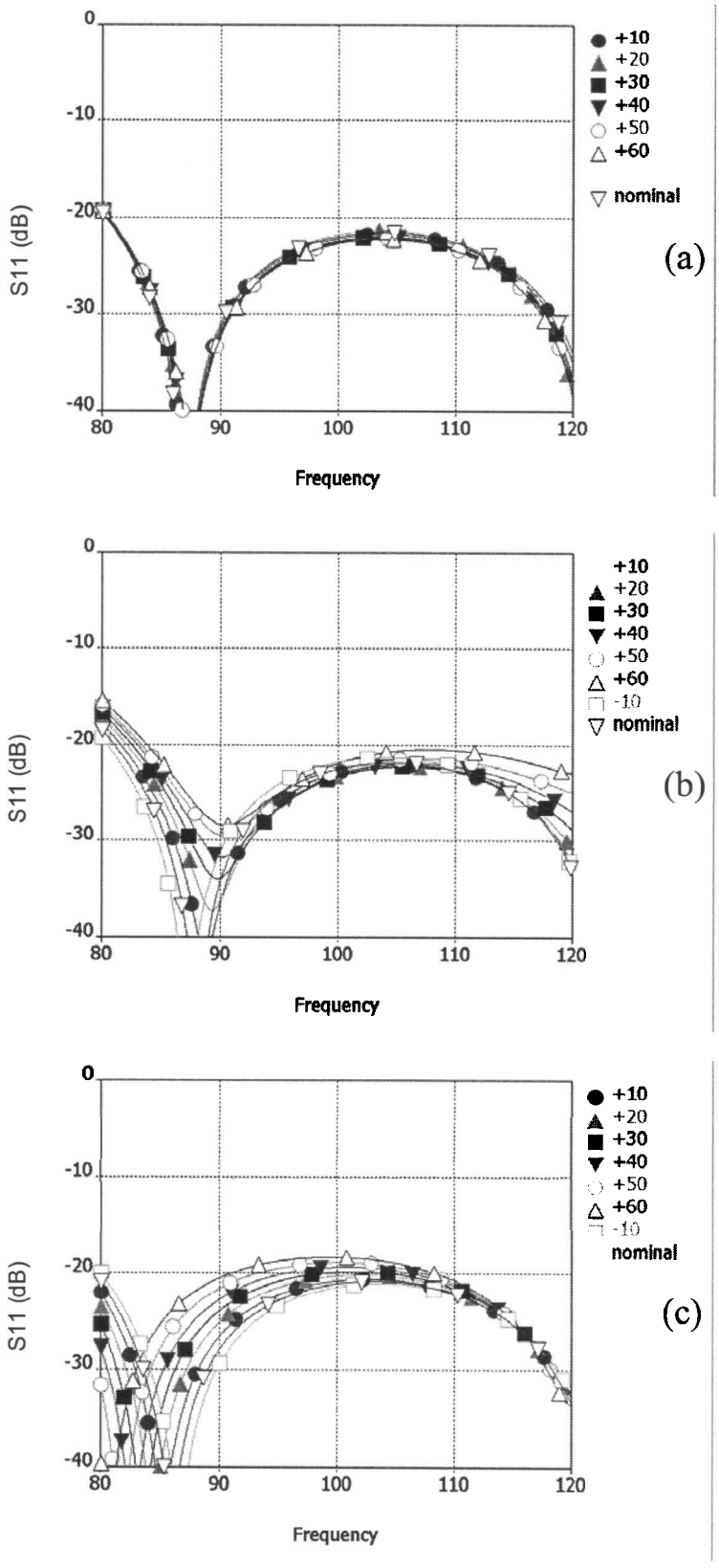

Fig. 37. Input match of waveguide-suspended stripline junction when slot width is varied.

5 Implementation of Time Domain Quantum Mixer Theory

The standard approach to determining the full quantum effects of the SIS mixer is to perform the computations in the frequency domain. To solve the large signal response, a time domain formulation has also been used in the *voltage update method* (VUM) [54], [55]. Even using this method, however, the nonlinear diode current (computed using the time domain equations) is related to the rest of the circuit in the Fourier domain. A short review of this technique is given and then a variation is presented (allowing full computation in the time domain), followed by a simple integration into a 3D field solver. Please note that a noise analysis is not considered feasible in the time domain and would need to be treated separately.

5.1 Voltage Update Method (VUM)

During the large signal analysis of the quantum mixer theory, approximations are made with respect to the LO and its harmonics. For example, when using a three-port approximation, all harmonics are considered to be shorted out and the LO is treated as a pure sine wave. The full five-port model takes into account the fundamental and the second harmonic, but assumes all others to be shorted out. As higher order harmonics are included, the resulting LO waveform across the mixer becomes increasingly complex. A further complication is due to the dispersive nature of the LO source impedance so that higher order harmonics see a different impedance than the fundamental.

Fig. 38 shows how the VUM addresses this problem by allowing the user to specify the embedding impedance, $Z_{source}(\omega)$, at each harmonic frequency. The generator voltage, V_{gen}, is represented by a DC bias and a pure sinusoidal source at the LO frequency. The dotted line divides the nonlinear and linear parts of the circuit.

The correct voltage falling across the junction is determined through an iterative process designed to match the terminal voltage of the linear network, $V^{LIN}(t)$, to the nonlinear part, $V^{NL}(t)$. The procedure starts with an initial guess on the voltage, $V^{NL}(t)$, falling across the junction and the corresponding diode current is found. The current due to the linear circuit, $I^{LIN}(t)$, must be equal and opposite to $I^{NL}(t)$. Using circuit theory, the linear network voltages at the interface are found by

$$V_n^{LIN} = Z_n^e I_n^{LIN} + V_{gen,n} \tag{69}$$

where $n = 0, 1, 2, ..., N$ denotes the index of the Fourier amplitude corresponding to the nth harmonic of the local oscillator, and $Z_n^e = \left(Z_{source,n} \| Z_{C,n}\right)$ is the equivalent source impedance that includes the junction capacitance. In other words, if the large signal voltage waveform is to be determined up to the fifth harmonic, equation (69) will be solved for all six cases: the DC, fundamental and four higher order harmonics. For example, using n = 0 (the DC case), the equivalent impedance is $Z_{source,DC}$ and the generator voltage is $V_{gen,DC}$. For n = 3 (the third harmonic), the equivalent impedance is the parallel combination of the source impedance with the junction capacitance, and the generator voltage is zero (in accordance with Fig. 38). The Fourier amplitudes of the current are found through transformation.

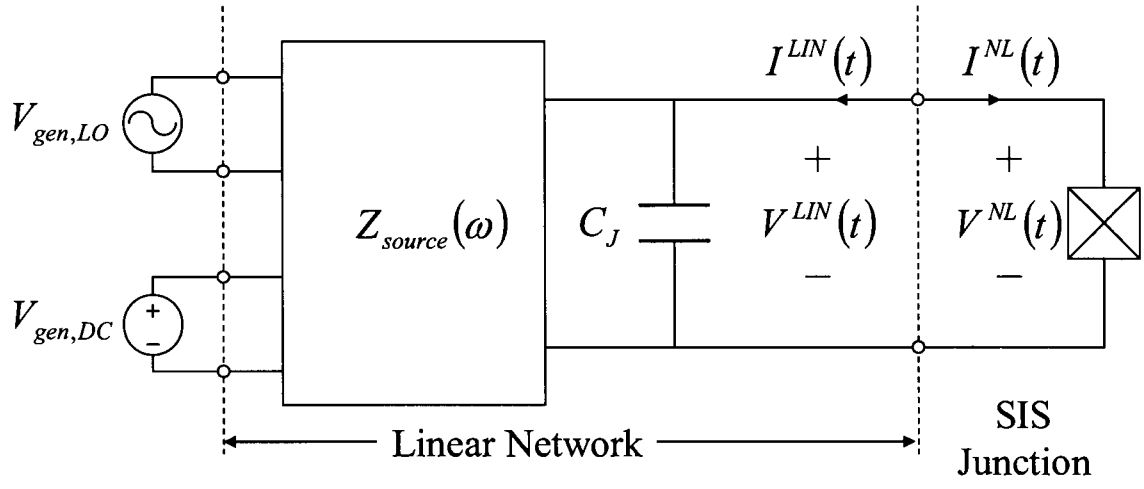

Fig. 38. Circuit describing the relation of the nonlinear diode current to the rest of the circuit in the voltage update algorithm [55]. The nonlinear current is transformed into the frequency domain and then linearly related to each harmonic of the LO.

Once the Fourier amplitudes, V_n^{LIN}, of the linear network voltages have been found, $V^{LIN}(t)$ is calculated through the inverse Fourier transform. If $V^{LIN}(t) = V^{NL}(t)$, then the junction voltage has been found. Otherwise, the voltage may be updated according to

$$V^{NL}(t) = pV^{LIN}(t) + (1-p)V^{NL}(t) \tag{70}$$

where p is a convergence parameter valid over the range of $0 < p < 1$. Convergence is better for the VUM when the terminating impedances approach a short circuit, but it becomes a problem when the source impedance is high compared with the input impedance of the junction [55].

5.2 Variation: Time Domain Voltage Update Method (TDVUM)

Since the VUM computes the linear network voltages in the frequency domain, it is assumed that the voltage waveforms only contain harmonics of the LO and are in a steady state. If the VUM is modified so that all calculations are performed in the time domain, denoted as the *time domain voltage update method* (TDVUM) for comparison purposes, true transient behavior and arbitrary time signals can be analyzed. The new algorithm must be able to evolve with each additional time step, yet still be accurate to the complexities of (62).

Fig. 39 depicts a simplified circuit representation for the TDVUM such that the source impedance is given by a simple resistor. The generator voltage is assumed to include the DC bias. As with the VUM, the terminal voltages are matched through an iterative process. Given a specified generator voltage, an initial guess on the mixer voltage, V_{mix}, is made. The nonlinear diode current is calculated, and the circuit voltage is found by

$$V_{cir}(t) = V_{gen}(t) - I(t)R_{gen} \tag{71}$$

where $t = k\Delta t$ and is evaluated for the k^{th} time step. If the terminal voltages match, then the algorithm is complete; otherwise, V_{mix} is updated according to (70). Matching the voltages at each time step allows for the integration of the algorithm into a time domain circuit or field solver. However, this is not quite as simple as it appears because the current, found by (62), requires a convolution operation that depends on the past history of the voltage across the junction. Therefore, not only is the convolution operation called during each time step, but also for numerous times within each iteration of that time step – creating a very demanding computational algorithm.

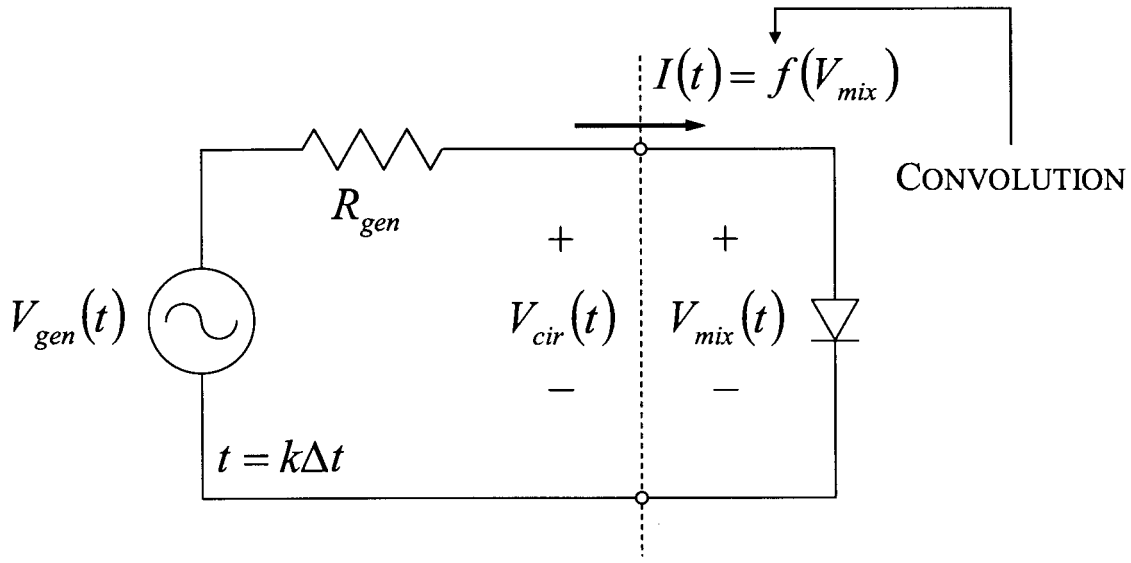

Fig. 39. Circuit describing the time domain voltage update algorithm (TDVUM). The source impedance is represented here as a simple resistor, but can be a more complicated network. For each time step, Δt, the mixer voltage is iteratively matched to the circuit voltage at the terminal interface. However, since the quantum mixer current requires a convolution of previous voltage values, each iteration also requires a convolution. Note that V_{gen} includes the DC voltage bias.

Recall that one simplification to be made is that the storage of the entire voltage time sample is not required; only a time sample equal to the length of the response function, calculated by (59), is necessary. This, of course, assumes that the time sample of the response function is long enough so that it has converged (e.g., longer than what is shown in Fig. 26). The other key to diminishing the computational effort is found in the iteration process. Instead of calculating the entire convolution for each test voltage, the convolution can be computed up to $k-1$ time values and then recalled for subsequent guesses. Using these concepts, a MATLAB [60] algorithm was programmed in the following steps:

- *Initialize parameters* – the I-V curve parameters and time step are determined. The response function is calculated (it only needs to be done once) ensuring that the time sample is long enough to indicate a steady state. Then for each k^{th} time step:
- *Guess initial voltage* $V_{mix} = V_{gen}$.
- *Compute current* – the phase factor and current are calculated for the initial voltage guess and the $k-1$ convolution term is stored.

- *Perform iteration and voltage update* – the circuit of Fig. 39 is solved for each new test voltage. Each voltage guess requires re-calculating the k^{th} term of the phase factor. The current is calculated for the new test voltage and the $k-1$ convolution term is re-used each time. If $V_{cir} = V_{mix}$, then the correct voltage has been found, otherwise, the new test voltage is modified by (70).

5.3 Validation and Comparison of the Two Methods

Since the pumped I-V curve incorporates a high frequency quantum effect (i.e., photon-assisted tunneling), and also because practitioners are familiar with the measured curves, it seems appropriate to compare the two methods above using the predicted pumped I-V curve of each. Given that the operating point of the SIS mixer is usually within the first photon step below the gap, Fig. 40 shows the region over which the VUM and the TDVUM are judged.

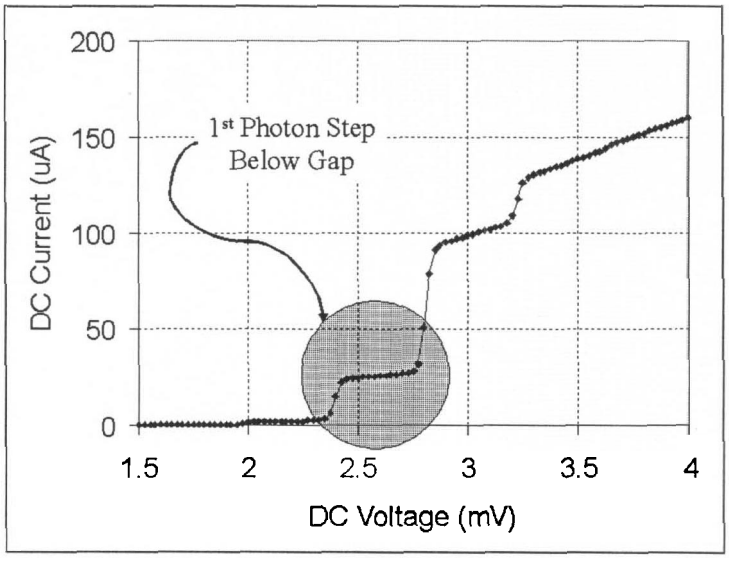

Fig. 40. Predicted pumped I-V curve with no source impedance included (this is not realizable in practice, but demonstrates the $I = f(V)$ relationship). The shaded circle shows the region over which the VUM and TDVUM responses are compared.

When the source impedance is introduced, the voltage waveform across the junction becomes nonlinear due to the diode current. In the fictitious case of zero impedance, the voltage across the mixer is purely sinusoidal, even though the diode current is nonlinear.

Both the VUM and TDVUM show the identical pumped I-V curve when no source impedance is taken into account.

As a consequence of working within the time domain, the source impedance of Fig. 39 must be implemented using real elements. The implication is that if a resistor is used, it is considered ideal and present for all frequencies including DC. In reality, mixer designs have DC bias networks, dispersive transmission line impedances and junction capacitance. More complex source networks, including DC bias elements, can be modeled, but the intention of this section is to keep the demonstration simple.

It is appropriate to define a *source* pumping parameter

$$\alpha_{source} = eV_{gen,AC}/\hbar\omega_{gen} \tag{72}$$

where the distinction is made from (45) in that the voltage, $V_{gen,AC}$, is the amplitude of the AC *generator* voltage, not the voltage established across the junction.

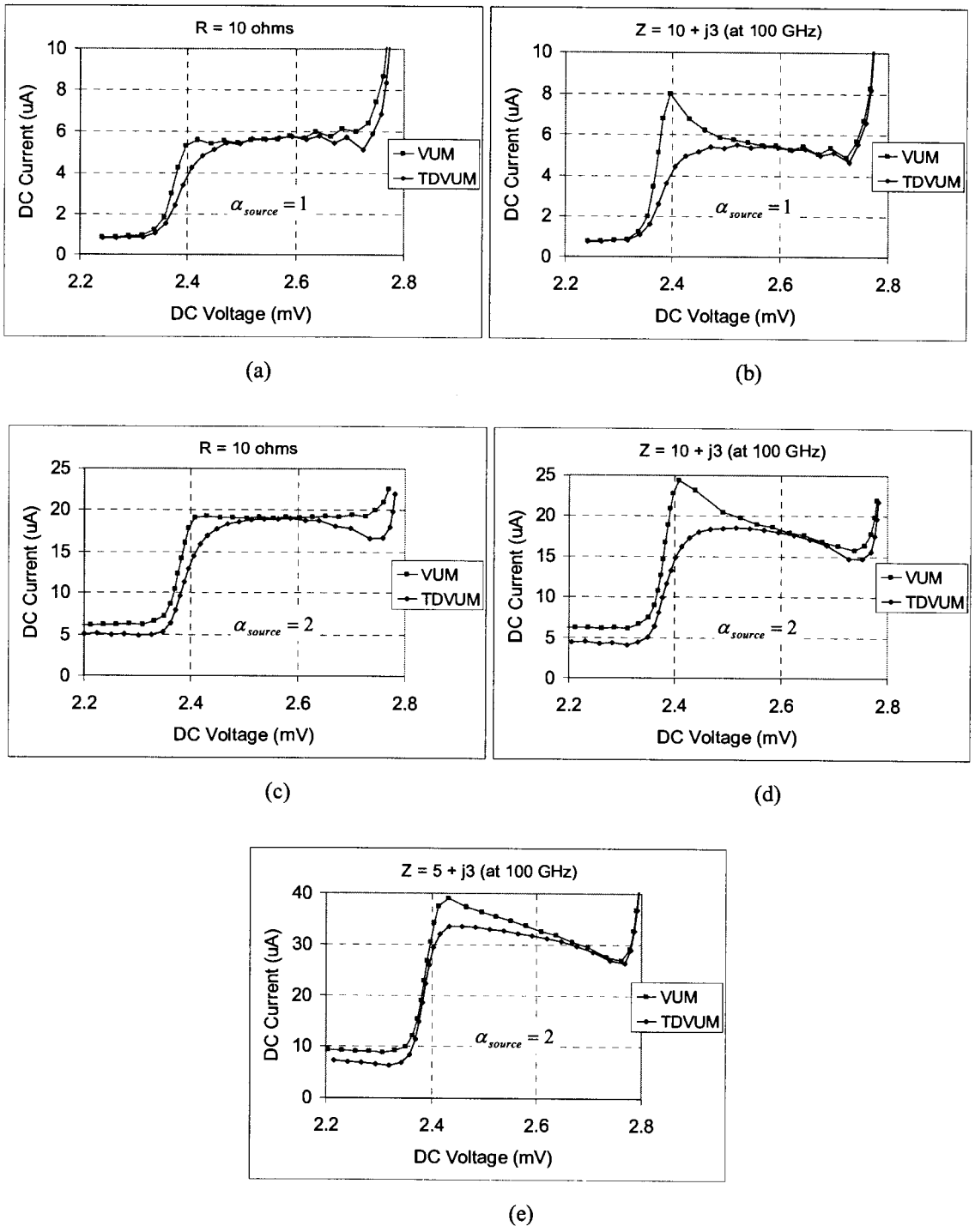

Fig. 41. Comparison of the first photon step as calculated with the VUM and the TDVUM. A source pumping of unity has been used for (a) and (b) and has been doubled for (c)-(e). The source impedance has either been modeled as a simple resistor or as a resistor in series with an inductor.

Fig. 41 shows several photon step predictions for different source impedances. For curves (a) and (b), the VUM was implemented using seven harmonics, i.e., for

$n = 0,1,2,...,7$, and all higher harmonics were considered shorted out. Typically, harmonics past the second or third are short-circuited by the junction capacitance, but they have been included to provide the closest comparison with the TDVUM. The other three cases were calculated only using the DC, fundamental and second harmonic because at higher source pumping, the VUM algorithm would not converge to an acceptable voltage tolerance around the step transition. Each I-V curve was calculated so that the maximum difference between the terminal voltages was 0.01 mV (which is very roughly 2-5% of the mixer voltage amplitude). In theory, the harmonic content of the TDVUM is limited only by the time step, which was set at ~0.05 psec enabling a frequency resolution up to the 100^{th} harmonic. In practice, however, the tolerance value between the test and mixer voltages will become the limitation.

Using (68), the optimum source resistance is found to be $R_{S,opt} \approx 10\,\Omega$, so it is fitting to choose this value for the simple resistive source. To show the interesting effect of an inductive source (causing a negative slope), the impedance was represented by a resistor in series with an inductor chosen to have a reactance of $3\,\Omega$ at 100 GHz. Accordingly, (71) was modified to include the $L\,dI/dt$ term. Relating these models to the VUM, the equivalent embedding impedances were specified as $Z_n^e = 10\,\Omega$ for the resistive source and $Z_n^e = R + jn3\,\Omega$ for the other (to indicate the changing value of the inductor at higher frequencies).

Upon first observation of Fig. 41, it is apparent that the current amplitude over the photon step has been reduced. This is not surprising because the voltage drop across the resistor results in less pumping to the junction. It is curious to see, however, that the VUM exhibits a sharper transition and flatter step. This difference is emphasized in the inductive case as the VUM predicts a large negative slope for the first half of the photon step. Increasing the amplitude of the source, the behavior remains the same. The curve of (e) shows the effect when the resistance is not as dominant.

In all cases, the TDVUM has a more gradual and dampened step transition. This may be as a result of the steady state assumption. Recall that each iteration of the VUM takes an entire voltage time segment as an input. Transient effects of the current are filtered out when the circuit is solved in the Fourier domain, and so the final voltage calculated

across the mixer has no transient and is assumed to be in a steady state. It is assumed that the circuit will arrive at the same steady state response whether or not the transient is included. Alternatively, the TDVUM algorithm is updated in a time-stepping fashion, taking into account the initial conditions and transients that may change how the circuit reaches a steady state. Recall that the SIS junction current is not instantaneously related to the voltage, but that it depends on the past history of the voltage.

The implications are that since the slope is not as pronounced during the first half of the photon step, the TDVUM will predict a conversion gain that is less than the VUM over this region. Furthermore, for a purely resistive case, the TDVUM shows a small roll-off on either side of the step. This would lead to the mixer performance varying at different bias points within the step so that the optimal bias range is smaller than the width of the step itself. In practice, the performance is not constant over the entire step and so the prediction is in agreement. In either case, photon-assisted tunneling is demonstrated and even the phenomenon of a negative dynamic conductance is observed for inductive source impedances.

5.4 Implementation of TDVUM into 3D EM Field Solver (MEFiSTo)

After demonstrating the algorithm of the time domain voltage update method for the large signal condition, the groundwork has been laid for a full embedding into a circuit solver or field solver. MEFiSTo-3D Pro [62] is a full wave 3D electromagnetic field solver that is based on the *transmission line matrix* (TLM) method [63], [64]. An interconnection between SPICE [65] circuit models and the field has already been developed in MEFiSTo by means of representing the TLM network by an equivalent Thévenin or Norton source and impedance [66]. The transmission line impedance is found through an equivalent combination of input link lines. A similar technique was used to implement the SIS quantum theory via a TLM-MATLAB connection.

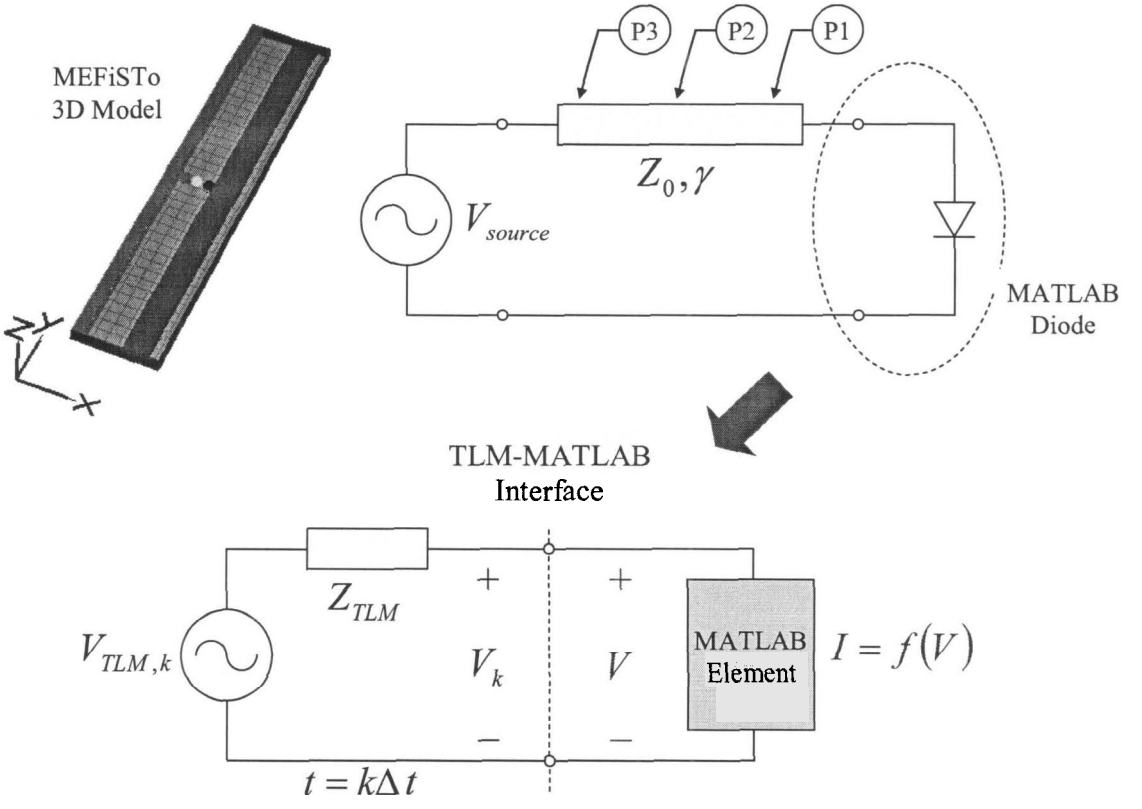

Fig. 42. MEFiSTo implementation of a parallel plate waveguide terminated with a MATLAB diode. The 3D model shows a distributed source connected to a short section of transmission line with three probes placed to monitor the voltage and current at each location. The lower figure describes the TLM-MATLAB interface where the distributed TLM mesh has been reduced to a single Thévenin source and resistance .

In order to confirm the behavior of the MATLAB interface without the complexities of the SIS theory, a nonlinear diode was modeled first. Fig. 42 illustrates a short section of parallel plate waveguide terminated with a shunt diode. The width-to-height ratio of the waveguide is 38:1, so that the equivalent characteristic impedance is $\sim 10\,\Omega$.

A circuit analysis of a $10\,\Omega$ source (consisting of an ideal voltage source in series with a resistor) connected across the MATLAB diode was completed and is shown in Fig. 43. This proved to be a good test venue for the TLM-MATLAB connection because of the drastic changes in the current. One can see that the current has been rectified so that during half of the cycle, the diode appears as an open circuit. This means that in the field simulation, the magnetic field should also be zero at the terminals of the diode. To create a field simulation close to the circuit already analyzed, a very short section ($3\Delta\ell$) of transmission line was used. The mesh resolution was $\Delta\ell = 0.01\,mm$ for a generator wavelength of $\lambda = 3\,mm$. In MEFiSTo, the probes can only be placed at the location of

the link line nodes, but the cell boundaries are marked halfway between the nodes. This means that the three probes in Fig. 42 were placed at $0.5\,\Delta\ell, 1.5\,\Delta\ell$ and $2.5\,\Delta\ell$ away from the MATLAB cell boundary.

In the open circuit condition, the diode acts as a magnetic wall boundary and the electric field is reflected back in phase. Because of the small length of transmission line, each voltage probe response was identical to that obtained in the circuit analysis. However, the magnetic field (a scaled representation of the current) must approach zero at the diode terminal interface. Fig. 44 shows the current measured from each probe and it is apparent that, even at the location of the probe only $0.5\Delta\ell$ away from the MATLAB cell boundary, the magnetic field is not yet zero. In cases such as this, where either the voltage or current tends to zero at the interface, extrapolation is necessary to obtain the true response. According to [66], the actual TLM-MATLAB connection is made halfway between the MATLAB cell boundary and the MATLAB node. Extrapolating under this condition, i.e., $-0.25\Delta\ell$ from the cell boundary, the correct current response is shown in the final two cycles of the waveform in Fig. 44, demonstrating validity in the full field response.

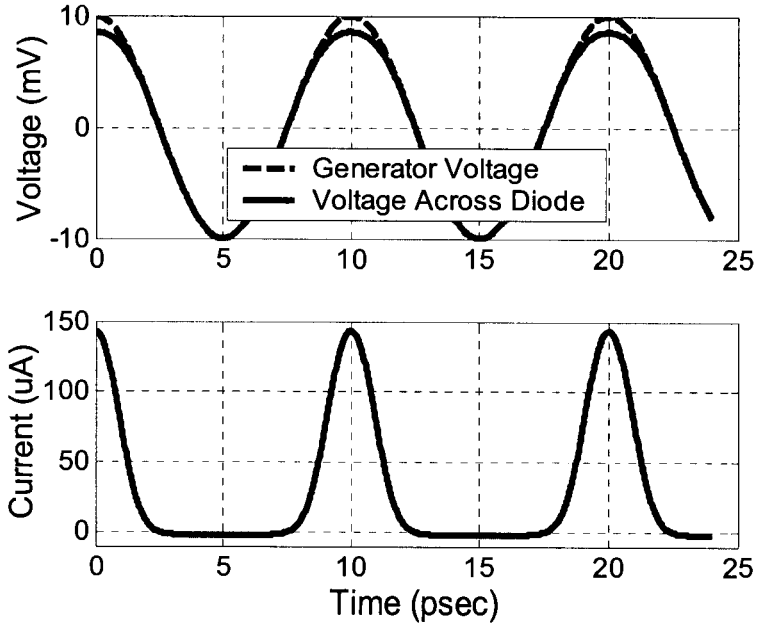

Fig. 43. Circuit response of a $10\,\Omega$ voltage source connected across a diode. The plot representing the generator voltage indicates the waveform of the ideal source before the effects of the source resistance.

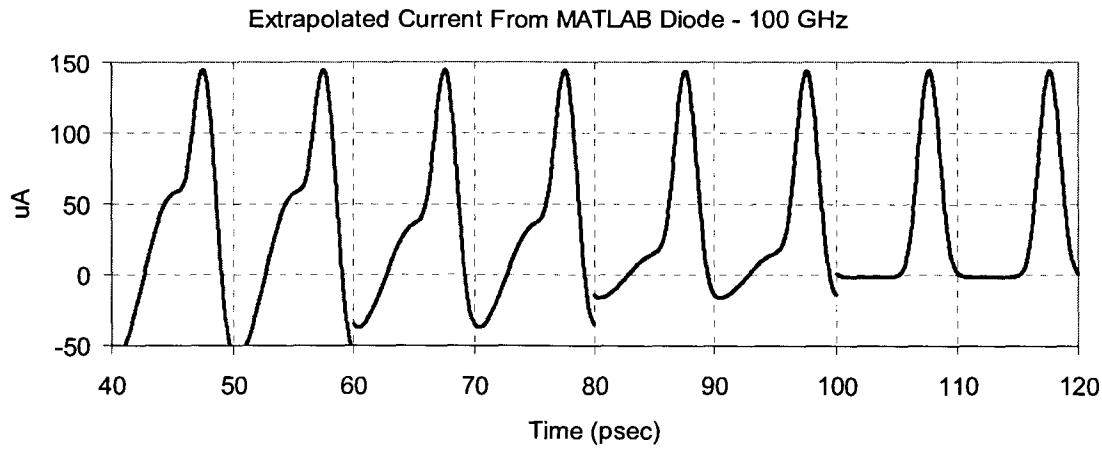

Fig. 44. Progressive view of the current measured through each probe in the MEFiSTo field simulation. The final two periods of the waveform have been determined through extrapolation and indicate the current directly at the TLM-MATLAB connection.

5.4.1 Simple MEFiSTo Implementation of a SIS Circuit

The full time domain SIS mixer algorithm was implemented in MEFiSTo. The MATLAB module calls three functions, *currInit*, *currTest* and *currInstant* (included in Appendix C) that perform the algorithm of the TDVUM as described in section 5.2. Since the time step within MEFiSTo is dependent on the mesh resolution, it was important that the mesh be discretized uniformly in all directions and that the time step was the same within the MATLAB code.

Fig. 45 illustrates the simple model that was used. To maintain continuity with the above results, the parallel plate transmission line was designed to have a characteristic impedance of $10\,\Omega$. MEFiSTo allows the user to attach multiple generators to each source element and so the DC bias voltage and LO were separately defined. A delay was placed on the LO signal to allow for the DC bias to stabilize. Fig. 46 shows the fields sampled by the probes (placed next to the junction). The probe only samples the field along the link line upon which it is placed. As such, the total field across the SIS junction is the sum of all incident lines and the value shown in Fig. 46 must be scaled to make comparisons with the results found above.

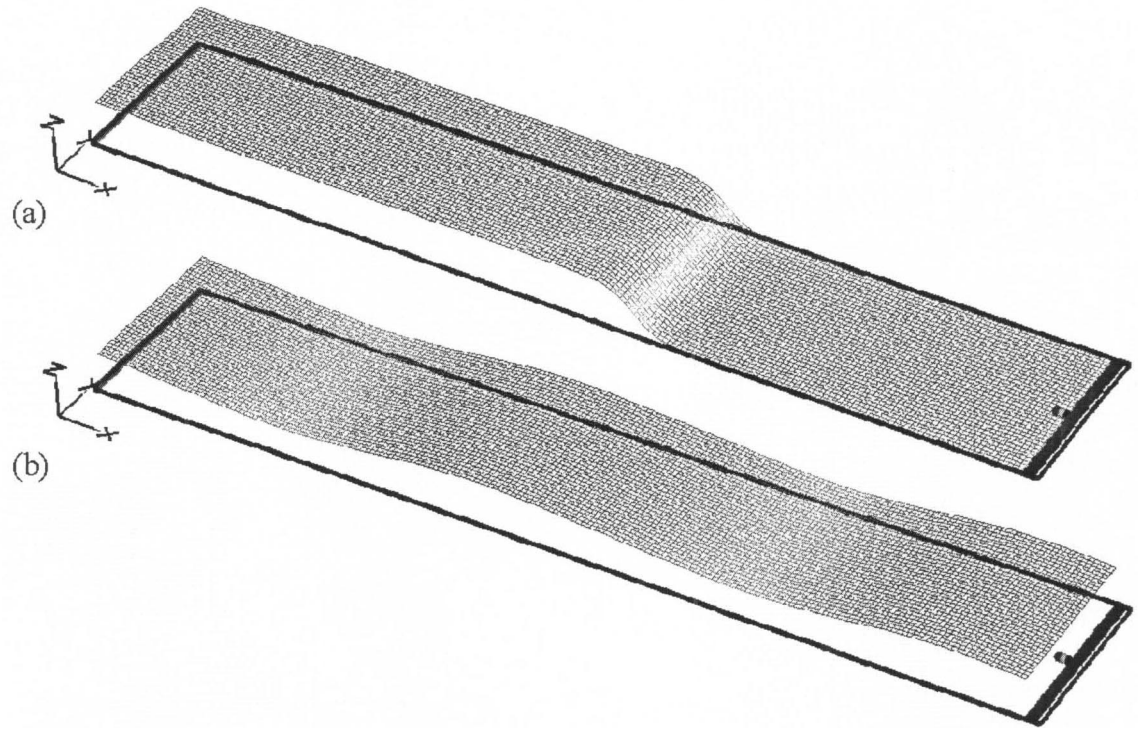

Fig. 45. MEFiSTo model of a parallel plate waveguide terminated with a SIS mixer diode. (a) Transient view capturing the DC bias voltage applied from the generator (left) toward the SIS junction (right). The bias is applied in a ramping fashion to avoid excess ringing in the step response. (b) Steady state view of the local oscillator plus DC voltage distributed across the transmission line.

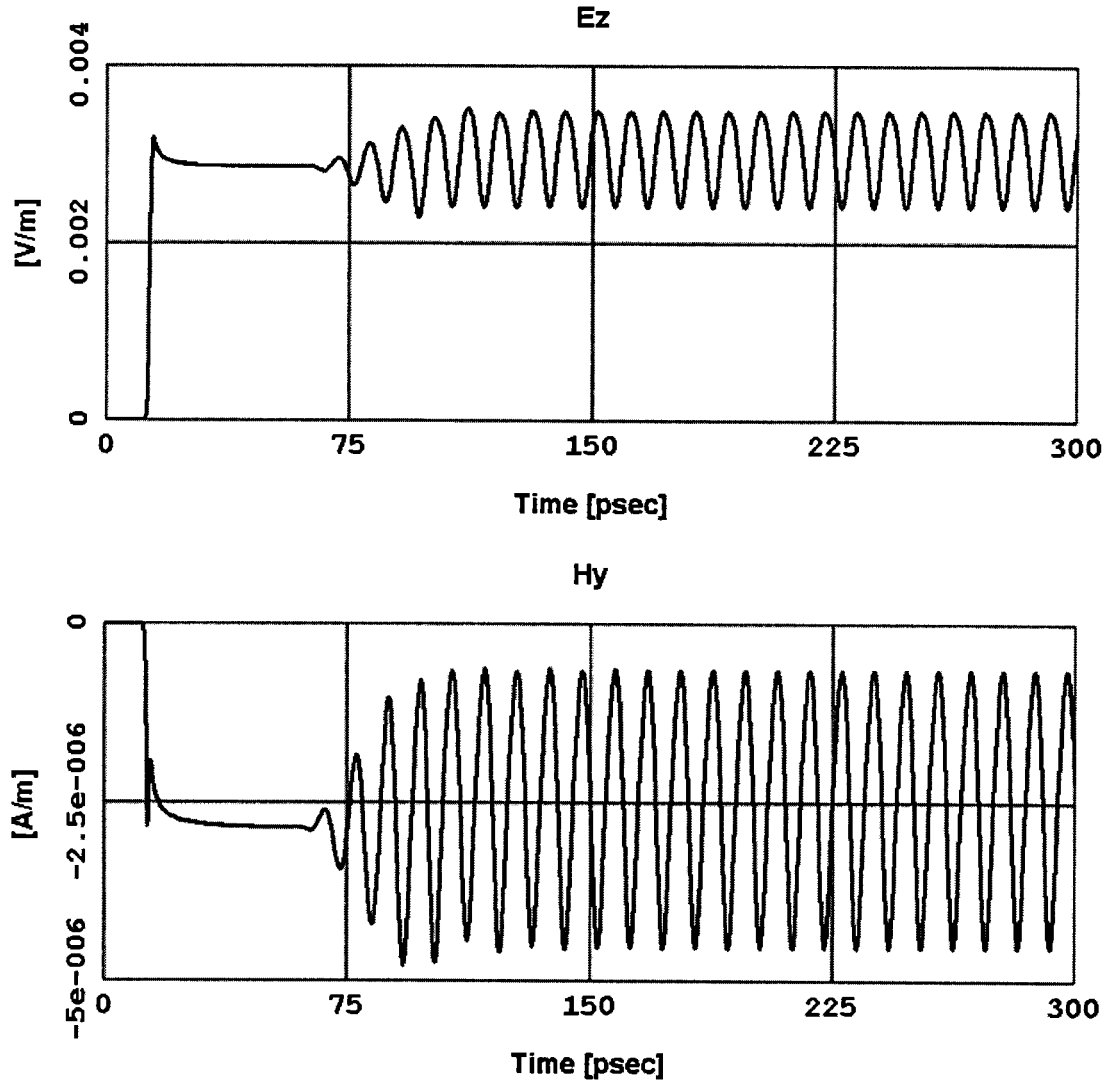

Fig. 46. Electric and magnetic field measured by the probe of the simple SIS model above. The DC bias voltage is applied first, then after some delay the LO is excited.

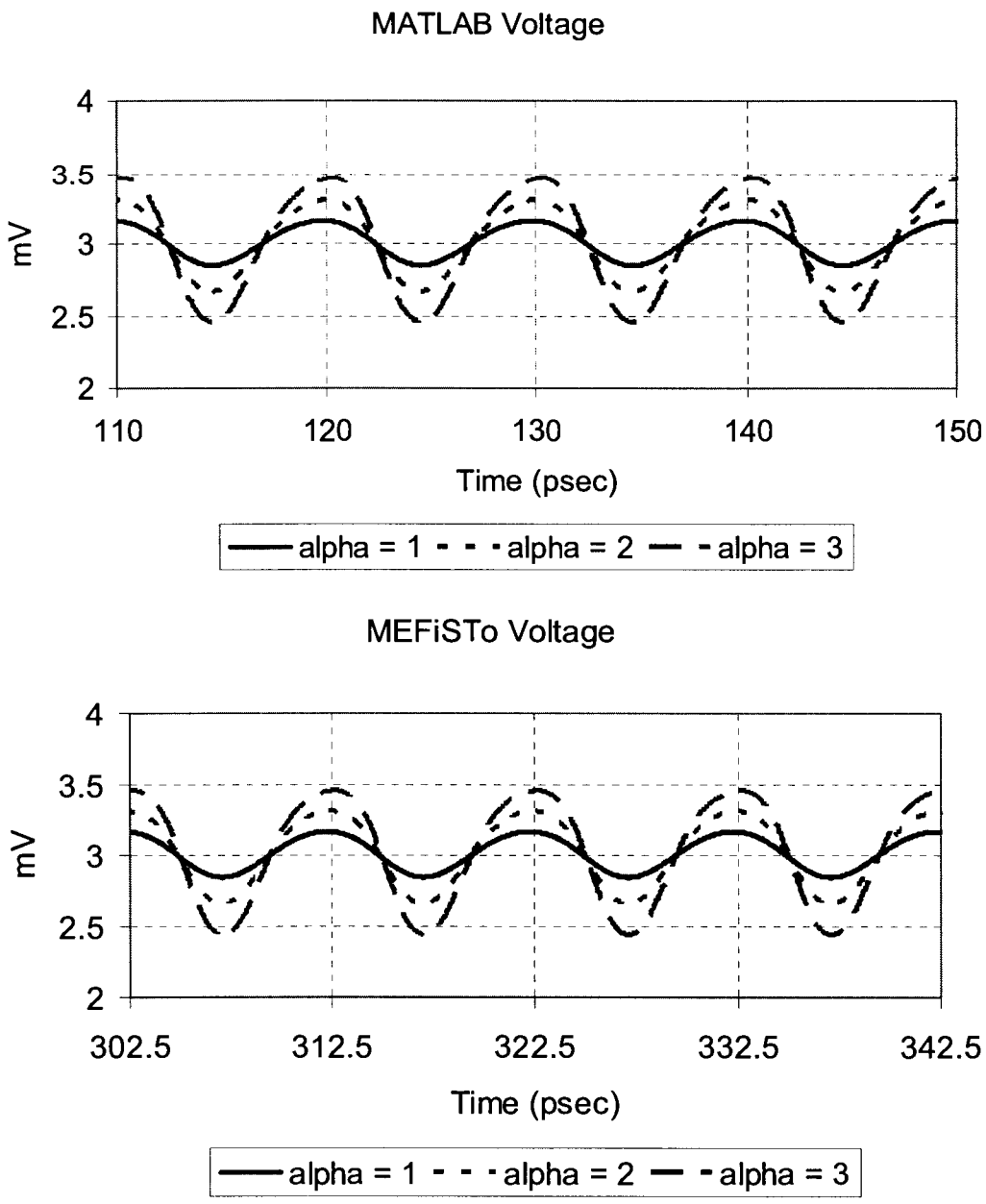

Fig. 47. Comparison of voltages across the SIS junction for different strengths of source voltage as calculated in MATLAB and probed in MEFiSTo. The DC voltage has been set so that the junction is biased at the midpoint of the photon step above the gap.

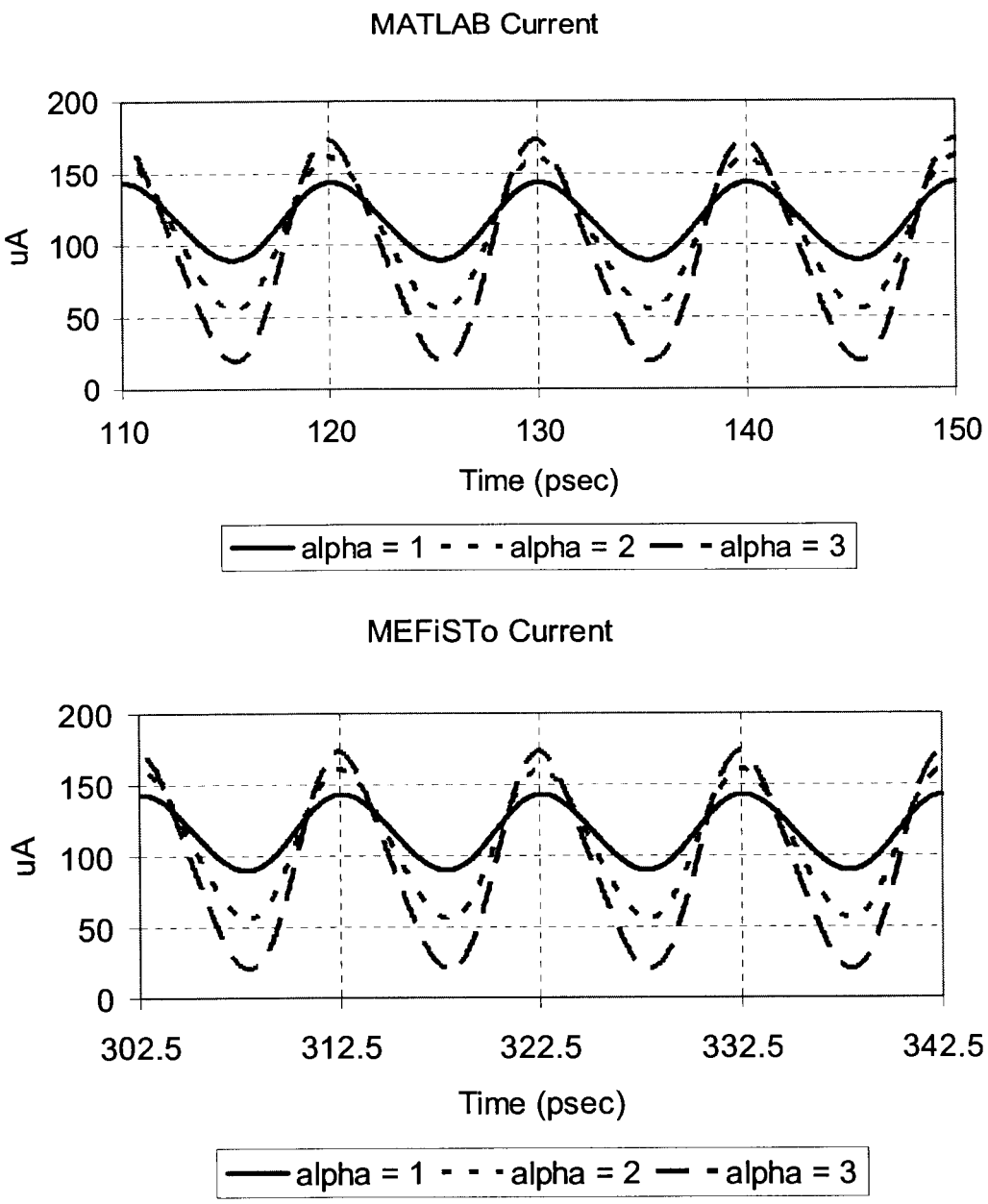

Fig. 48. Comparison of currents through the SIS junction for different strengths of source voltage as calculated in MATLAB and probed in MEFiSTo. The DC voltage has been set so that the junction is biased at the midpoint of the photon step above the gap.

In the same way that the MATLAB diode model was verified by means of a comparison with a circuit analysis, the MATLAB SIS model was compared against the response purely derived using MATLAB. If the waveforms determined match the MEFiSTo result at the TLM-MATLAB connection, then the incident time-varying field is validated. Using a bias point midway along the photon step above the gap, Fig. 47 and

Fig. 48 compare the calculated and measured waveforms for different values of α_{source}. Indeed, the waveforms do match, indicating that the SIS junction has been successfully embedded into the field simulator.

5.4.2 Conclusion and Future Work

The intent of this section has been to describe the process of embedding the SIS mixer theory into a field solver. This has been accomplished by means of a large signal analysis, although the small signal effects have not been demonstrated. Mixing products can, of course, be viewed by simply adding a 2-tone input and there is no limitation against this (even using the exact model described above). To make the results meaningful, however, a quantitative comparison of conversion gain and impedance match against some other method (i.e., frequency domain analysis) would need to be made. This is a large undertaking and is outside of the scope of this thesis, and as such, no small signal results are included.

A great advantage of embedding the SIS model into a time domain field solver is the ability to visualize the fields, including the transient. Fig. 49 shows an example of how MEFiSTo gives insight towards determining the standing wave between the SIS junction and the generator.

Future work to be completed includes implementing a 3-terminal, 2-port MATLAB element. In the above results, a 2-terminal, 1-port element is used to terminate a section of transmission line. Using the 2-port element, an output IF section can be modeled as it appears on the mixer chip. MEFiSTo already has this feature for SPICE elements, so it is not expected to pose a significant problem for implementation. Further experimentation with complex geometries, including biasing networks, junction capacitance, tuning elements and parasitics must also be done.

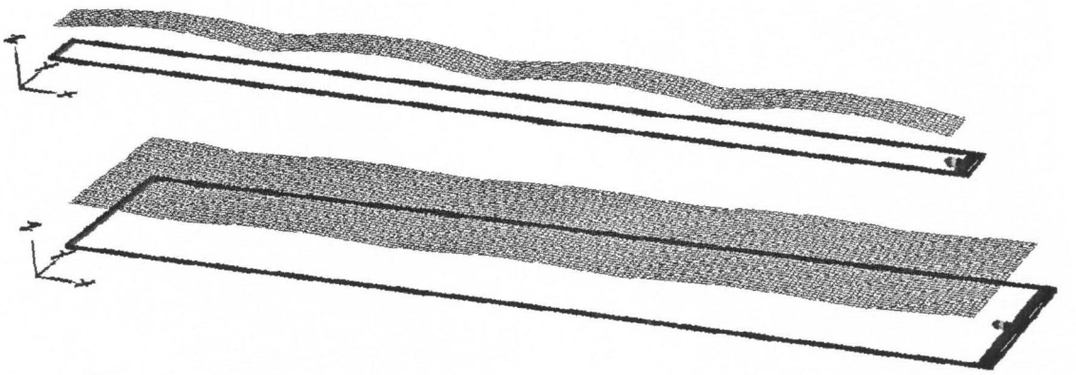

Fig. 49. Envelope of the electric field demonstrating the standing wave for different line impedances. The top figure has a characteristic impedance of 37.7 Ω and clearly shows a larger mismatch than the lower model designed for 10 Ω.

References

[1] R. Bachiller et al., "Science with ALMA," http://www.eso.org/projects/alma/science/, website available as of April, 2005.

[2] http://www.alma.info/ , website available as of April, 2005.

[3] J. Zmuidzinas and P. L. Richards, "Superconducting detectors and mixers for millimeter and submillimeter astrophysics," Proc. IEEE, vol. 92, no. 10, pp. 1597-1616, October 2004.

[4] L. N. Cooper, "Bound electron pairs in a degenerate Fermi gas", Phys. Rev., vol. 104, no. 4, pp. 1189-1190, November 1956.

[5] J. Bardeen, L. N. Cooper and J. R. Schrieffer, "Theory of superconductivity", Phys. Rev., vol. 108, no. 5, pp. 1175-1204, December 1957.

[6] C. Kittel, Introduction to Solid State Physics, 7th Ed. New York: John Wiley & Sons, Inc., 1996.

[7] M. Tinkham, Introduction to Superconductivity, New York: McGraw-Hill, Inc., 1975.

[8] V. Z. Kresin and S. A. Wolf, Fundamentals of Superconductivity, New York: Plenum Press, 1990.

[9] B. G. Streetman, Solid State Electronic Devices, 4th Ed., New Jersey: Prentice-Hall, Inc., 1995.

[10] P. A. Tipler, Physics, 3rd Ed. New York: Worth Publishers, Inc., 1991.

[11] R. A. Serway, Physics for Scientists and Engineers, 3rd Ed. Toronto: Saunders College Publishing, 1990.

[12] I. Giaever and K. Megerle, "Study of superconductors by electron tunneling", Phys. Rev., vol. 122, no. 4, pp. 1101-1111, May 1961.

[13] A. H. Daymen and R. J. Martin, "Quantum interaction of microwave radiation with tunneling between superconductors", Phys. Rev. Lett., vol. 8, no. 6, pp. 246-248, March 1962.

[14] M. H. Cohen, L. M. Falicov and J. C. Phillips, "Superconductive tunneling", Phys. Rev. Lett., vol. 8, no. 8, pp. 316-318, April 1962.

[15] B. D. Josephson, "Possible new effects in superconductive tunnelling", Phys. Lett., vol. 1, no. 7, pp. 251-253, July 1962.

[16] B. D. Josephson, "Coupled superconductors", Rev. Mod. Phys., vol. 36, no. 1, pp. 216-220, January 1964.

[17] P. K. Tien and J. P. Gordon, "Multiphoton process observed in the interaction of microwave fields with the tunneling between superconductor films", Phys. Rev., vol. 129, no. 2, pp. 647-651, January 1963.

[18] N. R. Werthamer, "Nonlinear self-coupling of Josephson radiation in superconducting tunnel junctions", Phys. Rev., vol. 147, no. 1, pp. 255-263, July 1966.

[19] J. R. Tucker, "Quantum Limited Detection in Tunnel Junctions Mixers," IEEE J. of Quantum Electronics., vol. QE-19, no. 11, pp. 1234-1258, November 1979.

[20] J. R. Tucker, "The quantum response of nonlinear tunnel junctions as detectors and mixers," Reviews of Infrared and Millimeter Waves, New York: Plenum, vol. 1, pp. 1-46, 1983.

[21] J. R. Tucker and M. J. Feldman, "Quantum Detection at Millimeter Wavelengths," Rev. Mod. Phys., vol. 57, no. 4, pp. 1055-1113, October 1985.

[22] J. R. Tucker, "Predicted conversion gain in superconductor-insulator-superconductor quasiparticle mixers," Appl. Phys. Lett., vol. 36, no. 6, pp. 477-479, March 1980.

[23] L. D. Landau and E. M. Lifshitz, Quantum mechanics (course of theoretical physics; vol. 3), 3rd Ed., New York: Pergamon Press Inc., 1977

[24] L. R. D'Addario, "Noise parameters of SIS mixers," IEEE Trans. Microwaves Theory Tech., vol. 36, no. 7, pp. 1196-1206, July 1988.

[25] M. J. Wengler, "Submillimeter-wave detection with superconducting tunnel diodes", Proc. IEEE, vol. 80, no. 11, pp. 1810-1826, November 1992.

[26] R. E. Harris, "Josephson tunneling current in the presence of a time-dependent voltage," Phys. Rev. B, vol. 11, no. 9, pp. 3329-3333, May 1975.

[27] R. E. Harris, "Intrinsic Response Time of a Josephson Tunnel Junction", Phys. Rev. B, vol. 13, no. 9, pp. 3818-3821, May 1976.

[28] R. E. Harris, "Numerical evaluation of the response of a Josephson tunnel junction in an arbitrary circuit," J. Appl. Phys., vol. 48, no. 12, pp. 5188-5190, December 1977.

[29] R. E. Harris, "Comments on the roles of the cosine term and the reactive part of the quasiparticle term in the Josephson tunneling current," IEEE Trans. Magn., vol. MAG-11, no. 2, pp. 856-857, March 1975.

[30] D. G. McDonald, R. L. Peterson, C. A. Hamilton, R. E. Harris, and R. L. Kautz, "Picosecond applications of Josephson junctions," IEEE Trans. Electron Devices, vol. ED-27, no. 10, pp. 1945-1965, October 1980.

[31] A. R. Kerr, M. J. Feldman and S. -K. Pan, "Receiver Noise Temperature, the Quantum Noise Limit, and the Role of the Zero-Point Fluctuations," 8th Int. Symp. On Space Terahertz Tech., pp. 101-111, March 25-27, 1997, also available as ALMA Memo 161.

[32] A. R. Kerr, "Suggestions for Revised Definitions of Noise Quantities, Including Quantum Effects," ALMA Memo 236, Nov. 10, 1998.

[33] H. B. Callen and T. A. Welton, "Irreversibility and generalized noise", Phys. Rev., vol. 83, no. 1, pp. 34-40, July 1951.

[34] M. J. Feldman, S. -K. Pan, A. R. Kerr and A. Davidson, "SIS mixer analysis using a scale model," IEEE Trans. Magn., vol. MAG-19, no. 3, pp. 494 - 497, May 1983.

[35] A. R. Kerr and S. -K. Pan, "Some recent developments in the design of SIS mixers," Int. J. Infrared Millimeter Waves, vol. 11, no. 10, pp. 1169-1187, October 1990.

[36] A. R. Kerr, S. -K. Pan, A. W. Lichtenberger, and D. M. Lea, "Progress on tunerless SIS mixers for the 200-300 GHz band," IEEE Microwave Guided Wave Lett., vol. 2, no. 11, pp. 454-456, November 1992.

[37] A. R. Kerr, "Some fundamental and practical limits on broadband matching to capacitive devices, and the implications for SIS mixer design," IEEE Trans. Microwaves Theory Tech., vol. 43, no. 1, pp. 2-13, January 1995.

[38] S. M. X. Claude, "Lead Alloy Superconducting Tunnel Junctions for Submillimetre Wave Heterodyne Detection," Ph.D. dissertation, Queen Mary and Westfield College, University of London, London, 1996.

[39] M. Bin, "Low-noise THz niobium SIS mixers," Ph.D. dissertation, California Institute of Technology, Pasadena, California, 1997.

[40] A. R. Kerr, S. -K. Pan, A. W. Lichtenberger and H. H. Huang, "A tunerless SIS mixer for 200-280 GHz with low output capacitance and inductance," 9th Int. Symp. on Space Terahertz Tech., pp. 195-203, March 1998, also avail. as ALMA Memo 205.

[41] S. M. X. Claude, C. T. Cunningham, A. R. Kerr and S.-K. Pan, "Design of a Sideband-Separating Balanced SIS Mixer Based on Waveguide Hybrids," ALMA Memo 316, Sept. 20, 2000.

[42] A. R. Kerr, S. -K. Pan and J. E. Effland, "Sideband Calibration of Millimeter-Wave Receivers," ALMA Memo 357, Mar. 27, 2001.

[43] A. Navarrini, "Development of DSB and SSB SIS mixers for radio astronomy in the frequency band 250-370 GHz," Ph. D. dissertation, Université Joseph Fourier, Grenoble, France, 2002.

[44] S. Asayama, T. Noguchi and H. Ogawa, "A fixed –tuned W-band waveguide SIS mixer with 4.0-7.5 GHz IF," Int. J. Infrared Millimeter Waves, vol. 24, no. 7, pp. 1091-1099, July 2003.

[45] S. -K. Pan, A. R. Kerr, M. W. Pospieszalski, E. F. Lauria, W. K. Crady, N. Horner, Jr., S. Srikanth, E. Bryerton, K. Saini, S. M. X. Claude, C. C. Chin, P. Dindo, G. Rodrigues, D. Derdall, J. Z. Zhang and A. W. Lichtenberger, "A Fixed-Tuned SIS Mixer with Ultra-Wide-Band IF and Quantum-Limited Sensitivity for ALMA Band 3 (84-116 GHz) Receivers," 15th Int. Symp. on Space Terahertz Tech., Northampton, MA, April 2004.

[46] S. -K. Pan, Section 5.6.2.2, SIS Mixer Development for band 3 in ALMA Construction Project Book, http://www.alma.nrao.edu/projectbk/construction/chap5/chap5.pdf, website available as of April, 2005.

[47] C. C. Chin, D. Derdall, J. Sebesta, F. Jiang, P. Dindo, G. Rodrigues, D. Bond, S. -K. Pan, A. R. Kerr, E. Lauria, M. Pospieszalski, J. Zhang, T. Cecil and A. Lichtenberger, "A low noise 100 GHz sideband-separating receiver," Int. J. Infrared Millimeter Waves, vol. 25, no. 4, pp. 569-600, April 2004.

[48] ALMA Band 3 Preliminary Design Review (PDR), Document FEND-40.90.00.00-001-A-REP, version A, Mar. 10, 2004.

[49] D. M. Pozar, Microwave Engineering, 2nd Ed. New York: John Wiley & Sons, Inc., 1998.

[50] S. M. X. Claude, "Local Oscillator Coupling and System Noise," HIA ALMA Band 3 Internal Report, Feb. 18, 2003.

[51] P. Dindo, "Microwave Circuit Design of the Warm IF Chain," HIA ALMA Band 3 Internal Report, Sept. 8, 2003.

[52] P. Dindo and D. Derdall, "SIS Mixer Test Report: N11_A2_2," HIA ALMA Band 3 Internal Report, July, 2004.

[53] A. R. Kerr, "A technique for determining the local oscillator waveforms in a microwave mixer," IEEE Trans. Microwaves Theory Tech., vol. 23, no. 10, pp. 828-831, October 1975.

[54] R. G. Hicks and P. J. Khan, "Numerical analysis of nonlinear solid-state device excitation in microwave circuits," IEEE Trans. Microwaves Theory Tech., vol. 30, no. 3, pp. 251-259, March 1982.

[55] R. G. Hicks, M. J. Feldman, and A. R. Kerr, "A general numerical analysis of the superconducting quasiparticle mixer," IEEE Trans. Magn., vol. MAG-21, no. 2, pp. 208-211, March 1985.

[56] A. R. Kerr, S. -K. Pan, and S. Withington, "Embedding impedance approximations in the analysis of SIS mixers," IEEE Trans. Microwave Theory Tech., vol. 41, no. 4, pp. 590-594, April 1993.

[57] P. Dieleman, H. G. Bukkems and T. M. Klapwijk, "Observation of Andreev reflection enhanced shot noise," Phys. Rev. Lett., vol. 79, no. 18, pp. 3486-3489, November 1997.

[58] A. R. Kerr, "Surface impedance of superconductors and normal conductors in EM simulators," ALMA Memo 245, Rev. Aug. 9, 1999.

[59] J. Ward, F. Rice, G. Chattopadhyay and J. Zmuidzinas, "SuperMix: A Flexible Software Library for High-Frequency Circuit Simulation, Including SIS Mixers and Superconducting Elements," 10th Int. Symp. on Space Terahertz Tech., 1999 Proceedings. Avail. at http://www.submm.caltech.edu/supermix/, website available as of April, 2005.

[60] MATLAB, The MathWorks, Inc., 3 Apple Hill Drive, Natick, MA 01760-2098, USA, http://www.mathworks.com, website available as of April, 2005.

[61] CST Microwave Studio, CST of America, Inc., 10 Laurel Avenue, Suite 300, Wellesley Hills, MA 02481, USA, http://www.cst-america.com, website available as of April, 2005.

[62] MEFiSTo-3D Pro, FAUSTUS Scientific Corporation, 1256 Beach Drive, Victoria, BC, V8S 2N3, Canada, http://www.faustcorp.com, website available as of April, 2005.

[63] P, B. Johns, "The art of modeling," IEE Trans. Electron. Power, vol. 25, no. 8, pp. 565–569, August 1979.

[64] W. J. R. Hoefer, "The transmission-line matrix method—Theory and applications," IEEE Trans. Microwave Theory Tech., vol. MTT-33, pp. 882-893, October 1985.

[65] SPICE, University of California, Berkeley, USA, http://bwrc.eecs.berkeley.edu/Classes/IcBook/SPICE/, website available as of April, 2005.

[66] P. P. M. So and W. J. R. Hoefer, "A TLM-SPICE interconnection framework for coupled field and circuit analysis in the time domain," IEEE Trans. Microwaves Theory Tech., vol. 50, no. 12, pp. 2728-2733, December 2002.

[67] Eccosorb, Emerson & Cuming Microwave Products, 28 York Ave., Randolph, MA 02368, USA, http://www.eccosorb.com, website available as of April, 2005.

Note: ALMA Memos are available at http://www.alma.nrao.edu/memos/index.html, website available as of April, 2005.

Appendix A Measured DSB Results of Mixers Used in 2SB Receiver

The following plot has been taken from [52] and measured with a different cryostat then the one used for the measurements in section 2. These two mixers do not have the superior noise performance as measured for mixer J1 (shown in section 2.2.2), but may still be acceptable for the final receiver cartridge.

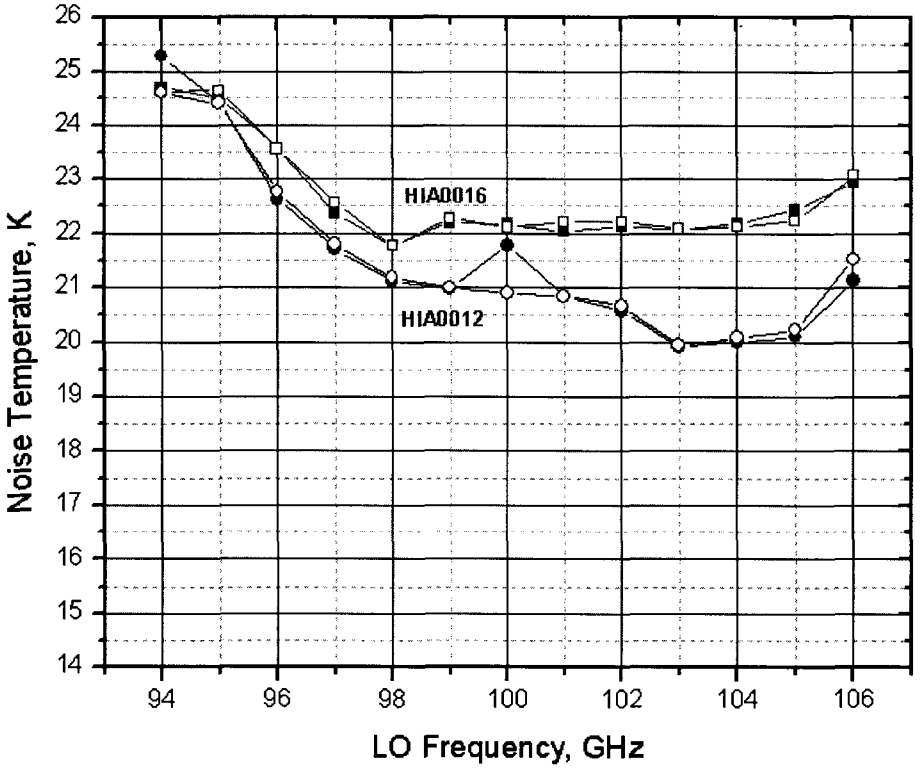

Fig. 50. DSB Noise for Mixers 0012 and 0016.

Appendix B Waveguide Inline Absorber Designs

The following waveguide inline attenuator designs (for use as the cold LO attenuator) have been simulated using CST [61]. The attenuator is either machined or cast-molded from Eccosorb MF-117 [67], which is a magnetically-loaded, machinable epoxy. The parameters for the Eccosorb are not specified to 100 GHz, so as a start, the values at 18 GHz were used. An insertion loss of 10 dB ± 2 dB across the band of 92-108 GHz was necessary. A "WR-9.6" rectangular waveguide was used (such that the width of the waveguide is 0.096"). The specifications were such that Port 1 was required to have at least 10 dB return loss and port 2 to have at least 15 dB return loss. The design was to be less than 5 mm in length and must exhibit repeatable performance subject to a 50 μm machining tolerance. VNA measurements are provided for the three-step (two different samples), wedge and flat section design. S-parameters, given in dB, are plotted for both the simulation results and the measurements.

Initial Four-Step Design

This design had very good simulated performance, but was impractical to manufacture (especially the last step thickness). The table below gives the dimensions, specified in millimeters, for each step (*Hstep* for height and *Lstep* for length). The first step corresponds to the leftmost step.

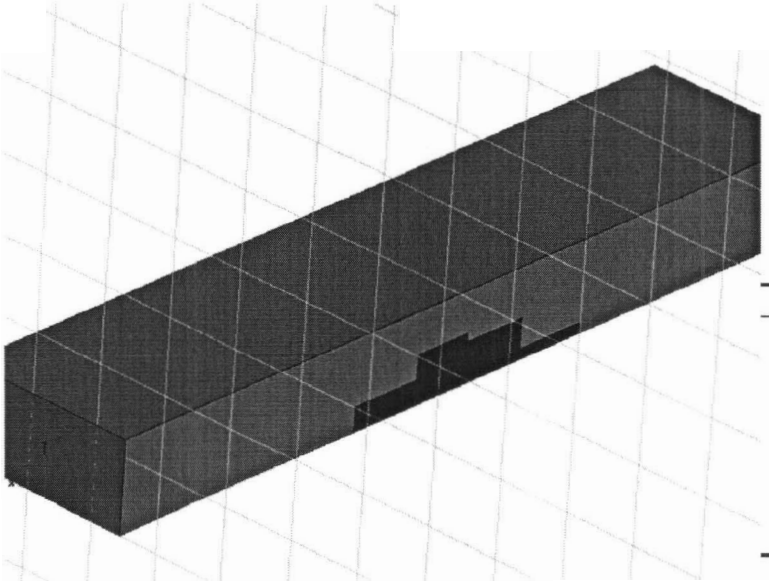

Parameter	*[mm]*
Hstep1	0.33
Hstep2	0.65
Hstep3	0.54
Hstep4	0.14
Lstep1	1
Lstep2	0.81
Lstep3	0.91
Lstep4	1

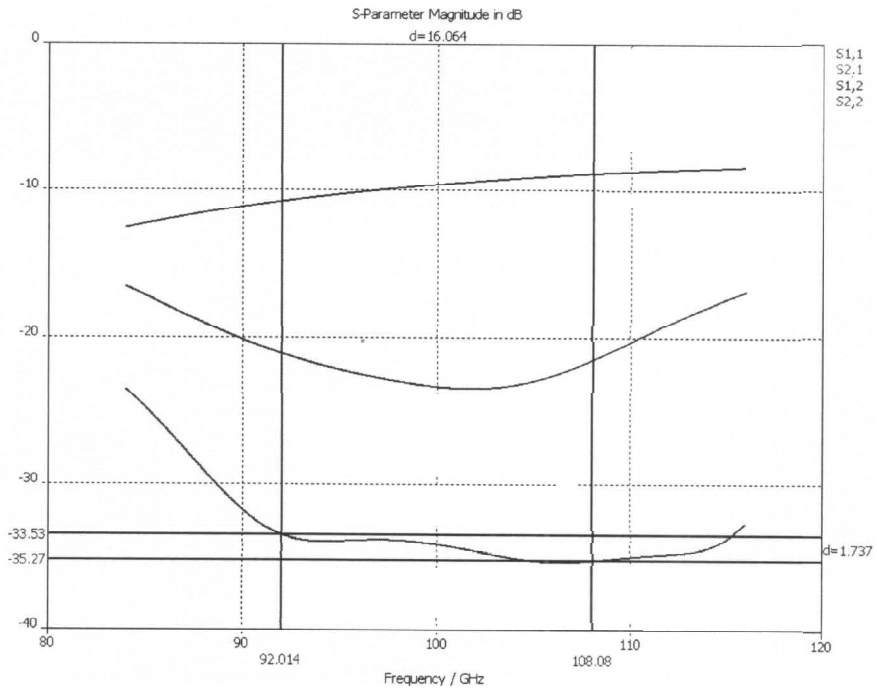

Three-step Design

The above design was simplified. Because of its symmetric design, both assembly and machining is made easier.

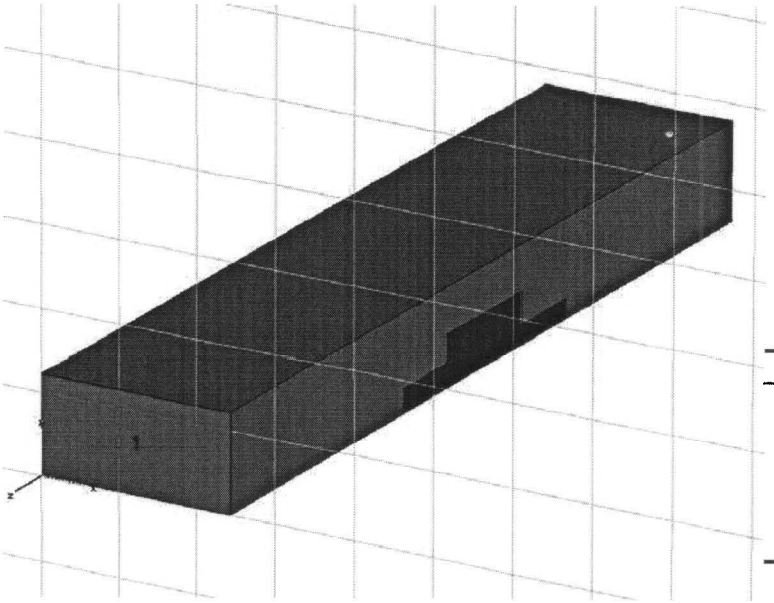

Parameter	***[mm]***
Hstep1	0.25
Hstep2	0.65
Hstep3	0.25
Lstep1	1
Lstep2	1.67
Lstep3	1

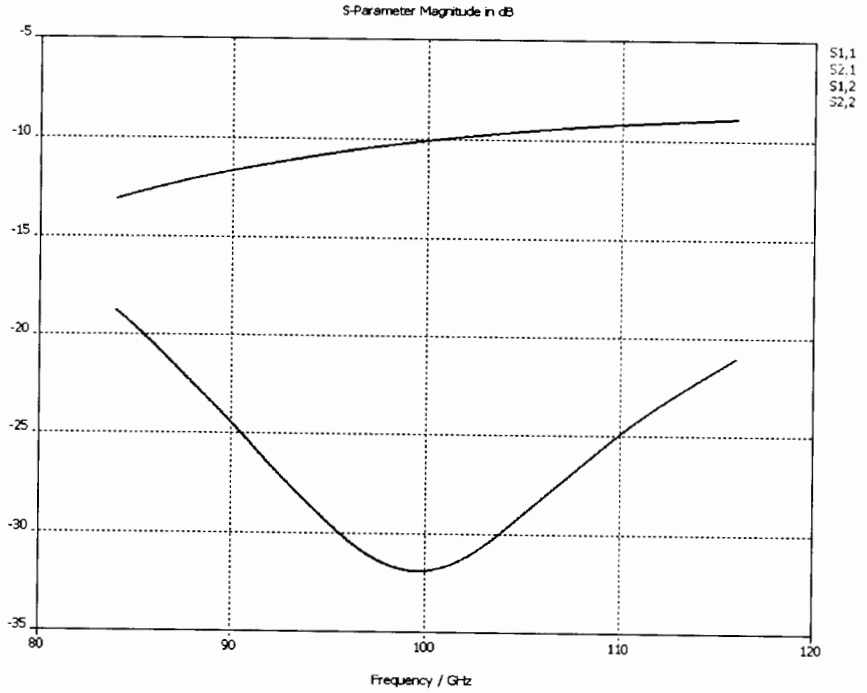
S-Parameter Magnitude in dB
-5
-10
-15
-20
-25
-30
-35
80
90
100
110
120
Frequency / GHz
S1,1
S2,1
S1,2
S2,2

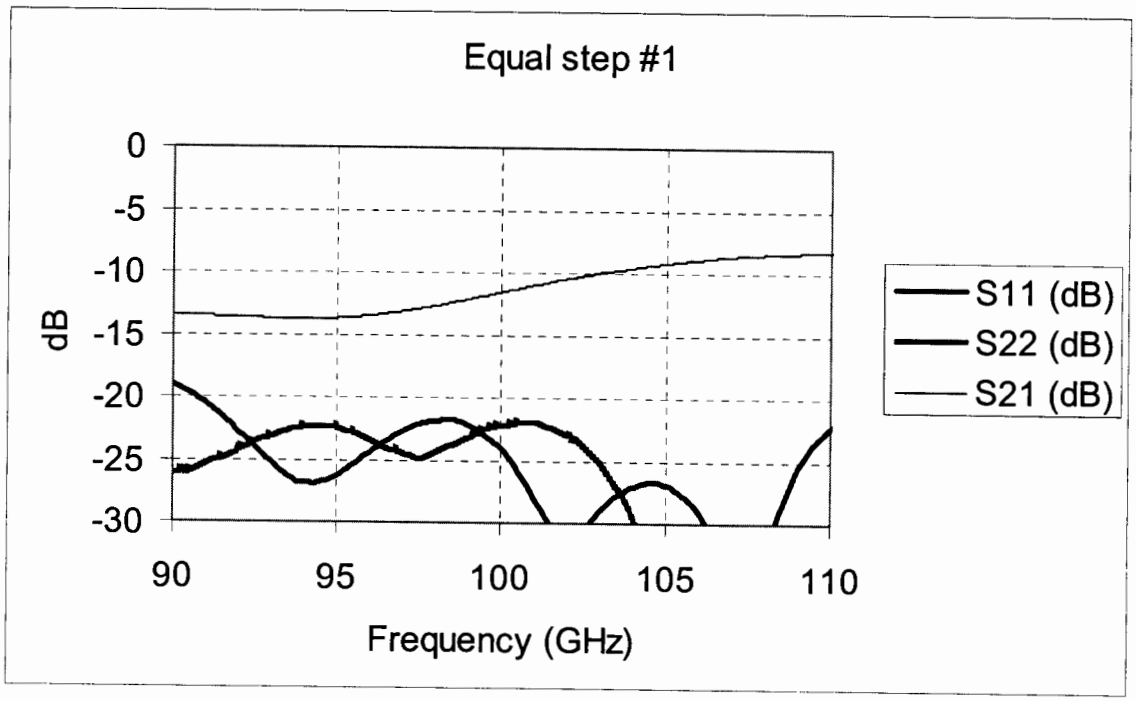
Equal step #1
0
-5
-10
-15
-20
-25
-30
dB
90
95
100
105
110
Frequency (GHz)
S11 (dB)
S22 (dB)
S21 (dB)

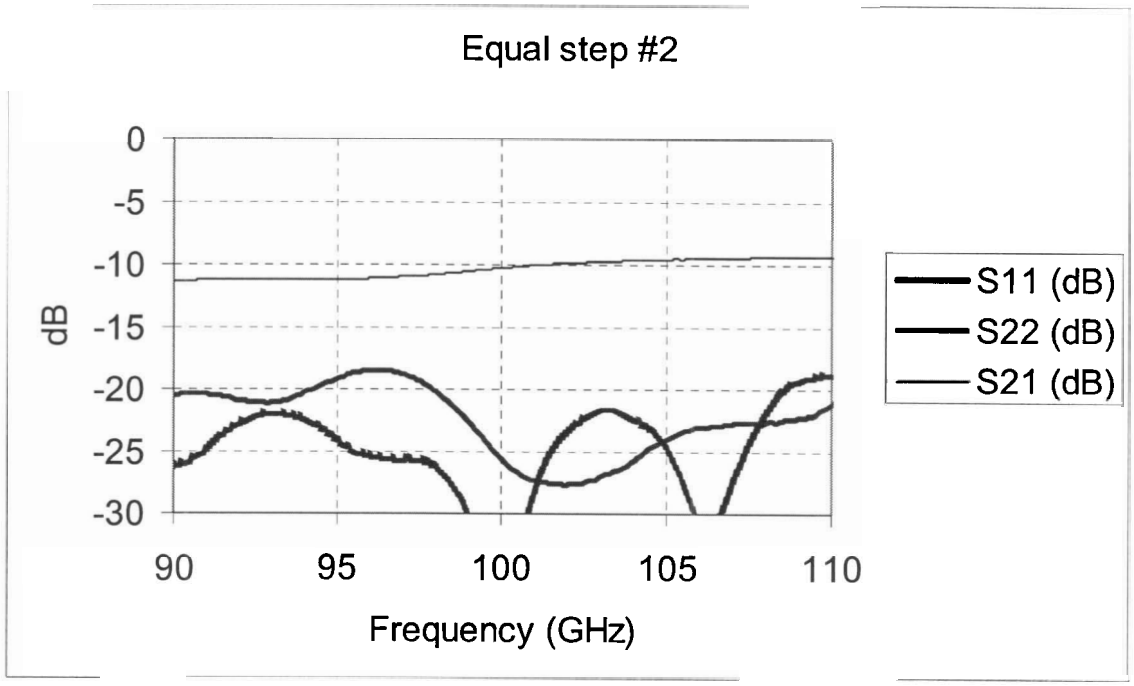

One Dimensional Wedge Design (5mm)

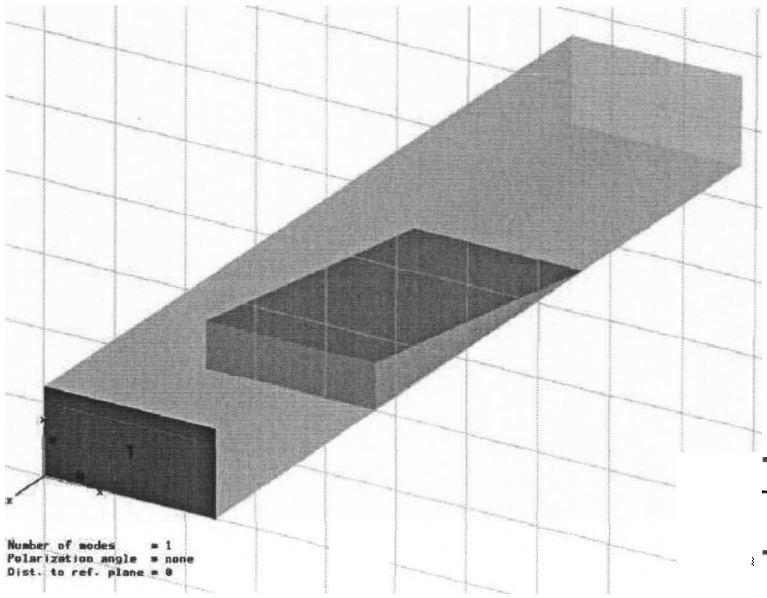

Parameter	*[mm]*
Height	0.65
Length	5

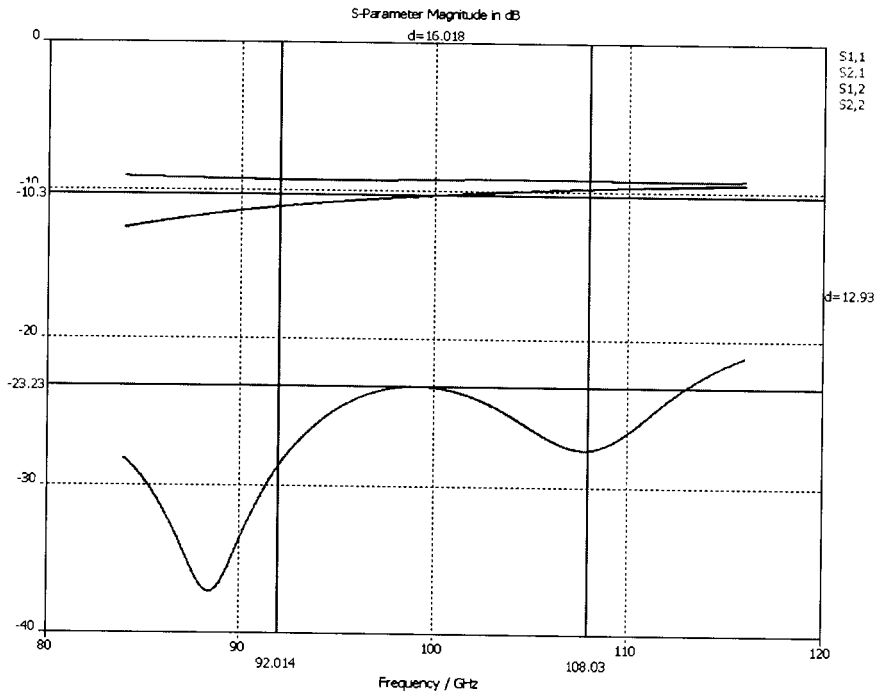
S-Parameter Magnitude in dB
d=16.018
S1,1
S2,1
S1,2
S2,2
d=12.93
0
-10
-10.3
-20
-23.23
-30
-40
80
90
92.014
100
108.03
110
120
Frequency / GHz

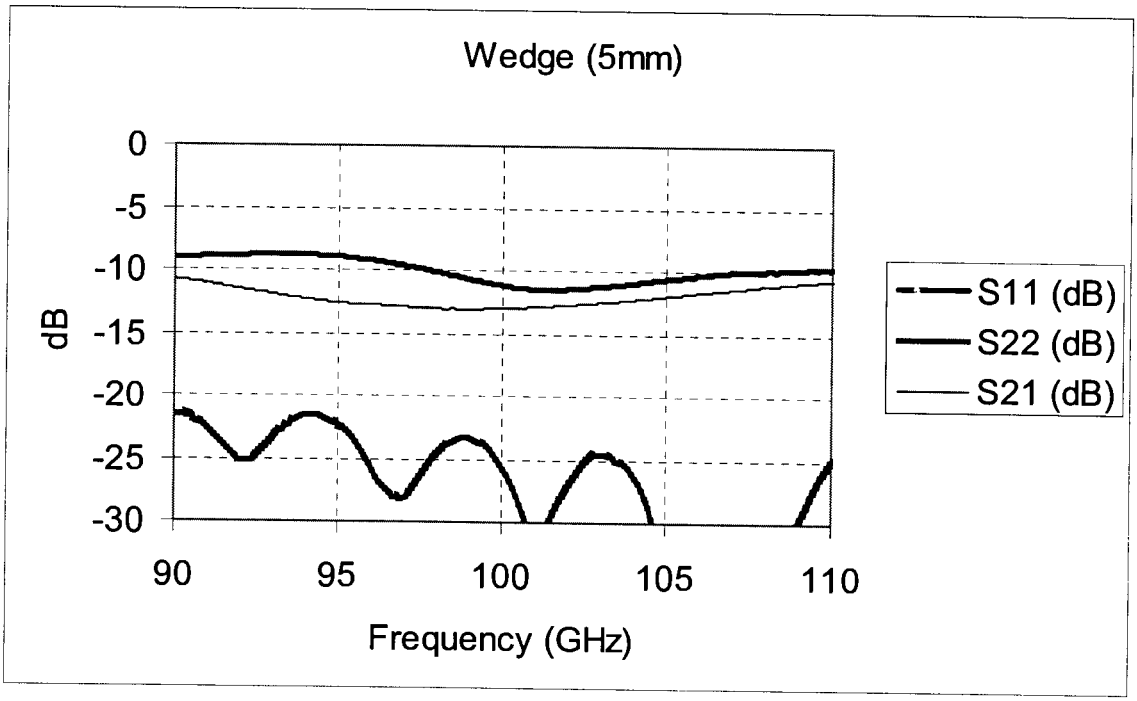
Wedge (5mm)
0
-5
-10
-15
-20
-25
-30
dB
90
95
100
105
110
Frequency (GHz)
S11 (dB)
S22 (dB)
S21 (dB)

Flat Section of Eccosorb

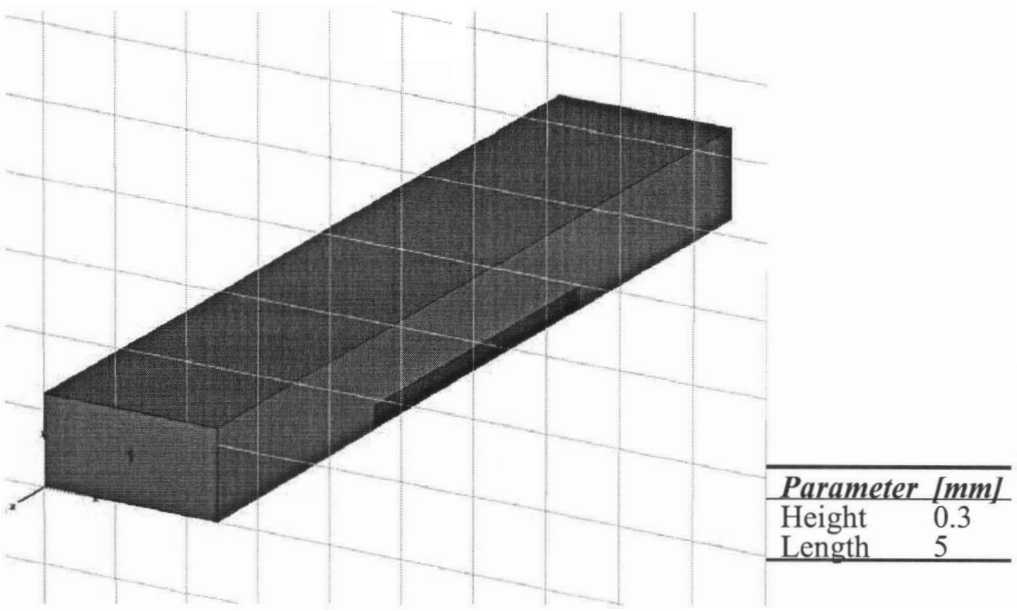

Parameter	*[mm]*
Height	0.3
Length	5

The thickness was modeled for 200, 300 and 400 μm and the variation is shown below. The measured sample was machined at 300 μm.

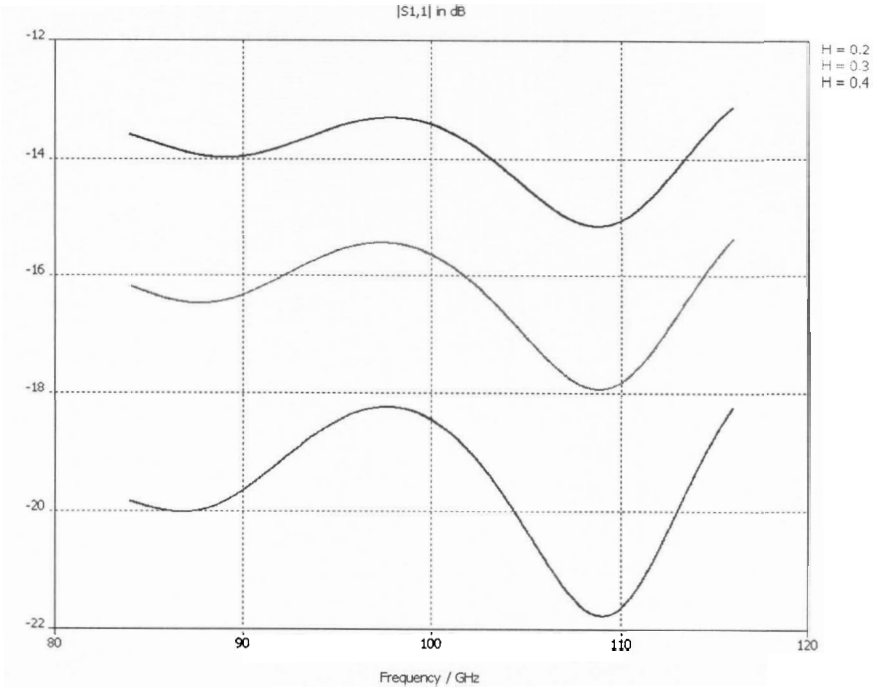

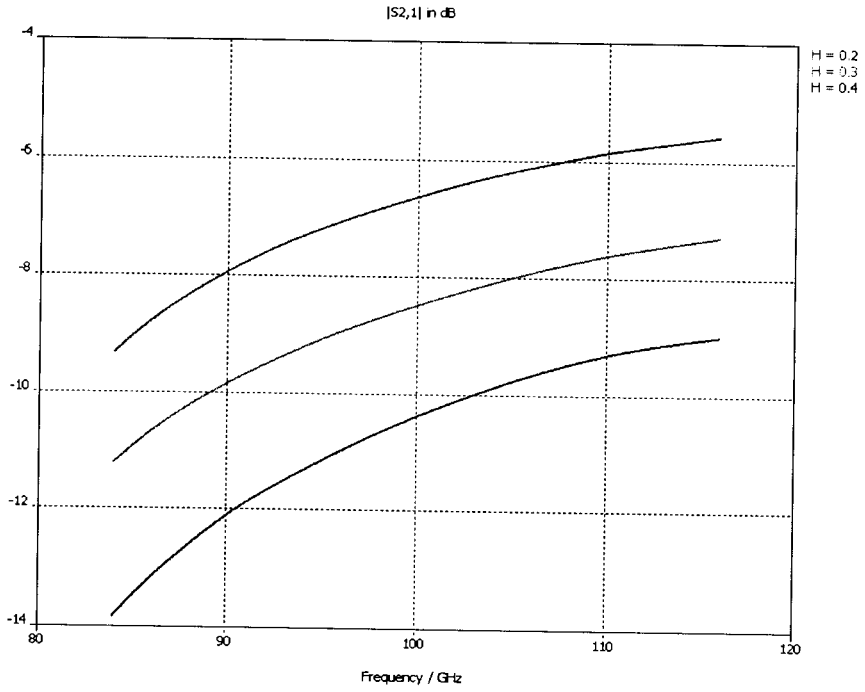
|S2,1| in dB
H = 0.2
H = 0.3
H = 0.4
-4
-6
-8
-10
-12
-14
80
90
100
110
120
Frequency / GHz

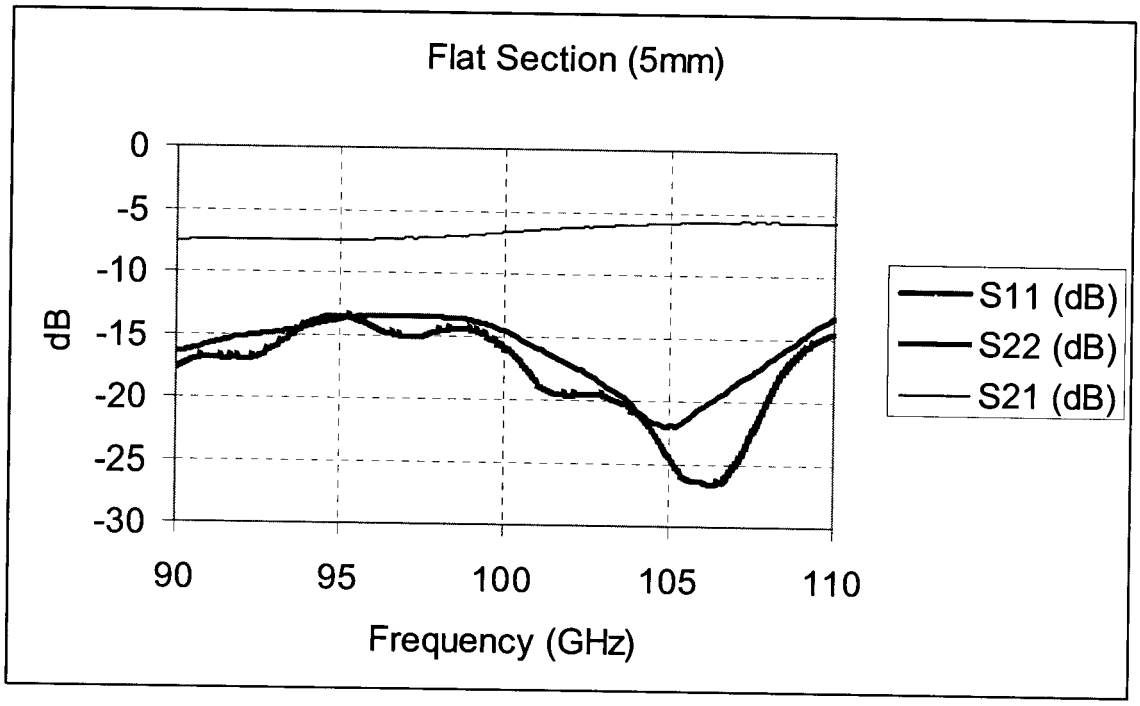
Flat Section (5mm)
0
-5
-10
-15
-20
-25
-30
dB
90
95
100
105
110
Frequency (GHz)
S11 (dB)
S22 (dB)
S21 (dB)

Appendix C MATLAB Functions Used with MEFiSTo

To create a SIS element within the MEFiSTo modeling environment, the *IV Element* device is selected. The command statement

```
@matlab currInit currTest currInstant + 1
```

is used to call MATLAB to execute the quantum theory algorithms which are provided below. The functions below assume that the response function, called *chi*, has already been calculated using (59) and is stored in a text file within the same directory.

```
%*************************************************
%******************** currInit.m ********************
% This script file initializes sets up the I-V parameters

close all;
clear all;

% Define global constants
global Rn;
global vg;
global q;
global hbar;
global timeStep;
global phaseFactor;   % will be a vector.  Intially starts as null
global chi;   % this is the response function (must be pre-calculated)
global index; % shift index for the iteration
global convNMinusOne; % variable used to store part of the convolution

% Define Constants and recall data
index = 0;
Rn = 25;    % define normal state resistance in ohms
vg = 2.808e-3; % gap voltage in Volts
h=6.6260755E-34;    % planck's constant
q=1.60217733E-19;   % electron voltage
k=1.380658E-23;     % Boltzmann's constant
```

```
hbar = h/(2*pi);

load -ascii Chi.txt; % assumes response function is stored in ascii
timeScaleChi = Chi(1,:); % first row is the time in seconds
timeStep = Chi(1,2);
chi = Chi(2,:); % the second row is the calculated response function
clear Chi;  % delete old variable because it's case sensitive

currInstant(0); % make a call to currInstant first


%*****************************************************
function curr = currTest(vTest)
% ******************** currTest.m ********************
% Takes an input test voltage (at t=k) and computes the current.
% Uses an input 'convNMinusOne' that contains the convolution that
% has already been calculated up to (n-1).  The convolution
% re-uses the (n-1) value for each new test voltage.

global Rn;
global timeStep;
global phaseFactor;
global index;
global chi;
global q;
global hbar;
global convNMinusOne;

% redo last part of phaseFactor
if index == 1
    phaseFactor(index) = exp( -i*q/hbar * vTest * timeStep);
else
    phaseFactor(index) = phaseFactor(index-1)
    * exp( -i*q/hbar * vTest * timeStep);
end

convFull = convNMinusOne + chi(1)*phaseFactor(index);
currConv = convFull * timeStep;
```

```
curr = vTest/Rn + imag( conj(phaseFactor(index)) * currConv);


function curr = currInstant(vInstant)
%*******************************************************
% ******************** currInstant.m *******************
% This function gives the instantaneous current at the given timestep.
% The previous convolution and phase factor results have been stored
% so only the new information is added.
% The variable 'convNMinusOne' is defined and can be used for testing
% out a voltage at the same time step using the function 'currTest.m'

global Rn;
global q;
global hbar;
global timeStep;
global phaseFactor;
global chi;
global index;
global convNMinusOne;

index = index + 1;

if index == 1
    phaseFactor(index) = exp( -i*q/hbar * vInstant * timeStep);
else
    phaseFactor(index) = phaseFactor(index-1)
    * exp( -i*q/hbar * vInstant * timeStep);
end

lengthChi = length(chi);

if lengthChi > index
    convNMinusOne = sum( fliplr(chi(2:index))
    .* phaseFactor(1:index-1));
else
    convNMinusOne = sum( fliplr(chi(2:lengthChi))
    .* phaseFactor(index-lengthChi+1:index-1));
```

```
end

convFull = convNMinusOne + chi(1)*phaseFactor(index);
currConv = convFull * timeStep;
curr = vInstant/Rn + imag( conj(phaseFactor(index)) * currConv);
%*********************************************************
%*********************************************************
```